

5

3395

3396

3397

Longevity studies and Consolidation of the present CMS RPC system

3398 The RPC system, located in both barrel and endcap regions, provides a fast, independent muon
3399 trigger over a large portion of the pseudo-rapidity range ($|\eta| < 1.6$). During HL-LHC operations
3400 the expected conditions in terms of background and pile-up will make the identification and correct
3401 p_T assignment a challenge for the muon system. The goal of the RPC upgrade is to provide additional
3402 hits to the Muon System with more precise timing. All this information will be elaborated by the
3403 Trigger System in a global way enhancing the performance of the muon trigger in terms of efficiency
3404 and rate control. The RPC Upgrade consists of two projects: an improved Link Board System and
3405 the extension of the RPC coverage up to $|\eta| = 2.4$.

3406 The Link Board System is responsible for the processing, the synchronization and the zero-
3407 suppression of the signals coming from the RPC FEBs. The Link Board components have been
3408 produced between 2006 and 2007 and will be subjected to ageing and failure on a long term scale.
3409 An upgraded Link Board System will overcome the ageing problems and will allow for a more
3410 precise timing information to the RPC hits from 25 to 1.5 ns.
3411 In order to develop an improved RPC that fulfills CMS requirements, an extensive R&D program is
3412 being conducted. The benefits of adding two new RPC layers in the innermost ring of stations 3 and
3413 4 will be mainly observed in the neutron-induced background reduction and efficiency improvement
3414 for both the muon trigger and the offline reconstruction.

3415 The coverage of the RPC System up to higher pseudo-rapidity $|\eta| = 2.1$ was part of the original
3416 CMS TDR. Nevertheless, the expected background rates being higher than the certified rate capa-
3417 bility of the present CMS RPCs in that region and the budget being limited, RPCs were restricted to
3418 a smaller pseudo-rapidity range. Even though the iRPC technology that will equip the extension of
3419 the Muon System will be different than the current CMS RPC technology, it is necessary to certify
3420 the rate capability and longevity of the existing detectors as the radiation level will increase together
3421 with the increase of instantaneous luminosity of the LHC. For this purpose, unused spare CMS RPC
3422 detectors have been installed in different irradiation facilities, first of all, to certify the detectors to

the new levels of irradiation they will be subjected to and, finally, to study their ageing and certify their good operation throughout the HL-LHC program.

This chapter will discuss the longevity and consolidation studies of the present CMS RPC system to which I have contributed. Two different irradiation facilities have been used at CERN. In each of them I took a leading role in defining the experimental set-up, but also in the data collection and data analysis. In the first facility in which preliminary tests were conducted, I also worked on simulations of the experimental setup and I made predictions on the particle rate expected at the detector level. During the last 4 years of longevity test conducted in the second facility, I became a DAQ expert and built a software which is now the base for the data collection to study the longevity of CMS RPCs. Moreover, I also worked together with the Detector Control Software (DCS) expert to provide an online monitoring of the collected data. Indeed, I developed a software that automates the extractions of the detectors' data and produces plots at destination of the users thanks to a fast analysis. This software is a corner stone for the final data analysis. Documentations of both these softwares are given in Appendix A and Appendix B.

In a first section of the chapter, the irradiation facilities will be described. The study conducted will then be summarized in details. A description of the set-ups as well as a comprehensive review of the obtained results will be provided.

5.1 Testing detectors under extreme conditions

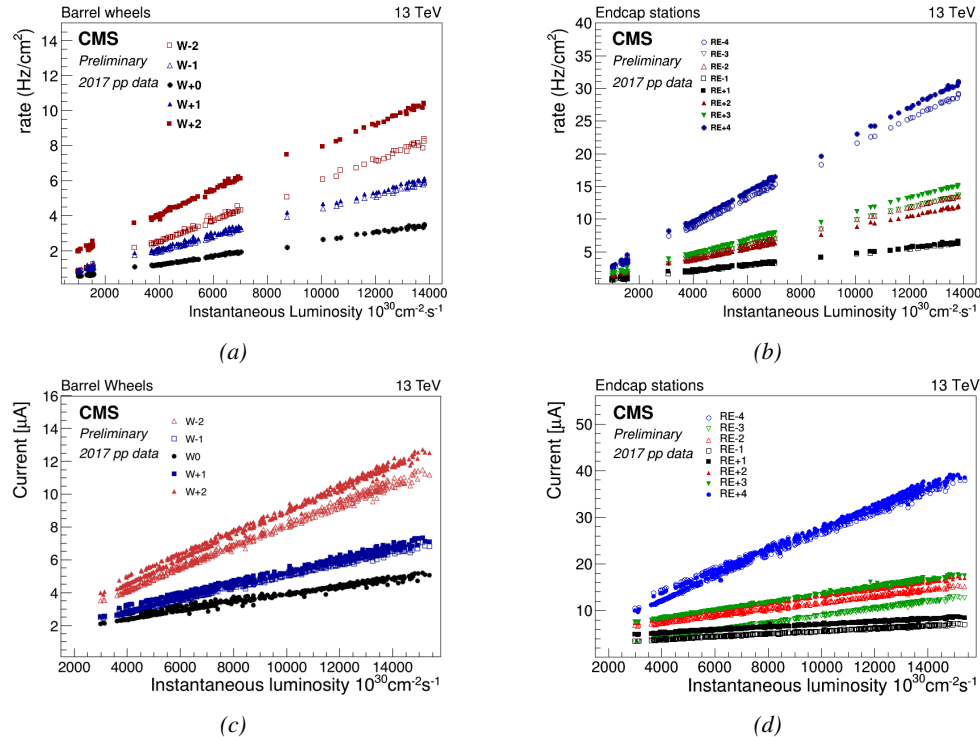


Figure 5.1: Mean RPC Barrel (left column) and Endcap (right column) rate (top row) and current (bottom row) as a function of the instantaneous luminosity as measured in 2017 p-p collision data.

The upgrade from LHC to HL-LHC will increase the peak luminosity from $10^{34} \text{ cm}^{-2} \text{ s}^{-1}$ to $5 \times 10^{34} \text{ cm}^{-2} \text{ s}^{-1}$, increasing the total expected background to which the RPC system will be subjected. Mainly composed of low energy gammas, neutrons, and electrons and positrons from $p\text{-}p$ collisions, but also of low momentum primary and secondary muons, punch-through hadrons from calorimeters, and particles produced in the interaction of the beams with collimators, the background will mostly affect the regions of CMS that are the closest to the beam line, i.e. the RPC detectors located in the endcaps.

Data collected during 2017, presented in Figure 5.1, allows to study the values of the background rate in the entire RPC system. This was achieved thanks via the monitoring of the rates in each RPC rolls and of the current in each HV channel. A linear dependence of the mean rate or current on the instantaneous luminosity is shown in selected runs with identical LHC running parameters. It is assumed that such a linear behaviour should be observed at even higher luminosities and is therefore used to extrapolate the rates and currents that will be expected during HL-LHC. In Figure 5.2, a linear extrapolation of the distribution of the background hit rate per unit area as well as the integrated charge is shown at a HL-LHC condition. The maximum hit rate per unit area in the endcap detectors at HL-LHC conditions is expected to be of the order of 600 Hz/cm^2 while the charge deposition should exceed 800 mC/cm^2 . The detectors will thus have to be certified up to an irradiation of 840 mC/cm^2 . These extrapolations are provided with a required safety factor 3 for the certification study.

In the past, extensive long-term tests were carried out at several gamma and neutron facilities certifying the detector performance. Both full size and small prototype RPCs have been irradiated with photons up to an integrated charge of $\sim 0.05 \text{ C/cm}^2$ and $\sim 0.4 \text{ C/cm}^2$ respectively and were certified for rates reaching 200 Hz/cm^2 [262, 263]. Since the beginning of Run-I until December 2017, the RPC system provided stable operation and excellent performance. The average integrated charge is of about 1.66 mC/cm^2 in the Barrel and 4.58 mC/cm^2 in the Endcap, closer to the beam line, as can be seen in Figure 5.3). The detectors did not show any ageing effects for a maximum integrated charge in a detector of the order of 0.01 C/cm^2 and a peak luminosity reaching $1.4 \times 10^{34} \text{ cm}^{-2} \text{ s}^{-1}$ during the 2017 data taking period.

To perform the necessary studies on the present CMS RPC detectors, facilities offering the possibility to irradiate the chambers are necessary in order to recreate HL-LHC conditions or stronger and

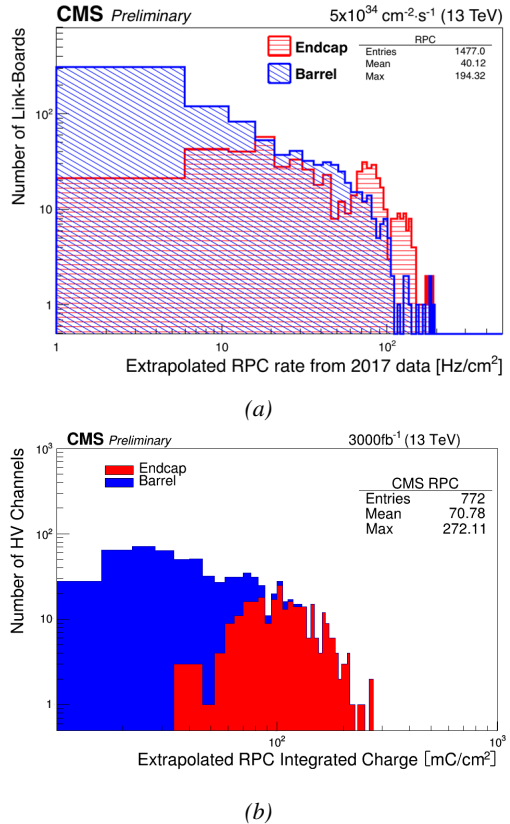


Figure 5.2: Linear extrapolation of the hit rate (a) and of the integrated charge (b) per region (Barrel, Endcap) respectively to HL-LHC instantaneous luminosity ($5 \times 10^{34} \text{ cm}^{-2} \text{ s}^{-1}$) and HL-LHC integrated luminosity (3000 fb^{-1}).

study the detector performance through time. A first series of such studies was conducted in the former Gamma Irradiation Facility (GIF) of CERN before its dismantlement starting from September 2014. This preliminary study was used as a stepping stone towards the building of a more powerful irradiation fully dedicated to longevity studies of CMS and ATLAS subsystems in the perspective of HL-LHC. The period of preliminary work has also been a key moment in the elaboration and improvement of data acquisition, offline analysis and online monitoring tools that are extensively used in the new gamma irradiation facility.

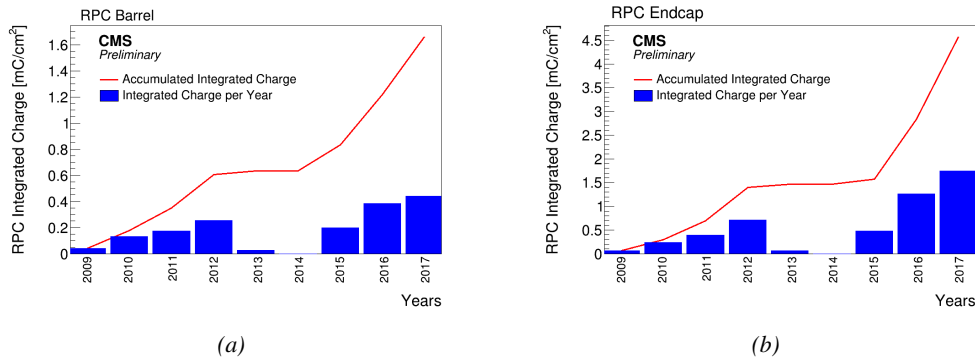


Figure 5.3: CMS RPC mean integrated charge in the Barrel region (a) and the Endcap region (b). The integrated charge per year is shown in blue. The red curve shows the evolution of the accumulated integrated charge through time. The blank period in 2013 and 2014 corresponds to LS1.

5.1.1 The Gamma Irradiation Facility

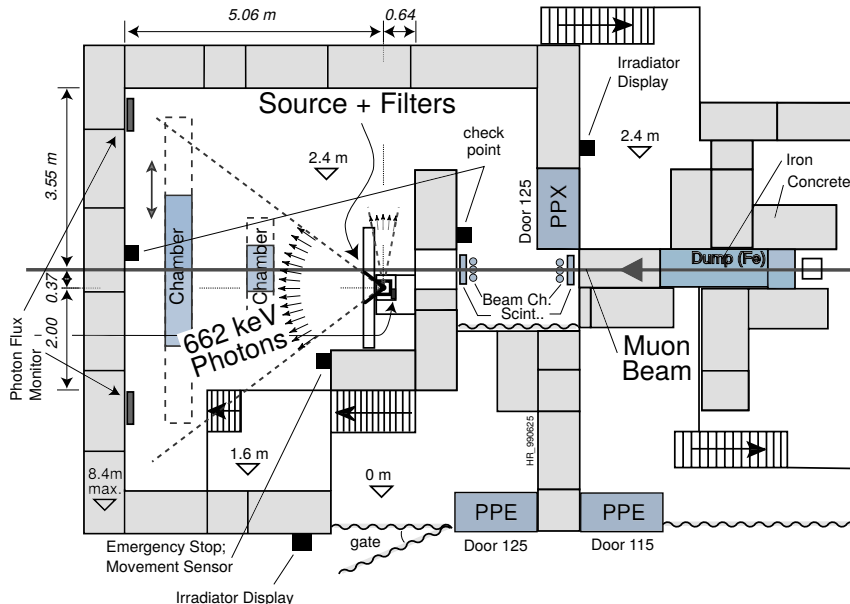


Figure 5.4: Layout of the test beam zone of GIF at CERN.

3495 Located in the SPS West Area at
 3496 the downstream end of the X5 test beam, the GIF was a test area in
 3497 which particle detectors were ex-
 3498 posed to a particle beam in pres-
 3499 ence of an adjustable gamma back-
 3500 ground [264]. Its goal was to repro-
 3501 duce background conditions these
 3502 detectors would endure in their op-
 3503 erating environment at LHC. The
 3504 layout of the GIF is shown in Figure
 3505 5.4. Gamma photons are produced
 3506 by a strong ^{137}Cs source installed in
 3507 the upstream part of the zone inside
 3508

3509 a lead container. The source container includes a collimator, designed to irradiate a $6 \times 6 \text{ m}^2$ area at
 3510 5 m maximum distance to the source. A thin lens-shaped lead filter helps providing with a uniform
 3511 out-coming flux in a vertical plane, orthogonal to the beam direction. The photon rate is controlled
 3512 by further lead filters allowing the maximum rate to be limited and to vary within a range of four
 3513 orders of magnitude. Particle detectors under test are then placed within the pyramidal volume in
 3514 front of the source, perpendicularly to the beam line in order to profit from the homogeneous photon
 3515 flux. Adjusting the background flux of photons can then be done using the filters and choosing the
 3516 position of the detectors with respect to the source. The zone is surrounded by 8 m high and 80 cm
 3517 thick concrete walls. Access is possible through three entry points. Two access doors for personnel
 3518 and one large gate for material. A crane allows installation of heavy equipment in the area.

3519 As described on Figure 5.5, the ^{137}Cs source emits a 662 keV photon in 85% of the decays. An
 3520 activity of 740 GBq was measured on the 5th of March 1997. The half-life of Cesium is well known
 3521 ($t_{1/2} = (30.05 \pm 0.08) \text{ y}$) and can be used to compute the activity of the source at the time of the
 3522 study. The GIF tests were done in between the 20th and the 31st of August 2014, i.e. at a time $t =$
 3523 ($17.47 \pm 0.02) \text{ y}$ resulting in an attenuation of the activity from 740 GBq in 1997 to 494 GBq in
 3524 2014.

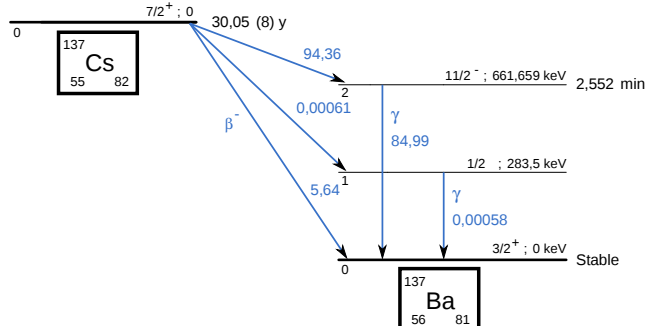


Figure 5.5: ^{137}Cs decays by β^- emission to the ground state of ^{137}Ba ($BR = 5.64\%$) and via the 662 keV isomeric level of ^{137}Ba ($BR = 94.36\%$) whose half-life is 2.55 min.

3525 5.1.2 The new Gamma Irradiation Facility

3526 The GIF++, located in the SPS North Area at the downstream end of the H4 test beam, has replaced
 3527 its predecessor during LS1 and has been operational since spring 2015 [265]. Like GIF, GIF++
 3528 features a ^{137}Cs source of 662 keV gamma photons, their fluence being controlled with a set of
 3529 filters of various attenuation factors. The source provides two separate large irradiation areas for
 3530 testing several full-size muon detectors with homogeneous irradiation, as presented in Figure 5.6.

3531 The source activity was measured to be about 13.5 TBq in March 2016. With the photon flux
 3532 being far greater than HL-LHC expectations, GIF++ provides an excellent facility for accelerated
 3533 ageing tests of muon detectors. The source is situated in a bunker designed to perform irradia-
 3534 tion test along a muon beam line, which is available during selected periods throughout the year.
 3535 The H4 beam, providing the area with muons with a maximum momentum of about 150 GeV/c,
 3536 passes through the GIF++ zone and is used to periodically study the performance of the detectors
 3537 placed under long term irradiation. Its flux is of 104 particles/s/cm² focused in an area of about
 3538 $10 \times 10 \text{ cm}^2$.

	1	2	3
A	1	10	100
B	1	1.468	100
C	1	2.154	4.642

Table 5.1: Attenuation of single filters on each filter plane of the GIF++ Cesium source.

attenuation factor (for example $333 = 100 \times 100 \times 4.642 = 46420$).

Adjusting the gamma flux is possible thanks to the three planes (A, B and C) of adjustable absorbers featured on the Cesium source [266]. With properly adjusted filters, one can simulate the background expected at HL-LHC and study the performance and ageing of muon detectors in HL-LHC environment. Each plane of filters features three filters (1, 2 and 3) with different Absorption factor (ABS) listed in Table 5.1. The source absorber settings can be referred by a three digit number with a format ABC or by its

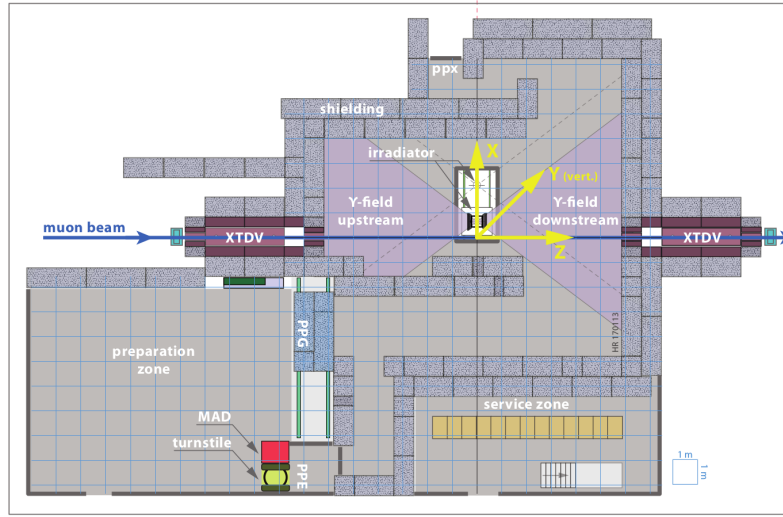


Figure 5.6: Floor plan of the GIF++ facility. When the facility downstream of the GIF++ takes electron beam, a beam pipe is installed along the beam line (z -axis). The irradiator can be displaced laterally (its center moves from $x = 0.65$ m to 2.15 m), to increase the distance to the beam pipe.

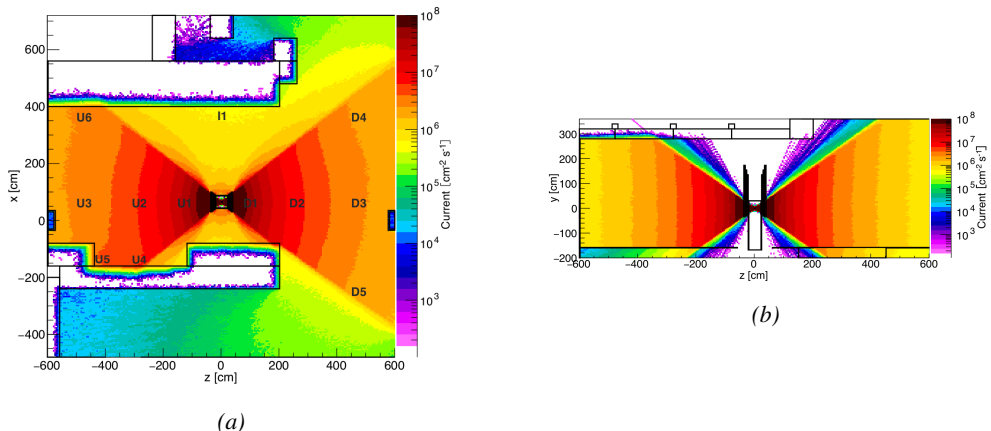


Figure 5.7: Simulated unattenuated current of photons in the xz plane (a) and yz plane (b) through the source at $x = 0.65$ m and $y = 0$ m [267]. With angular correction filters, the current of 662 keV photons is made uniform in xy planes.

The gamma current as simulated with GEANT4 is presented in Figure 5.7. In their simulation paper [267], Pfeiffer et al. define the particle current as "a measure of the net number of particles crossing a flat surface with a well-defined orientation. The unit of current is $\text{m}^{-2} \text{s}^{-1}$ and thus identical to the unit of flux. Current is meaningful in cases where particles are counted without any interest in their interactions." The labels UN, DN, with $N \in [1 : 5]$ and I1 correspond to the position of different Radiation Monitoring (RADMON) sensors measuring the irradiation in the bunker area [267]. According to the simulation results, that agree within 12% to the doses measured with the RADMONs, the RPCs that will be tested in GIF++ can expect a maximal gamma current of the order of 2 to $5 \times 10^6 \text{ cm}^{-2} \text{s}^{-1}$ assuming they will always stay in a region in between sensor U5 and the back wall of the upstream area.

5.2 Preliminary studies at GIF

5.2.1 RPC test setup

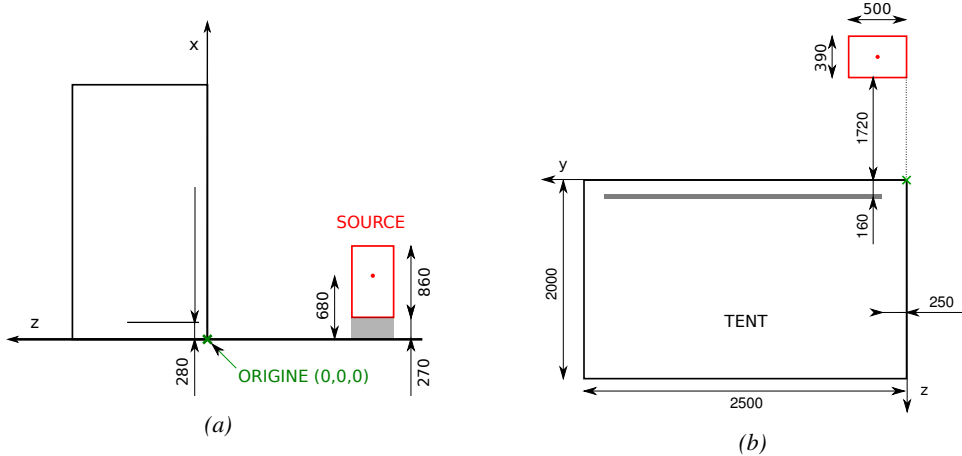


Figure 5.8: Description of the RPC setup. Dimensions are given in mm. A tent containing RPCs is placed at 1720 mm from the source container. The source is situated in the center of the container. RE-4-2-BARC-161 chamber is 160 mm inside the tent. This way, the distance between the source and the chambers plan is 2060 mm. Figure (a) provides a side view of the setup in the xz plane while Figure (b) shows a top view in the yz plane.

During Summer 2014, preliminary tests have been conducted in the GIF area on an endcap chamber of type RE4/2 and labeled RE-4-2-BARC-161 produced for the extension of the endcap with a fourth disk in 2013. This chamber has been placed into a trolley covered with a tent in order to control the temperature. The positions of the RPC inside the tent and of the tent with respect to the source in the bunker are described in Figure 5.8. The goal of the study was to have a preliminary understanding of the rate capability of the present technology used in CMS. It was decided to measure the efficiency of the RPC under irradiation for detecting cosmic muons as, at the time of the tests, the beam was not operational anymore. Three different absorber settings were used and compared to the case where the detector was not irradiated in order to study the evolution of the performance of the detector with increasing exposure to gamma radiation. First of all, measurements were done with the fully opened source. To complete this preliminary study, the gamma flux has been attenuated by

3571 a factor 2, a factor 5 and finally the source was shut down. The efficiency of the RPC at detecting
 3572 the cosmic muons in coincidence with a cosmic trigger as well as the background rate as seen by the
 3573 detectors were measured.

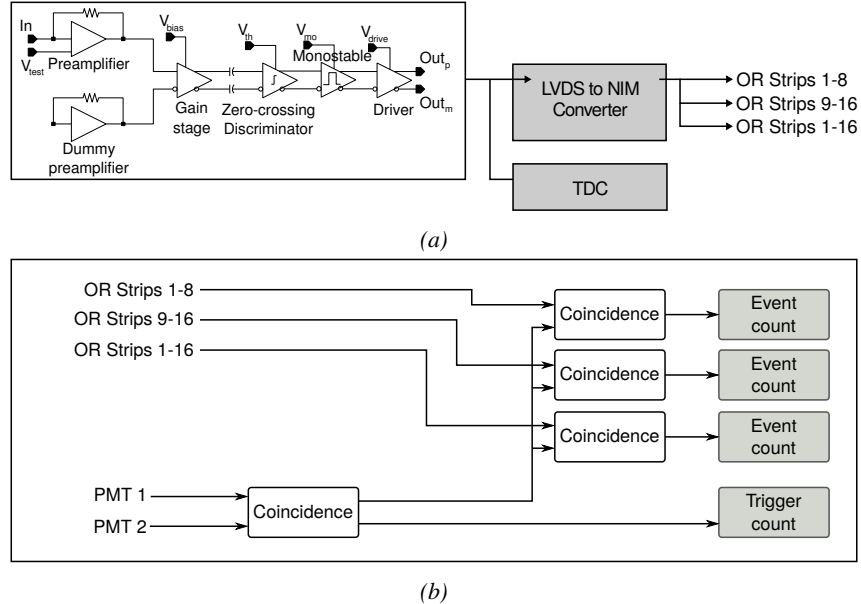


Figure 5.9: (a) Shaping of the signals from the RPC strips by the FEE. The output LVDS signals are then read-out by a TDC module connected to a computer or converted into NIM and sent to scalers. (b) Trigger logic implementation with the RPC and photomulitplier signals.

3574
 3575
 3576
 3577
 3578
 3579
 3580
 3581
 3582
 3583
 3584
 3585
 3586



3587 Figure 5.10: RE-4-2-BARC-161 chamber is inside the tent as
 3588 described in Figure 5.8. In the top right, the two scintillators used
 3589 as trigger can be seen.

3590
 3591
 3592
 3593

libraries and the data collected by the TDCs was saved into .dat files is analysed with an algorithm computing parameters such as efficiency, hit profile, cluster size, or gamma and noise rates which was developed with C++ as well. Finally, histograms and curves are produced using ROOT.

The data taking was performed using a CEAN TDC module of type V1190A [268] to which the digitized output of the RPC Front-End Board is connected, as described in Figure 5.9a and the trigger signal from the telescope. The communication with the computer is performed thanks to a CAEN communication module of type V1718 [269]. In order to control the rates recorded by the detector, the digitized RPC signals are also sent to scalers as described in Figure 5.9b. The C++ DAQ software used in GIF was developed as an early attempt towards the understanding of the CAEN li-

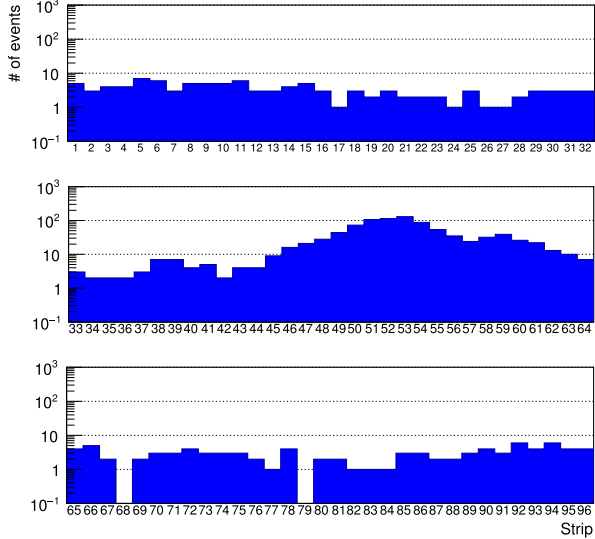
3594 The trigger system was composed of two plastic scintillators and
 3595 was placed in front of the setup with an inclination of 10° with respect to
 3596 the detector plane in order to look at cosmic muons. Using this particular
 3597 trigger layout, shown in Figure 5.10,
 3598 lead to a cosmic muon hit distribution into the chamber similar to the
 3599 one of Figure 5.11. As mentioned in Chapter 2, the endcap RPC readout
 3600 is segmented into three pseudo-rapidity partitions. The outer most
 3601 partition, corresponding to the wide end of the chamber, is the partition
 3602 A. The other two partitions are the
 3603 partitions B and C. Each of them
 3604 consists in 32 copper strips. These
 3605 32 strips are connected to the FEEs
 3606 by groups of 16. The trigger is
 3607 placed in front of the half-partition
 3608 B2 which corresponds to the last 16 strips of partition B (49 to 64).
 3609

3610 Measured without gamma irradiation, two peaks can be seen on the profile of readout partition
 3611 B, centered on strips 52 and 59. Some events still occur in other half-partitions than B2 contributing
 3612 to the inefficiency of detection of cosmic muons. In the case of partitions A and C, the very low
 3613 amount of data can be interpreted as noise. On the other hand, it is clear that a little portion of
 3614 muons reached the half-partition B1 (strips 33 to 48). Section 5.2.2 will help us understand that
 3615 these two peaks are due respectively to forward and backward coming cosmic particles. Forward
 3616 coming particles are detected first by the scintillators and then the RPC while the backward going
 3617 muons are first detected in the RPC.

3624 5.2.2 Geometrical acceptance of the setup layout to cosmic muons

3625 In order to profit from a constant gamma irradiation, the detectors inside of the GIF bunker had to be
 3626 placed in a plane orthogonal to the beam line. The muon beam that used to be available was meant to
 3627 test the performance of detectors under test. This beam being not active anymore, another solution
 3628 to test detector performance had to be used. Thus, it was decided to use cosmic muons detected
 3629 through a telescope composed of two scintillators. Lead blocks were used as shielding to protect the
 3630 photomultipliers from gammas as can be seen from Figure 5.10.

3631 An inclination of $\sim 10^\circ$ was given to the cosmic telescope to increase the muon trigger rate for
 3632 this otherwise horizontal setup. A good compromise had to be found between good enough muon
 3633 flux and narrow enough hit distribution to be sure to contain all the events into a single half-partition
 3634 as required from the limited available readout hardware. It was then foreseen to detect muons and
 3635 read them out only from half-partition B2. Nevertheless, a misplacement of the trigger scintillators
 3636 resulted in an inefficiency, as can be seen in Figure 5.11 with events appearing in half-partition B1.



3637 *Figure 5.11: Hit distributions over all three partitions of
 3638 RE-4-2-BARC-161 chamber is showed. Top, middle and bottom
 3639 figures respectively correspond to partitions A, B, and C.*

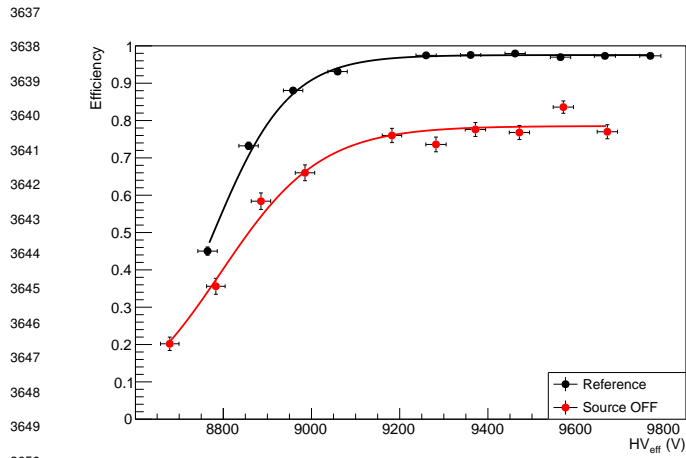


Figure 5.12: Comparison of the efficiency of chamber RE-4-2-BARC-161 with and without irradiation. Results are derived from data taken on half-partition B2 only.

by the red curve. The inefficiency too high compared to the 12.7% of data contained into the first 16 strips observed on Figure 5.11, to be explained only by the geometrical acceptance of the setup itself. Simulations have been conducted to quantify the inefficiency of the setup.

5.2.2.1 Geometrical acceptance simulation setup

The layout of the GIF setup has been reproduced¹ and incorporated into a C++ Monte Carlo (MC) simulation to study the geometrical acceptance of the telescope projected onto the readout strips [270]. A 3D view of the simulated layout is given into Figure 5.13. The RPC read-out plane is represented as a yellow trapezoid while the two scintillators as blue cuboids. The green plane corresponds to the $4 \times 4.5 \text{ m}^2$ muon generation plane centered on the experimental setup within the simulation. The goal of the simulation is to look at muons that pass through the telescope composed of the two scintillators and define their distribution onto the RPC read-out plane. During the reconstruction, the read-out plane is then divided into its read-out strips and each muon track is assigned to a strip.

$N_\mu = 10^8$ muons are generated at a random position in the horizontal generation plane. This position corresponds to the intersection of the muon track with the generaltion plane. The plane is located at a height corresponding to the lowest point of the scintillators in order to easily simulate muons coming at very large zenith angles (i.e. $\theta \approx \pi$). The position of the particle within the plane is associated with a random direction: an azimuth angle ϕ chosen between 0 and 2π and a zenith angle θ chosen between 0 and $\pi/2$ to follow a usual $\cos^2\theta$ distribution for cosmic particles. Then, using the position of the muon in the generation plane and its direction, the intersection of the track with the planes of the scintillator cuboids is computed. In the case the muon wasn't found within the surface of both the scintillators, the simulation restarts and generates a new muon. On the contrary, if the track passed through the telescope, the simulation goes on. The position of the muon hit within the RPC read-out plane is computed. The hits are saved into histograms, one per read-out partition,

As can be seen in Figure 5.12, a comparison of the performance of chamber RE-4-2-BARC-161 with and without irradiation suggests an inefficiency of approximately 20%. On the 18th of June 2014, data have been taken on the chamber at CERN building 904 (Prevessin Site) with cosmic muons providing us a reference efficiency plateau of $(97.54 \pm 0.15)\%$ represented by the black curve. A similar measurement has been done at GIF on the 21st of July with the same chamber giving a plateau of $(78.52 \pm 0.94)\%$ represented

¹Albeit only roughly using Figure 5.10 due to the lack of actual measurements of the respective positions of each parts of the experimental setup. Using reference dimensions such as the saize of the detector and the size of the photomultiplier, the positions could be deduced.

whose bins corresponds to the RPC copper strips. The strip in which the hit occured is determined by knowing precisely the geometry of the RPC. Muon hits are also filled in different histograms whether they are associated to forward coming ($\pi \leq \phi < 2\pi$) or backward going ($0 \leq \phi < \pi$) muons.

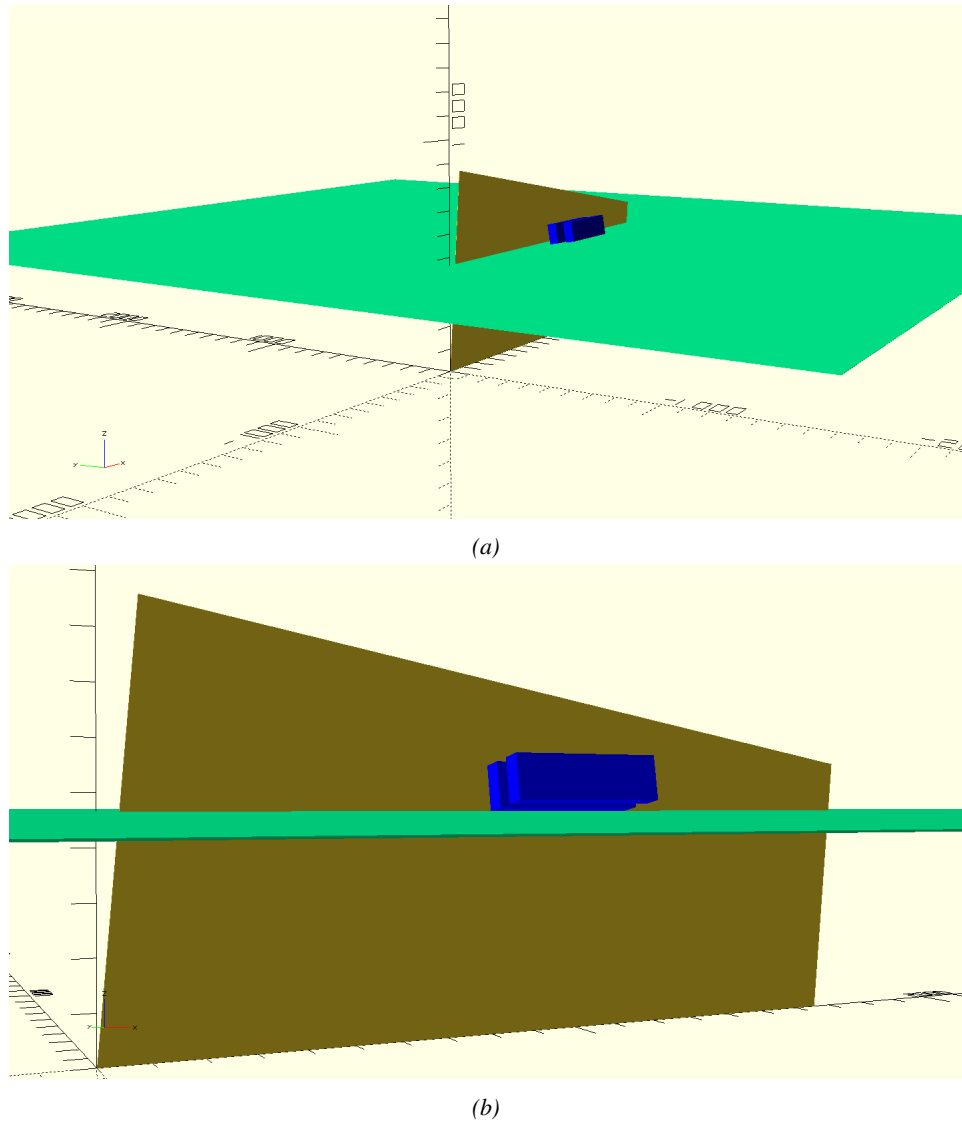


Figure 5.13: Representation of the layout used for the simulations of the test setup. (a) Global view of the simulated setup. (b) Zoomed view on the experimental setup.

5.2.2.2 Results and limitations

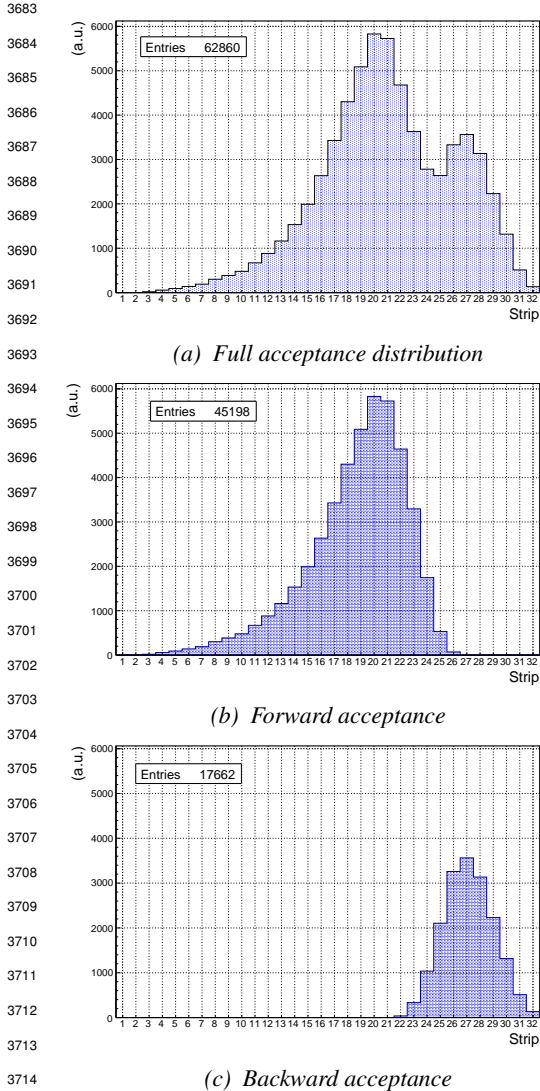


Figure 5.14: Geometrical acceptance distribution as provided by the Monte Carlo simulation.

affected by a variation of the inclination angle, as can be seen in Figure 5.16. Yet, the position of the acceptance peaks in the distribution would be in agreement with what is measured, and the contribution of farward and backward muons would never reach the observation. With an inclination of 10° , 28.1% of the total geometrical acceptance should contribute to detecting backward muons whereas it is measured that the hit profile contains 22.0% of backward data only. Introducing in the simulation an error of $\pm 2^\circ$ would lead to a correction factor $c_{geo} = 1.20^{+0.04}_{-0.03}$ allowing for a good improvement of the efficiency measured in GIF, as can be seen from Figure 5.17. GIF measurement is in agreement with the reference curve within statistical errors.

The output from the simulation is given in Figure 5.14 in which the geometrical acceptance distribution of the setup is shown. The distributions for the separate contributions of forward coming and backward going muons are all provided. The strip number is given in a range of 1 to 32 corresponding to the 32 strips contained in each RPC read-out partition even though partition B correponds, by convention, to strip numbers 33 to 64. It can be established than, out of the total amount of muons that have passed through the telescope and reached the RPC, 16.8% were hitting the 16 first strip of the read-out plane corresponding to half partition B1. This number corresponds to the inefficiency. It can be used then to correct the data by scaling up by a factor $c_{geo} = 1/(1 - 0.168)$ the efficiency measured during data taking.

Nevertheless, the distribution showed in Figure 5.14a differs from the measured hit profile showed in Figure 5.11 as can be seen in Figure 5.15. It is difficult to evaluate a systematic uncertainty on this geometrical correction for different reasons.

First of all, even though the dimensions of the scintillators and of the RPC are well known, the position of each element of the setup with respect to one another was not measured. The extraction of the position of each part of the setup from Figure 5.10 was a first large source of error.

The inclination is also roughly measured to be 10° bringing more uncertainty into the simulation. The acceptance distribution would be

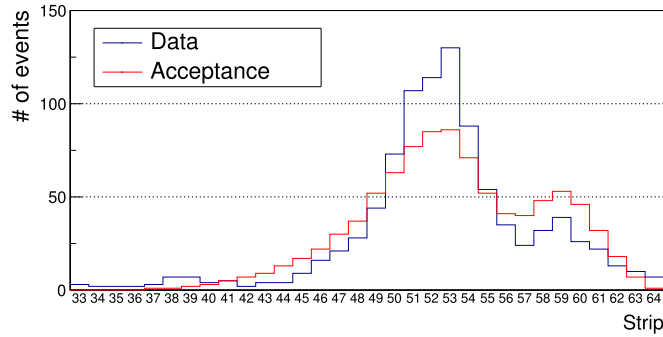


Figure 5.15: Comparison of the hit distribution recorded in the detector and of the normalised geometrical acceptance distribution.

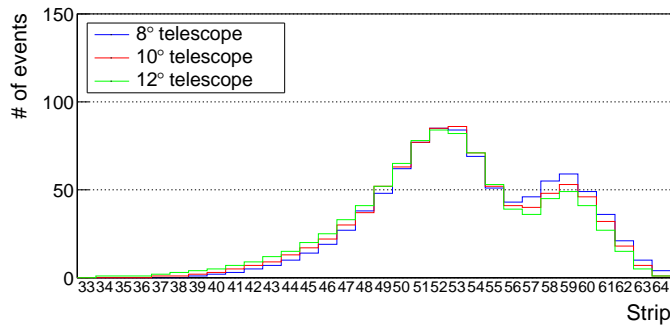


Figure 5.16: Effect of the variation of telescope inclination on the normalised geometrical acceptance distribution.

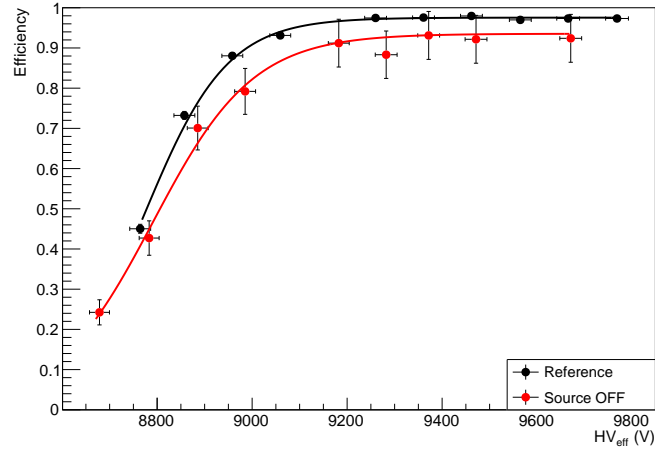


Figure 5.17: Correction of the efficiency without source. The efficiency after correction gets much closer to the Reference measurement performed before the study in GIF by reaching a plateau of $(93.52 \pm 2.64)\%$.

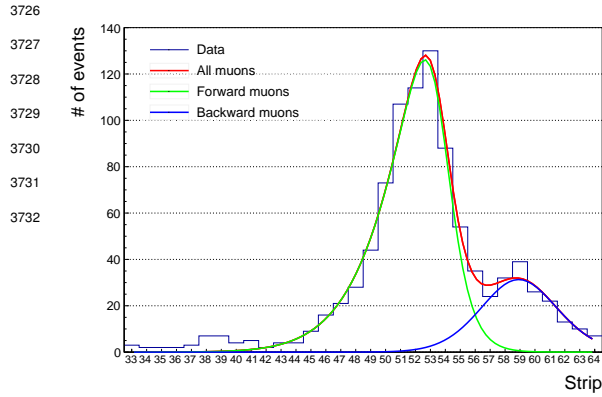


Figure 5.18: Hit distributions over read-out partition B of RE-4-2-BARC-161 chamber together with skew distribution fits corresponding to forward and backward coming muons.

Given the observed difference between the simulation and the measured data, one should realize that the geometrical acceptance and the hit profile are actually not directly comparable. The geometrical acceptance only provides with the information about what the detector can expect to see in a perfect world where all muons are detected in the exact same way. The detection would be independent from their energy or angle of incidence, and there would be no fluctuation of the detector gain due to complex avalanche development. No thresholds would be applied on the scintillators and on the RPC FEEs to reduce the noise, the cross-talk and the corresponding spread of the induced charge observed on the read-out strips. The hit profile provides the final product of all the previously mentioned contributions and can greatly differ from purely geometrical considerations. A full physics analysis involving softwares such as GEANT would be required to further refine the correction on the measured efficiency at GIF.

5.2.3 Photon flux at GIF

In order to understand and evaluate the γ flux in the GIF area, simulations have been conducted at the time GIF was opened for research purposes [264]. Table 5.2 gives the γ flux for different distances D to the source. The simulation was done using GEANT and a Monte Carlo N-Particle (MCNP) transport code, and the flux F is given with the estimated error from these packages expressed in %.

Nominal ABS	Photon flux F [$\text{cm}^{-2} \text{s}^{-1}$]			
	at $D = 50 \text{ cm}$	at $D = 155 \text{ cm}$	at $D = 300 \text{ cm}$	at $D = 400 \text{ cm}$
1	$0.12 \times 10^8 \pm 0.2\%$	$0.14 \times 10^7 \pm 0.5\%$	$0.45 \times 10^6 \pm 0.5\%$	$0.28 \times 10^6 \pm 0.5\%$
2	$0.68 \times 10^7 \pm 0.3\%$	$0.80 \times 10^6 \pm 0.8\%$	$0.25 \times 10^6 \pm 0.8\%$	$0.16 \times 10^6 \pm 0.6\%$
5	$0.31 \times 10^7 \pm 0.4\%$	$0.36 \times 10^6 \pm 1.2\%$	$0.11 \times 10^6 \pm 1.2\%$	$0.70 \times 10^5 \pm 0.9\%$

Table 5.2: Total photon flux ($E_\gamma \leq 662 \text{ keV}$) with statistical error predicted considering a ^{137}Cs activity of 740 GBq at different values of the distance D to the source along the x-axis of irradiation field [264].

This estimation of the backward versus forward content in the data was done through a fit using a sum of two skew distributions given in Equation 5.1. Although a skew distribution lacks physical interpretation, it allows fitting easily such kind of data, as showed in Figure 5.18.

$$(5.1) \quad \begin{aligned} g(x) &= A_g e^{-\frac{(x-\bar{x})^2}{2\sigma^2}} \\ s(x) &= \frac{A_s}{1 + e^{-\lambda(x-x_i)}} \\ sk(x) &= g(x) \times s(x) \\ &= A_{sk} \frac{e^{-\frac{(x-\bar{x})^2}{2\sigma^2}}}{1 + e^{-\lambda(x-x_i)}} \end{aligned}$$

3749 The table however does not
 3750 provide in a direct way the flux
 3751 at the level of the RPC under
 3752 test. First of all, it is nec-
 3753 essary to extract the value of
 3754 the flux from the available data
 3755 contained in the original paper
 3756 and then to estimate the flux in
 3757 2014 at the time the experimen-
 3758 tation took place. The extraction will be performed for the case of a pointlike source emitting
 3759 isotropic and homogeneous gamma radiations. The flux F_0 is known at a given reference point sit-
 3760 uated at D_0 from the source. The gamma flux F at a distance D from the source will be expressed
 3761 with Equation 5.2, assuming that the flux decreases as $1/D^2$ and where c is a fitting factor that can
 3762 be written as in Equation 5.3. Finally, using Equation 5.3 and the data of Table 5.2, with $D_0 =$
 3763 50 cm as reference point, Table 5.3 can be built. It is interesting to note that c for each value of D
 3764 does not depend on the absorption factor.

$$(5.2) \quad F^{ABS} = F_0^{ABS} \times \left(\frac{cD_0}{D} \right)^2$$

$$(5.3) \quad c = \frac{D}{D_0} \sqrt{\frac{F^{ABS}}{F_0^{ABS}}} \\ \Delta c = \frac{c}{2} \left(\frac{\Delta F^{ABS}}{F^{ABS}} + \frac{\Delta F_0^{ABS}}{F_0^{ABS}} \right)$$

3765 For the range of D/D_0 values available, it is possible to use a simple linear fit to get the evolution
 3766 of c that can be expressed as $c(D/D_0) = aD/D_0 + b$. Using Formula 5.4, but neglecting the
 3767 uncertainty on D that will only be used when extrapolating the values for the position of the RPC
 3768 under test whose position is not perfectly known, the results shown in Figure 5.19 is obtained.
 3769 Figure 5.19b confirms that using only a linear fit to extract c is enough as the evolution of the rate
 3770 that can be obtained superimposes well on the simulation points.

$$(5.4) \quad F^{ABS} = F_0^{ABS} \left(a + \frac{bD_0}{D} \right)^2, \quad \Delta F^{ABS} = F^{ABS} \left[\frac{\Delta F_0^{ABS}}{F_0^{ABS}} + 2 \frac{\Delta a + \Delta b \frac{D_0}{D} + \Delta D \frac{bD_0}{D^2}}{a + \frac{bD_0}{D}} \right]$$

3771 During the 2014 Gif tests, the RPC read-out plane was located at a distance $D = 206$ cm from
 3772 the source. Moreover, to estimate the strength of the flux in 2014, it is necessary to consider the
 3773 nuclear decay through time of the Cesium source whose half-life is well known ($t_{1/2} = (30.05 \pm$
 3774 0.08) y). The very first source activity measurement has been done on the 5th of March 1997 while
 3775 the Gif tests were done in between the 20th and the 31th of August 2014, i.e. at a time $t =$
 3776 (17.47 ± 0.02) y resulting in an attenuation of the activity from 740 GBq in 1997 to 494 GBq in
 3777 2014. All the needed information to extrapolate the expected flux through the detector at the moment
 3778 of the Gif preliminary tests has now been assembled, leading to Table 5.4. By assuming an average
 3779 sensitivity of the RPC to γ emitted by the ^{137}Cs source of $(2 \pm 0.2) \times 10^{-3}$ [271], the order of
 3780 magnitude of the expected hit rate per unit area would be of the order of kHz for a fully opened
 3781 source, as reported in the last column of the table. As photons are not charged particles, they mainly
 3782

3784 interact with the electrodes where they are converted into electrons. The HPL electrodes are not very
 3785 sensitive to gamma photons, hence only a small fraction of the incoming flux is seen by the RPC.

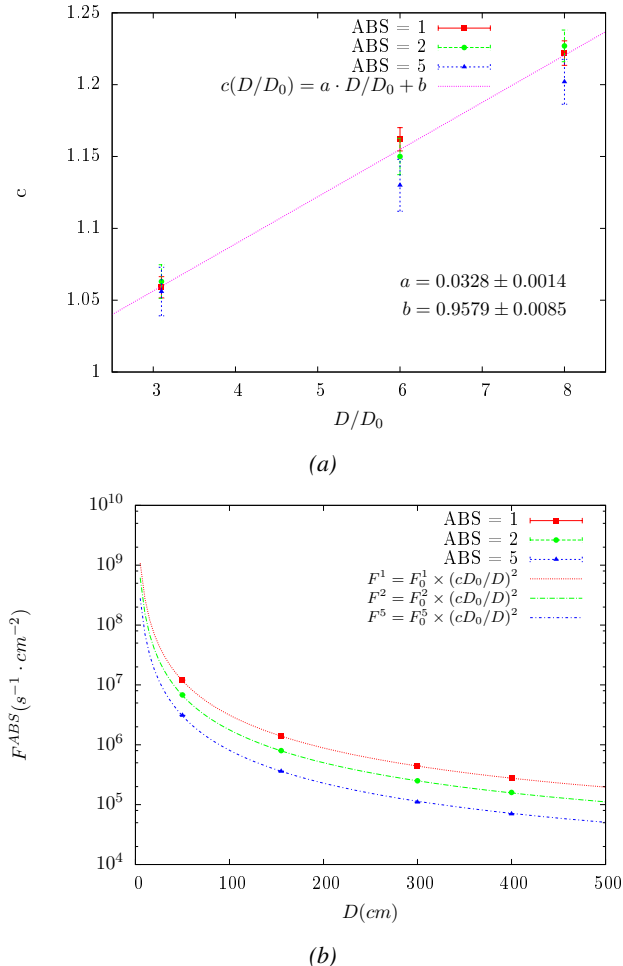


Figure 5.19: (a) Linear approximation fit performed on the data extracted from table 5.3. (b) Comparison of Equation 5.4 with the simulated flux using a and b given in figure 5.19a in Equation 5.2 and the reference $D_0 = 50$ cm and the associated flux for each absorption factor F_0^{ABS} from table 5.2.

Nominal ABS	Photon flux F [$cm^{-2} s^{-1}$]			Rate [Hz/cm ²] at $D^{2014} = 206$ cm
	at $D_0^{97} = 50$ cm	at $D^{97} = 206$ cm	at $D^{2014} = 206$ cm	
1	$0.12 \times 10^8 \pm 0.2\%$	$0.84 \times 10^6 \pm 1.2\%$	$0.56 \times 10^6 \pm 1.2\%$	1129 ± 14
2	$0.68 \times 10^7 \pm 0.3\%$	$0.48 \times 10^6 \pm 1.2\%$	$0.32 \times 10^6 \pm 1.2\%$	640 ± 8
5	$0.31 \times 10^7 \pm 0.4\%$	$0.22 \times 10^6 \pm 1.2\%$	$0.15 \times 10^6 \pm 1.2\%$	292 ± 4

Table 5.4: The data at D_0 in 1997 is taken from [264]. Using Formula 5.4, the flux at D , including an error of 1 cm, can be estimated in 1997. Then, taking into account the attenuation of the source activity, the flux at D can be estimated at the time of the tests in GIF in 2014. Assuming a sensitivity of the RPC to gammas, $s = (2 \pm 0.2) \times 10^{-3}$ [271], an estimation of the hit rate per unit area is obtained.

3786 The goal of the study was to have a good measurement of the intrinsic RPC performance without
 3787 source irradiation. Then, taking profit of the two working absorbers, at absorption factors 5 (300 Hz)
 3788 and 2 (~ 600 Hz) the goal was to show that the detectors fulfill the performance certification of CMS
 3789 RPCs. Finally, a first assessment of the performance of the detectors at higher backgrounds was
 3790 obtained with absorption factor 1 (no absorption and >1 kHz)).

3791 5.2.4 Results and discussions

3792 The data taking at GIF has been conducted between the 21st and the 31st of August, 2014. Data
 3793 have been collected with source both ON and OFF using three different absorber settings (ABS 5, 2
 3794 and 1) in order to vary the irradiation on the RPC. For each source setting, two HV scans have been
 3795 performed with two different trigger settings. During a first scan the trigger sent to the TDC module
 3796 was the coincidence of the two scintillators composing the telescope while during a second scan
 3797 the trigger was a pulse coming from a pulse generator in order to measure the noise or gamma rate
 3798 seen by the chamber. Indeed, using a pulse generator allows to trigger at moments not linked to any
 3799 physical event and, hence, to obtain a *RANDOM* trigger on noise and gamma events to measure the
 3800 associated rates, the probability to have a pulse in coincidence with a cosmic muon being negligible.

3801 From the cosmic trigger scans, a summary of the efficiencies and corresponding cluster sizes
 3802 is shown in Figure 5.20. The efficiency curves with Source ON show a shift with respect to the
 3803 case without irradiation. With ABS 5, the general shape of the efficiency curve stays unchanged
 3804 whereas a clear alteration of the performance is observed at ABS 2 and ABS 1. From the cluster
 3805 size results, a reduction of the mean cluster size under irradiation can be observed at equivalent
 3806 efficiency. This effect can be due to the perturbation of the electric field by the strong flux of gamma
 3807 particles interacting with the electrodes. With the increasing number of photons being converted
 3808 into electrons, an increasing number of charges need to be recombined all over the volume of the
 3809 electrodes that act as capacitors. A discharge of the electrodes reduces the effective field seen in the
 3810 gas volume by introducing a voltage drop across the electrodes thickness. The constant pressure put
 3811 on the detector by the converting photons can become strong enough to uniformly affect the gain of
 3812 the detector.

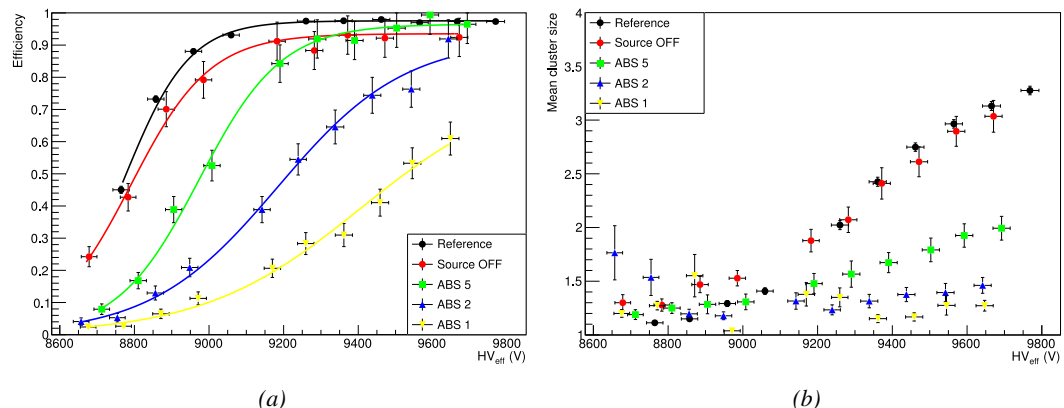


Figure 5.20: Efficiency (a) and cluster size (b) of chamber RE-4-2-BARC-161 measured at GIF with Source OFF (red) and Source ON using different absorber settings: ABS 5 (green), ABS 2 (blue) and ABS 1 (yellow). The results are compared to the Reference values obtained with cosmics.

3813 It is necessary to study the evolution of the performance of the chamber with the increasing rate
 3814 per unit area. The hit rate is measured as the number of hits detected in the RPC normalized to the
 3815 surface area of the read-out and to the total integrated time. The integrated time is linked to the time
 3816 window in which the TDC searches for data related to a trigger signal. Data is continuously kept in
 3817 the buffer of the TDCs but not all of these data is of interest. When a trigger signal is sent to the TDC
 3818 module, the TDC saves all of the data located in a certain time window set around the time stamp of
 3819 the signal. The total integrated time is then the total number of trigger signals times the width of a
 3820 search time window.

3821 In Figure 5.21a, the noise rate when the source is OFF remains low but increases at voltages above
 3822 9500 V. Aside of the natural increase of the noise with increasing voltage, the rise of the noise rate
 3823 in the detector can be related to the increased streamer probability observed with such a large electric
 3824 field. The rates measured at GIF with source ON all show a similar behaviour until a high voltage
 3825 of approximately 9400 V at which the rate of ABS 5 reaches a plateau, coinciding with the chamber
 3826 reaching full efficiency. It is important to note that, even though the rates look similar independently
 3827 from the gamma flux, relative to the efficiency of the chamber, the rate actually increases with
 3828 increasing flux at equivalent efficiency. A rough way to measure the rate effectively observed by
 3829 the detector for each source setting would be to normalize the measured rates to the efficiency of
 3830 the detector. This exercise was done with Figure 5.21b from which constant fits where done on
 3831 Source ON data in order to extract the rate the chamber was subjected to. This method leads to
 3832 rates of (164 ± 12) Hz/cm², (340 ± 26) Hz/cm² and (598 ± 50) Hz/cm² respectively for ABS 5,
 3833 2 and 1 which is consistent with the absorber values. Also, contrary to the case of the source OFF
 3834 measurement, no rise of the noise is observed at ABS 5. This difference could be explained by
 3835 the efficiency shift that is related to a decrease of the electric field across the gas volume. [But, as
 3836 **no data were taken at higher voltage values, this assumption can't be confirmed.**] Could be
 3837 confirmed by a study of the streamer probability for each dataset.

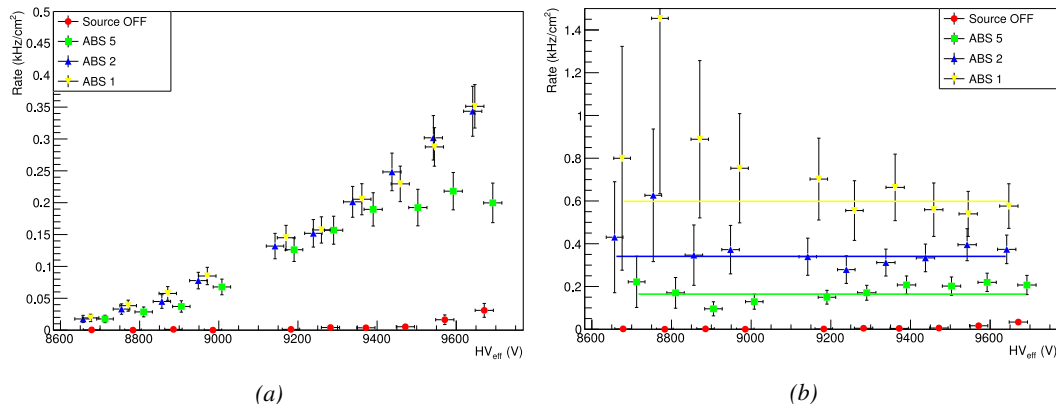


Figure 5.21: Rates in chamber RE-4-2-BARC-161 measured at GIF with Source OFF (red) and Source ON using different absorber settings: ABS 5 (green), ABS 2 (blue) and ABS 1 (yellow). On Figure (b), the rates of Figure (a) were normalized to the measured efficiency, and constant fits are performed on Source ON data showing the gamma rate in the chamber.

3838 The results need to be taken with care as a better estimation of the rate would have been to push
 3839 the detector towards higher voltages to reach the efficiency plateau for each absorber configuration
 3840 and only then extract the measured rate at working voltage, defined as in Formula 3.25. Nevertheless,

3841 using this method to estimate the rate to which the chamber is subjected, it is possible to look at the
 3842 evolution of the HV_{50} and HV_{knee} as a function of the increasing rate as showed in Figure 5.22.
 3843 The results from GIF suggest that at a rate of 600 Hz/cm^2 the working voltage of the chamber is
 3844 increased by a thousand V while the efficiency is reduced to approximately 80%, although the result
 3845 still is consistent with an efficiency better than 90% due to the large error on the measurement.

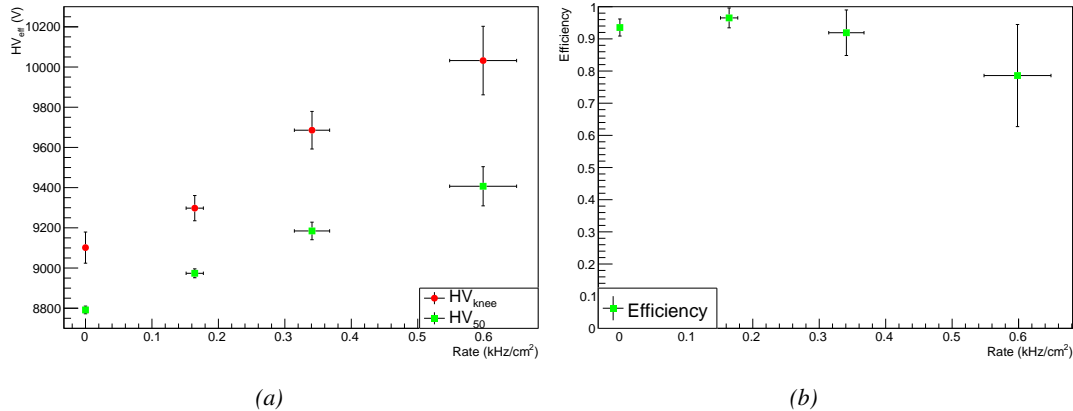


Figure 5.22: Evolution of the voltages at half maximum and at 95% of the maximum efficiency (Figure 5.22a), and of the maximum efficiency (Figure 5.22b) as a function of the rate in chamber RE-4-2-BARC-161. The data is extracted from the fits in Figures 5.20a and 5.21b.

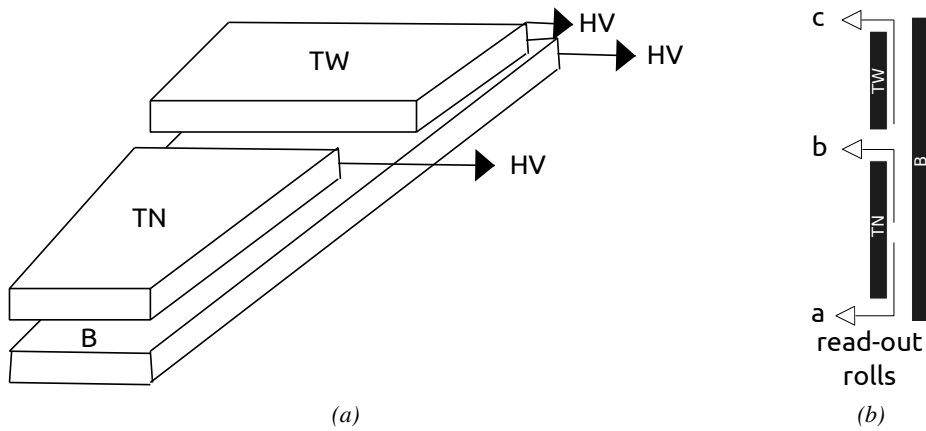


Figure 5.23: Presentation of a double-gap endcap RPC with its three RPC gaps. Due to the partitioning of the read-out strips into three rolls, the TOP layer of gap is divided into two gaps: TOP NARROW (TN) and TOP WIDE (TW). The BOTTOM (B) only consists in one gap.

3846 It is likely that the rates obtained through fitting on normalized values is underestimated. Indeed,
 3847 monitoring the current in the three gaps composing a CMS endcap RPC (Figure 5.23) while knowing
 3848 the rate, the charge deposition per avalanche q_γ can be computed. A current density, expressed in
 3849 A/cm^2 , divided by a rate per unit area, expressed in Hz/cm^2 yields a charge expressed in C. The
 3850 current driven by the RPC is assumed to be due to the irradiation, hence, to the avalanches developing

in the gas volume due to the photons of the Cesium source. On the other hand, the rate is supposed to be a measure of the number of photons interacting with the detector. This way, it comes that the charge deposition per avalanche is expressed like $q_\gamma = J_{mon}/R_\gamma$, with J_{mon} being the monitored current density and R_γ the measured γ rate. The current density is computed as the sum of the current density measured in the top and bottom gap layers, $J_{mon} = (I_{mon}^{TW} + I_{mon}^{TN})/(A_{TW} + A_{TN}) + I_{mon}^B/A_B$, with $A_{B,TN,TW}$ being the active area and $I_{mon}^{B,TN,TW}$ the monitored currents of the gaps. According to Figure 5.24, the charge deposition per avalanche consistently converges to a value of the order of 50 pC for each absorber setting which corresponds to a value more than twice larger than what reported in literature for CMS detectors [271, 272] indicating that the rates could have been wrongly evaluated during the short study performed at GIF. An increase of the γ rate by a factor 2 would actually be consistent with the expected rates calculated in Table 5.4, assuming the sensitivity to γ to be of the order of $(2 \pm 0.2) \times 10^{-3}$.

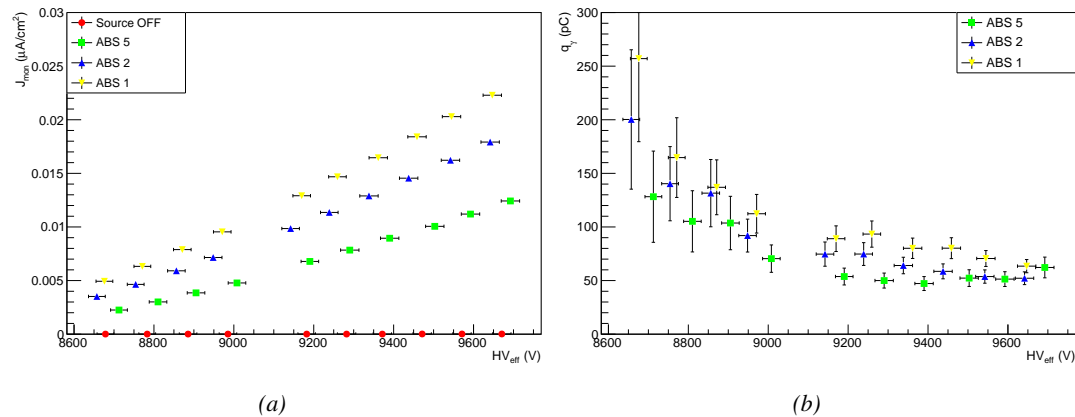


Figure 5.24: Current density (a) and charge deposition per gamma avalanche (a), defined as the current density normalized to the measured rate taken from Figure 5.21a as a function of the effective high voltage in chamber RE-4-2-BARC-161 measured at GIF with Source ON using different absorber settings: ABS 5 (green), ABS 2 (blue) and ABS 1 (yellow).

Overall, working at GIF has been a rewarding experience as it offered CMS RPC R&D team the possibility to start developing the necessary skills and tools that would become the core of GIF++ experiment. The quality of the results can be argued both due to the little robustness of the experimental setup and the lack of available statistics to draw conclusions from, bringing large errors on the final result. The confrontation of the data to known results pointed to a failure in correctly measuring the γ rate at working voltage and, hence, to an overestimation of the charge per avalanche and of the drift of working voltage with increasing rate. Nevertheless, the prototypes of DAQ and offline analysis tools proved to be reliable.

5.3 Longevity tests at GIF++

5.3.1 Selection and characterization of CMS RPCs for longevity at GIF++

In the perspective of future upgrades of LHC that would bring detectors to be operated in a high irradiation environment, the new Gamma Irradiation Facility of CERN was first proposed in 2009 [273].

3875 The Gif++ would thus provide all LHC R&D teams working on behalf of the different LHC exper-
 3876 iment with a facility to perform longevity studies using a very intense Cesium gamma source.

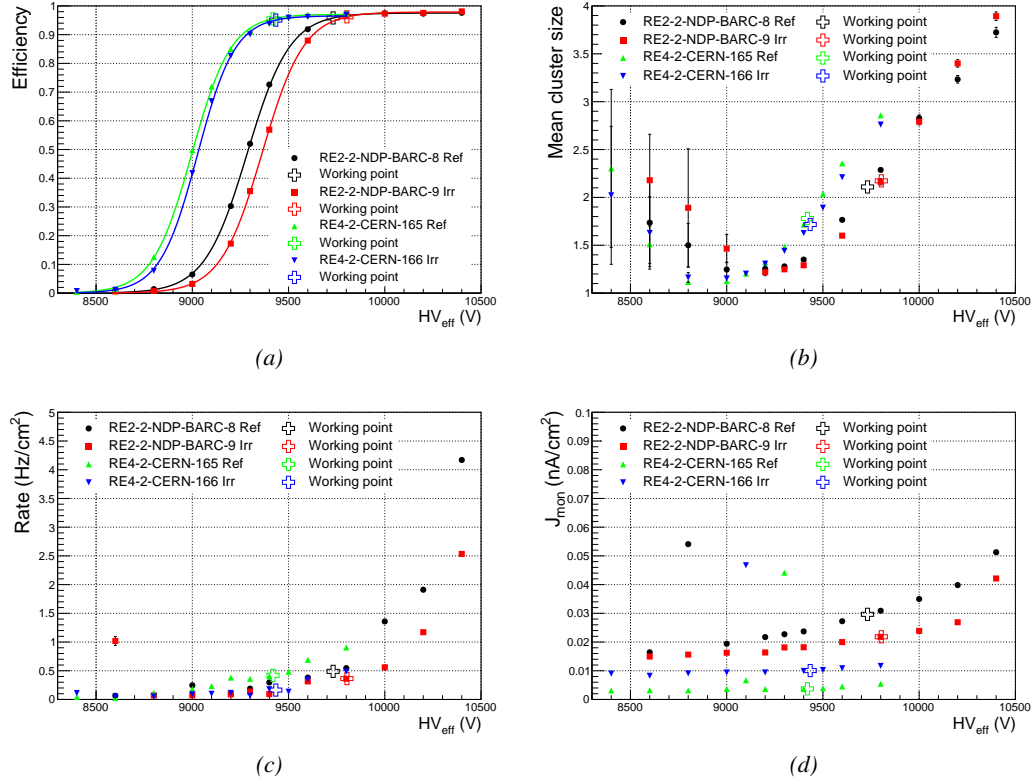


Figure 5.25: Characterization of CMS RPC detectors foreseen to be used at Gif++ for longevity studies of the present system. Using cosmic muons, efficiency (a) and cluster size (b) were measured as well as noise rate (c) and current density (d). For each detector, the working voltage, defined as in Formula 3.25 after LS1, was extracted from sigmoid fits performed in Figure (a) and the values of efficiency, cluster size, noise rate and current density at this voltage are reported using open crosses.

3877 In the specific case of CMS RPC, the longevity studies imply a constant irradiation of selected
 3878 detectors in order to accumulate a charge equivalent to what is expected during HL-LHC, i.e. a
 3879 charge of $0.8 \text{ C}/\text{cm}^2$ according to Figure 5.2 including a safety factor 3. Other detectors are left
 3880 non-irradiated to be used as references. Throughout the irradiation campaign, the performance of
 3881 the irradiated and reference detectors will be periodically probed using the high intensity H4 muon
 3882 beam. Dedicated test beam periods will be used to measure the efficiency and gamma rate at the
 3883 level of the detectors. Different source absorber settings will test the rate capability of CMS RPCs,
 3884 that needs to be certified above $600 \text{ Hz}/\text{cm}^2$. Using a muon beam will also help identifying signs of
 3885 ageing in the case the performance of the irradiated detectors diverges from those of the reference
 3886 detectors with increasing accumulated charge. Other than the performance of the detectors, signs of
 3887 ageing could come from increasing dark current that would be related to local ageing of the elec-
 3888 trodes triggered by the increased hydrofluoric acid (HF) production in an irradiated environment.
 3889 HF is produced by the decomposition of $C_2H_2F_4$ molecules during the charge multiplication pro-

cess and leads to increased dark current and noise in Bakelite RPCs treated with linseed oil. This effect is strongly reinforced by the presence of UV photons [274, 275]. A close monitoring of the current driven by the detectors will then be necessary as well as dedicated periodical electrode resistivity measurements and chromatography analyses on the gas exhaust.

As the maximum background in CMS is found in the endcap disks, the choice was made to focus the GIF++ longevity studies on endcap chambers. Most of the RPC system was installed in 2007. Nevertheless, the large chambers in the fourth endcap (RE4/2 and RE4/3) have been installed during LS1 in 2014. The HPL of these two different productions possibly having slightly different properties, four spare chambers of the present system were selected. From the original CMS RPC system, two RE2/2 spares were selected along two RE4/2 spares from the newest detectors. Having two chambers of each type allowed to always keep one of them non-irradiated as reference. Due to the limited gas flow in GIF++, the RE4 chamber remained non-irradiated until end of November 2016 when the longevity studies could finally be started on those chambers.

The performance of the chambers prior to the start of the longevity campaign was characterized in Ghent before their transportation to CERN for installation in the GIF++. The results of the characterization are showed in Figure 5.25 and summarized in Table 5.5. A clear difference in performance for both types of chambers is observed as the working voltages of the newest chambers, of type RE4, are 300 to 400 V lower to the older chambers indicating that the gap thickness of RE4 detectors could be thinner. This conclusion could as well be supported by the lower cluster size at working voltages that are also smaller in RE4 chambers. Even though the measured currents are low, RE4 detectors draw less current without irradiation than RE2 detectors pointing to a difference in electrode resistivity that were produced at different moments. Efficiency and noise rate levels are of the same order of magnitude for both type of RPCs.

RPC	RE2-2-NPD-BARC-08	RE2-2-NPD-BARC-09	RE4-2-CERN-165	RE4-2-CERN-166
Used as	Reference	Irradiation	Reference	Irradiation
HV_{WP} (V)	(9732 \pm 6)	(9803 \pm 6)	(9419 \pm 5)	(9434 \pm 5)
Efficiency at WP	(96.2 \pm 0.3)	(96.6 \pm 0.3)	(95.9 \pm 0.3)	(95.5 \pm 0.3)
Cluster size at WP	(2.19 \pm 0.04)	(2.27 \pm 0.05)	(1.88 \pm 0.04)	(1.80 \pm 0.04)
Noise at WP (Hz/cm ²)	(0.51 \pm 0.01)	(0.39 \pm 0.01)	(0.44 \pm 0.00)	(0.15 \pm 0.01)
J^{WP} (pA/cm ²)	(30.1 \pm 0.1)	(22.2 \pm 0.1)	(3.8 \pm 0.0)	(10.2 \pm 0.0)

Table 5.5: Summary of the characterization measurement performed in Ghent on CMS RPC detectors foreseen to be used at GIF++ for longevity studies of the present system. For each detector, the working voltage, defined as in Formula 3.25, was extracted from sigmoid fits performed in Figure 5.25a. The values of efficiency, cluster size, noise rate and current density at this voltage are reported.

5.3.2 RPC test setup

For an easy manipulation of the detectors, a trolley with a structure containing slots in which the RPCs can be slid vertically was used and is referred to as T1. When in position, each chamber is in a plane perpendicular to the beam line and the source flux as can be seen through Figure 5.26, and receives a uniform irradiation. Moreover the trolley allows for easy movement of the system. Indeed, the position of the trolley varies according to the specific measurements that are being done.

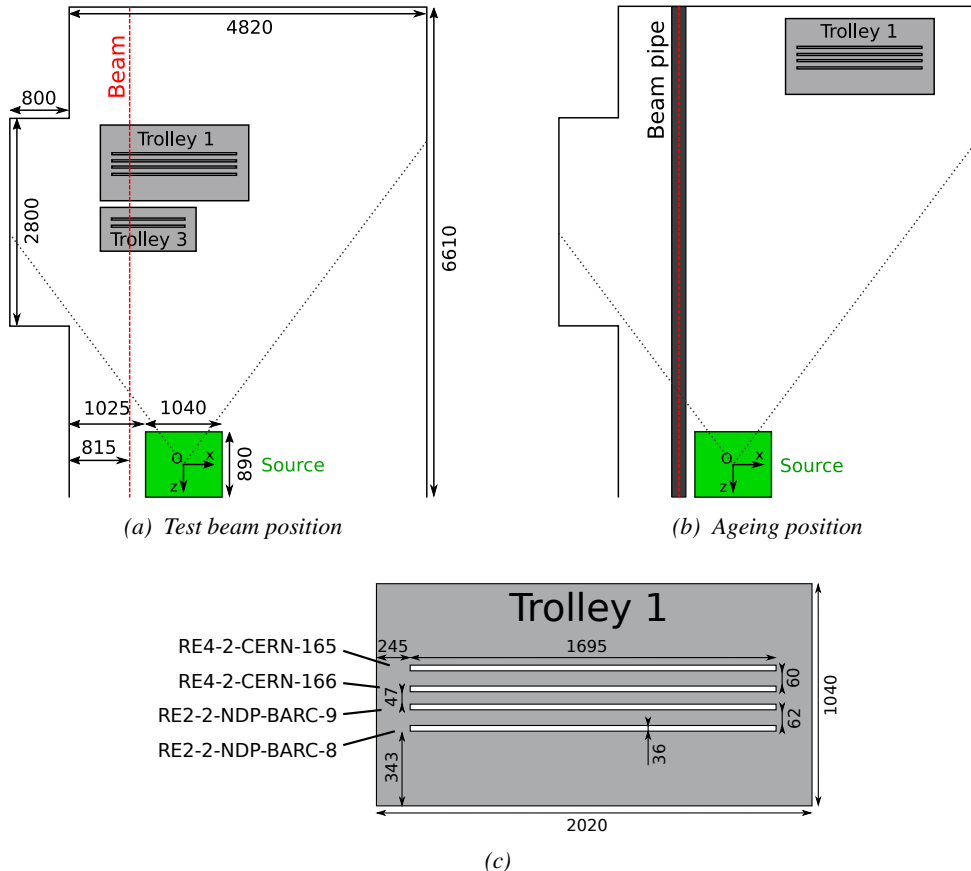


Figure 5.26: CMS RPC setup inside the GIF++ bunker during test beam (a) and ageing periods (b). The space in between the RPCs and the source is usually used by other detectors while the space in between T1 and the upstream wall is not filled. Due to the presence of the beam pipe, the trolley is moved away from the beam line during irradiation periods and placed further away from the source for less intense irradiation. The position of the trolley can vary due to the use of the space by other setups and is then not exact. Nonetheless, the position of the chambers in the trolley is fixed and given in Figure (c).

During the dedicated test beam periods, the GIF++ experiments are in control of the muon beam. The trolley is placed in the upstream region of the bunker, in the beam line at a distance of generally 3.4 m from the source, as described through Figure 5.26a. At this distance, the simulated gamma current is the order of $5 \times 10^6 \text{ cm}^{-2} \text{ s}^{-1}$. The CMS RPC detectors are the furthest away from the source as other detectors need to be certified at higher background rates. Depending on the needs of the other experiments at the GIF++, the trolley position of the trolley can be pushed as far as 4.1 m from the source. An additional trolley, referred to as T3, contains iRPCs and is placed between the source and the T1 trolley. Indeed, iRPCs need to be certified at higher rates and thus need to be placed closer to the source to receive a stronger irradiation using the same absorber settings. The space on T1 being limited, the tracking RPCs used for extra offline information during the analysis are placed on the same trolley as the iRPCs. They are kept at full efficiency at all time to reconstruct muon tracks and to correlate them with hits recorded in T1 chambers. The beam trigger system is composed of three scintillators. Two are placed outside on each side of the bunker and of the third scintillator is placed in the beam line in between T1 and the wall.

3933 Most of the year, outside of these test beam periods, T1 is placed in the so called *ageing position*
 3934 corresponding to the furthest position at approximately 4.7 m from the source outside of the beam
 3935 line before August 2019. At such a distance, the simulated gamma current is the order of 3×10^6
 3936 $\text{cm}^{-2} \text{s}^{-1}$. Following the extension of the upstream area in August 2019, the trolley was pushed
 3937 approximately 1 m away at a distance of 5.7 m to the source, corresponding to a simulated gamma
 3938 current of the order of $2 \times 10^6 \text{ cm}^{-2} \text{s}^{-1}$. During periods where GIF++ doesn't have the control of
 3939 the beam, the beam line needs to stay clear so that a beam tube can be installed through the bunker,
 3940 as can be seen in Figure 5.26b. The reason for placing the chambers as far as possible from the
 3941 source comes from the too high irradiation delivered by the source during the irradiation periods
 3942 where all the other groups having placed detectors in the bunker require as much charge integration
 3943 as possible. Hence, the source is operated without any absorbers. On the contrary, during the test
 3944 beam periods, all the groups working in GIF++ are interested in operating the source using various
 3945 absorber settings to study the performance of their detectors under different irradiation conditions.
 3946 T1 RPCs are kept at a stanby voltage of 6500 V when the other groups need to work with ABS 1
 3947 due to the proximity of the trolley to the source compared to ageing periods.

3948 From the bunker area, long cables and pipes running through the wooden floor connect the de-
 3949 tectors to the service area, visible in Figure 5.6. The service area hosts all the high and low voltage
 3950 power supplies, the TDCs and computers used for data acquisition and preliminary offline analysis.
 3951 The gas system required for the gaseous detectors installed in GIF++ can also be found in the service
 3952 area [276].

3953 The detectors read-out is, as in the case of GIF, connected to V1190A VME TDCs communicating
 3954 with the DAQ computer via a V1718 VME bridge manufactured by CAEN. At the end of each data
 3955 tacking, the preliminary analysis is run to fill the Detector Control Software webpage, referred to as
 3956 WebDCS, with Data Quality Monitoring (DQM) histograms. The WebDCS is a custom made DCS
 3957 application for the specific case of GIF++ RPCs. It provides online information about the environ-
 3958 mental parameters in the bunker as well as the state of each detector. A constant monitoring of
 3959 all the environmental parameters, in different points of the bunker area, gas parameters, to control its
 3960 composition, temperature and pressure, and of the voltages and currents delivered by the power sup-
 3961 plies is performed and displayed on the homepage of the WebDCS interface. Moreover, it contains
 3962 the database with all the RPC data in the form of ROOT files and of summary hisograms. Hence, it
 3963 is a useful tool for the shifters on duty in the control room located farther in the building, away from
 3964 the beam lines.

3965 5.3.3 GIF++ data flow

3966 At GIF++, the CMS RPC R&D setup collects different types of data from the detector monitoring
 3967 parameters, such as voltage and currents, the gas, source, and environmental parameters, and, of
 3968 course, the TDC data related to the actual muon and gamma measurements. These different data
 3969 sources correspond to three different data flows as presented in Figure 5.27.

3970 The *Data Interchange Protocol (DIP)* flow, DIP being a communication system allowing for
 3971 exchange of real-time information between systems [277], concerns all the data coming from the
 3972 gas composition, temperature and humidity, the environmental temperature and pressure, the source
 3973 settings and the radiation monitoring sensors. At the experimental area, all data of interest for all of
 3974 the users of the facility (source settings, radiation monitoring, gas composition at the exit of the gas
 3975 mixer and general environmental information) are measured, distributed and also stored in the data
 3976 of the experimental hall where is located the GIF++. Access to the database is done through DIP

3977 communication. The measurement of more specific data such as gas flow, temperature and humidity
 3978 at the level of the detectors (upstream and downstream of the detectors) as well as environmental
 3979 parameters has to be arranged by the users themselves. For this reason, several pressure, tempera-
 3980 ture and humidity sensors were installed on the gas distribution system of the RPC trolleys. The
 3981 corresponding data flow, although not related to DIP itself, is saved together with the DIP data into
 3982 the local CMS RPC database and displayed on the front page of the WebDCS. In the case any of
 3983 the measured values go out of their optimal range, the WebDCS will produce corresponding alerts.
 3984 The data are particularly important to perform the PT correction described in Section 3.4 of Chap-
 3985 ter 3 and to stabilize the effective voltage of the detectors. Monitoring history plots are made using
 3986 JavaScript are also displayed for easy access to past information, as shown in Figure 5.28.

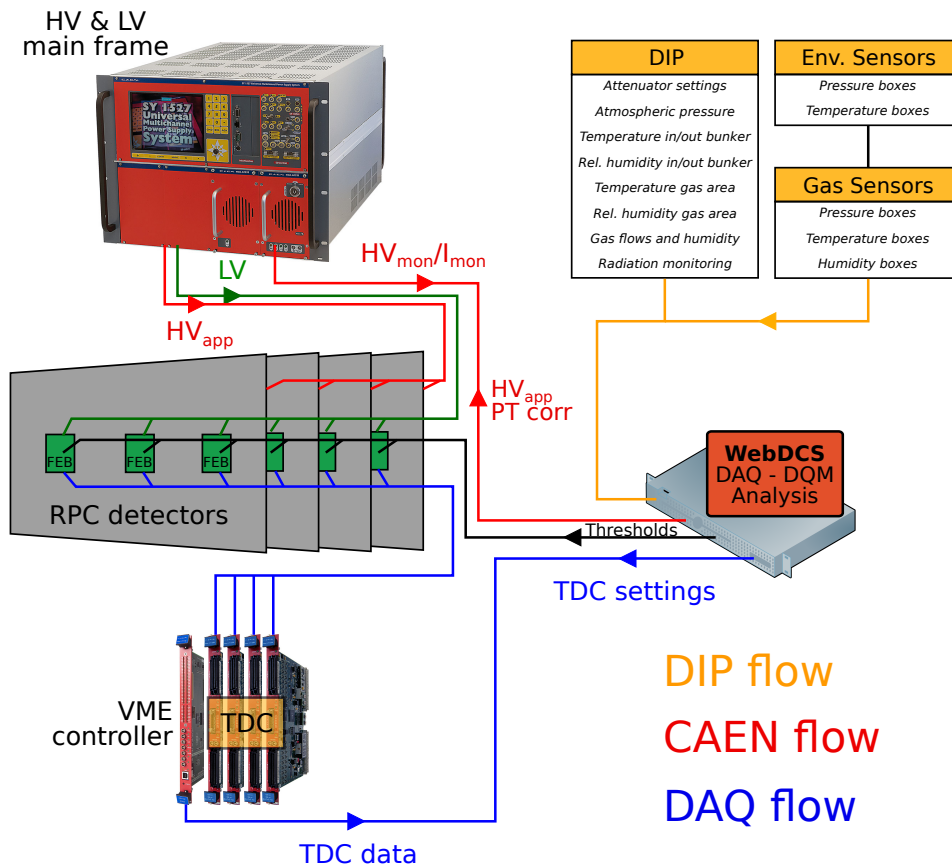


Figure 5.27: Visualisation of the main data flows in the CMS RPC setup at the Gif++. The yellow flow lines correspond to the DIP flow used for source, environmental and gas information. The red flow lines are for the CAEN flow through which the WebDCS communicates the voltages to be applied on the detectors using pressure and temperature information and retrieves the monitored voltages and currents. Finally, the blue flow lines correspond to the DAQ flow through which the RPC data is collected from the TDCs by the computer.

3987 The data flow related to the monitoring of the detector high voltages and currents, referred to
 3988 as *CAEN flow* as a reference to the manufacturer of power supplies, is handled through direct com-
 3989 munication between the DAQ computer and the power supply main frames. Finally, the DAQ flow
 3990 concerns all data acquired through the use of the TDCs, i.e. all the muon or gamma event data

3991 recorded by the detectors under test at GIF++. It was already discussed that when a trigger signal is
 3992 sent to a TDC module, the TDC saves all of the data located in a certain time window set around the
 3993 time stamp of the signal. The trigger signal in the case of GIF++ can be a coincidence of the trigger
 3994 scintillators or a signal from a pulse generator. The DAQ computer extracts from the TDC buffers the
 3995 list of fired channels and of associated time stamps for each trigger signal. The data is then used to
 3996 reconstruct muon tracks along the CMS RPC setup at the GIF++ or to compute the noise and gamma
 3997 rates associated to a certain source setting.

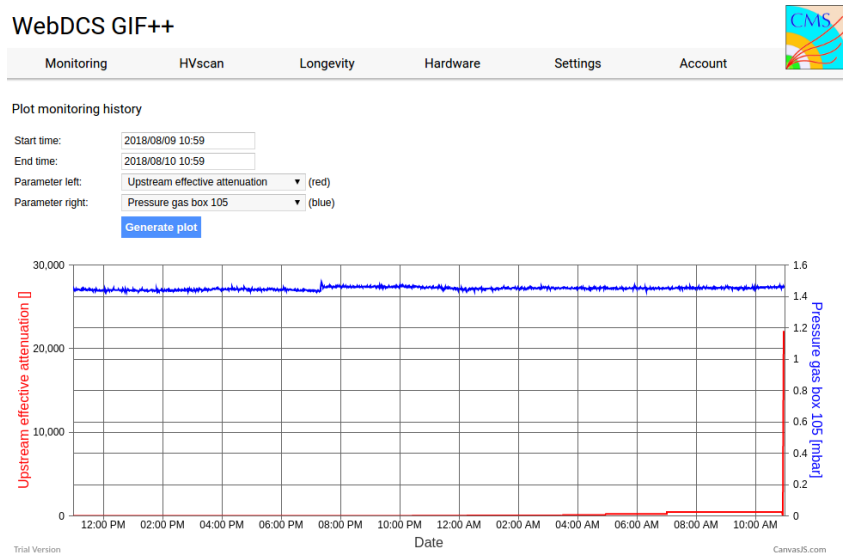


Figure 5.28: DIP monitoring history accessed through the GIF++ WebDCS interface.

3998 5.3.4 Measurements performed during beam periods

3999 As previously described, two types of measurements are performed on the chambers during beam
 4000 periods. On the one hand, it is interesting to measure the efficiency of the RPCs with increasing
 4001 voltage with different source absorber settings but on the other hand, it is important to correlate the
 4002 efficiency information to the gamma rate seen by the chambers at the different voltages. The choice
 4003 was made to separate efficiency measurements from rate measurements to better manage time and
 4004 data volume. In both cases, TDC data recorded during so called *HV scans* is divided into *runs*, one
 4005 for each high voltage point, whose data is stored into ROOT files. The TDC settings used during
 4006 both these scans as well as the ROOT data structure are detailed in Section A.4.2 of Appendix A.

4007 The goal of both efficiency and rate scans is to measure the rate capability of the detectors but
 4008 also to monitor any degradation of the performance due to ageing. This way, during test beam
 4009 periods the efficiency and corresponding gamma background are measured to correlate the evolution
 4010 of rate capability at different stages of irradiation. In the absence of other signs of ageing, a reduction
 4011 of the rate capability could be related to an increase of the electrodes resistivity.

5.3.4.1 Efficiency scans

The HV scans performed to specifically measure the muon detection efficiency under different irradiation conditions follow a standardized procedure. Data using the DAQ is taken at the same 12 HV points for all chambers, ranging from 9 kV to 10.1 kV in steps of 100 V. For each HV run, a minimum of 5000 muon beam triggers, provided by the coincidence of the three scintillators, is required in order to accumulate enough statistics for a reliable computation of the efficiency of the detectors. In addition to the four RPCs held on T1, two tracking RPCs installed on T3 are kept at a fixed voltage of 9.7 kV to provide the analysis software [278] with beam position information to exclude off-track signals. The tracking RPCs are double gap detectors featuring 2 mm HPL electrodes and 2 mm gas gaps. They are prototypes built by the italian company *General Tecnica* using a different production of HPL. Finally, the monitored currents and voltages are recorded in histograms along with the TDC data in a different ROOT file for each run.

HV scans are taken for different source settings as the goal is to irradiate all the detectors with a minimal rate of 600 Hz/cm². Usually, a full study of the performance of the detectors is performed with Source OFF, and then with nine absorber settings that attenuate the nominal gamma flux by factors from more than 200 to only 3, where settings with fully opened source are avoided with RPCs in test beam position. During the efficiency scans, the cluster size is also measured and the currents are monitored as can be seen in Figure 5.29.

5.3.4.2 Rate scans

The background measurements are performed using a similar HV scan procedure as for the efficiency measurements. The HV scan in test beam periods is taken at fewer HV points compared to the efficiency scans as the region of interest is located around the knee and efficiency plateau of the detectors, i.e. these scans are performed only on six HV points ranging from 9.5 kV to 10 kV. The value of the rate at the operating voltage is then deduced from the efficiency scan through linear

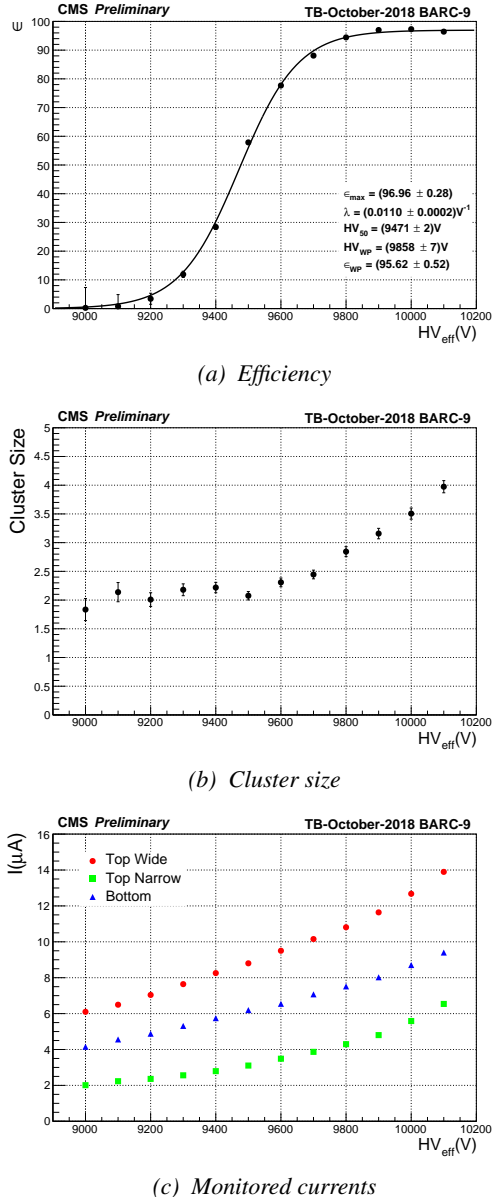


Figure 5.29: Example of results obtained during an efficiency scan performed with ABS 113 (4.6) during October 2018 testbeam period.

4056 interpolation. A good estimation of the rate requires a long enough integrated time of the TDC data.
 4057 The way data is collected, detailed in Appendix A, makes the DAQ search for data stored in the TDC
 4058 buffers prior to the trigger signal. The time window from which the data can be collected ranges from
 4059 25 ns to more than 50 μ s. With the Cesium source delivering a constant gamma flux, it was decided
 4060 that a total integrated time of 0.2 s would be enough to have a reliable calculation of the gamma
 4061 rate. This is achieved by taking 20,000 random trigger pulses delivered by a pulse generator at a
 4062 frequency of 300 Hz while extracting 10 μ s of data from the buffers for each trigger. An example
 4063 of the data obtained during rate scans is showed in Figure 5.30 in which the hit multiplicity at a
 4064 single HV step of a scan, used to compute the rate per unit area, is showed together with the rates as
 4065 computed at every HV steps.

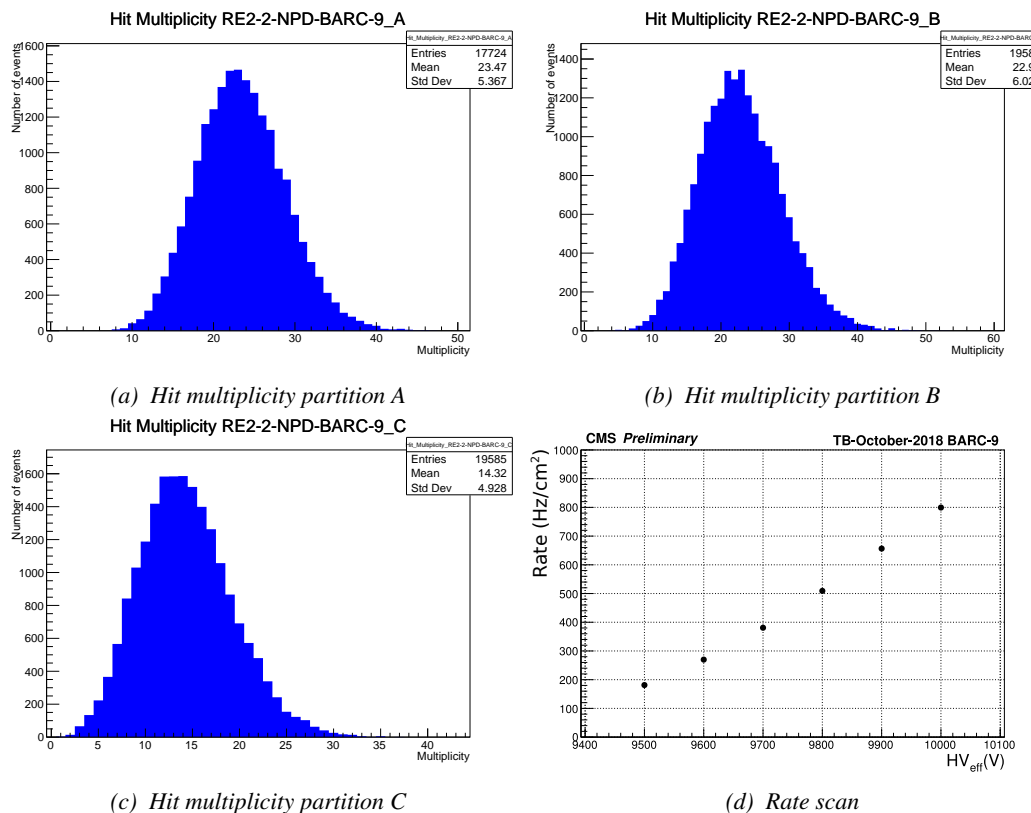


Figure 5.30: Example of results obtained during an efficiency scan performed with ABS 113 (4.6) during October 2018 testbeam period. The hit multiplicity histograms (a), (b) and (c) correspond to the fourth HV point of the scan at 9800 V.

4066 Separating the rate and efficiency measurements was motivated by the inconsistency of the muon
 4067 beam provided in Gif++². Using periods without beam to measure rates with a good statistics allows
 4068 for faster study programs. Moreover, the number of muons per beam spill depends strongly on the
 4069 user setups placed upstream of the Gif++ and on the specific beam optic magnet settings. Collecting

²During test beam periods, the delivery of the muon beam at the SPS North Area depends on the LHC program. As the SPS is used to feed the LHC with accelerated protons, the priority is given to the LHC. Other than the LHC, the delivery of muon beams can also be stopped due to maintenance or breakdown on the acceleration lane. This may translate into long periods with low intensity beams or even without any beam at all.

4070 20,000 events could then take too long for the other users at the Gif++. Hence, efficiency scans are
 4071 performed with lower statistics, and the time window from which the TDC data are extracted is
 4072 strongly reduced (400ns for efficiency scans versus 10 μ s for rate scans) to keep the data size to its
 4073 bare minimum.

4074 **5.3.4.3 Offline analysis and Data Quality Monitoring**

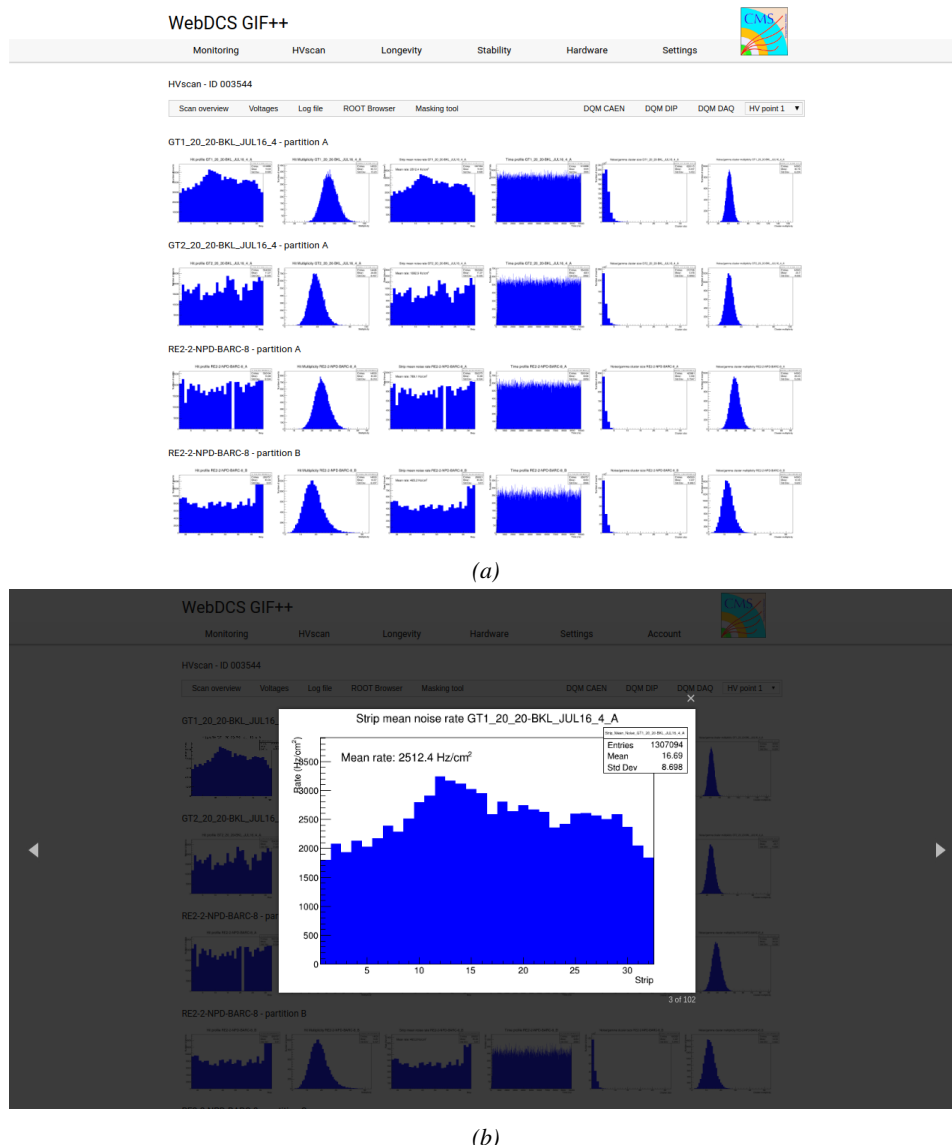


Figure 5.31: Example of DQM page available on CMS RPC WebDCS at the Gif++: the histogram of the rate measured in one of the tracking chambers, namely GT1_20_20_BKL_JUL16_4, is selected and displayed above the page.

4075 The data recorded during efficiency and rate scans always consists of two ROOT files per run, where
 4076 each run corresponds to a certain HV point. One of the files contains the TDC data, a collection
 4077 of hits and time stamps per active channel on the read-out of the RPCs, while the second is the
 4078 CAEN main frame data, i.e. the detector currents and high voltages. The data are systematically
 4079 analysed at the end of each scan using the Offline Analysis tool of GIF++, detailed in Appendix B,
 4080 that produces histograms such as hit, rate and time profiles, hit multiplicities, gamma cluster sizes or
 4081 multiplicities for the DQM display of the WebDCS, as shown in Figure 5.31. More histograms can be
 4082 accessed through the ROOT browser included in the WebDCS, as shown in Figure 5.32. Moreover,
 4083 the analysis performed with the Offline tool provides final results for the rate scans. On the contrary,
 4084 the algorithm for efficiency calculation is kept simple and approximative in the tool. Including
 4085 tracking into the analysis requires manual adjustment for each individual scan as the positions of the
 4086 trolleys with respect to each other may vary.

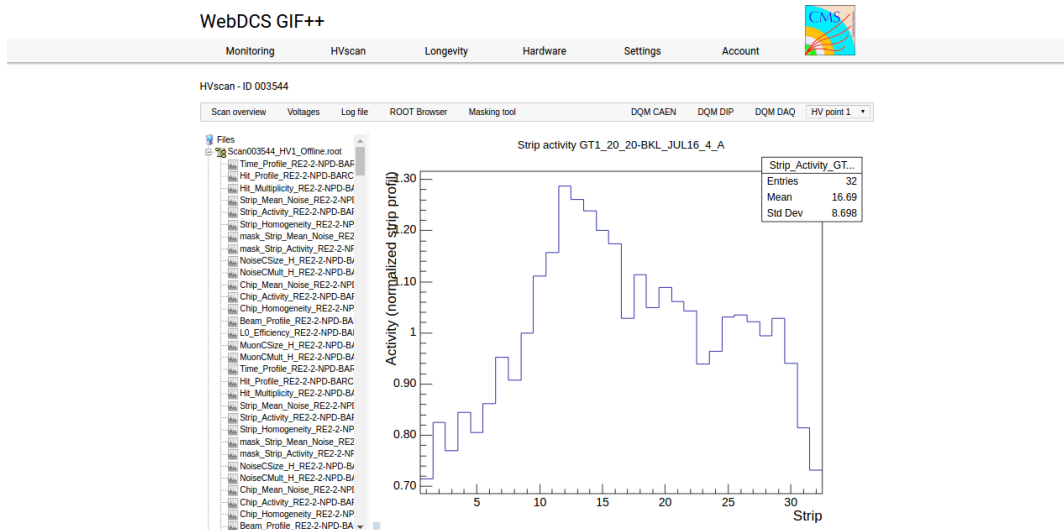


Figure 5.32: Example of DQM ROOT Browser page available on CMS RPC WebDCS at the GIF++: the strip activity profile, defined as the rate profile normalized to the mean rate, in one of the tracking chambers, namely GT1_20_20-BKL_JUL16_4. Available ROOT files and histograms can be browsed thanks to the left panel showing the directory and files structures.

4087 5.3.5 Measurements performed during irradiation periods

4088 Even though test beam periods are stressful times as an extensive data taking program needs to
 4089 be finalized in a short amount of time, the biggest amount of data actually comes from irradiation
 4090 periods. Indeed, when T1 is moved back to its ageing position in between each test beam periods,
 4091 data is recorded at any time the source can be switched ON for irradiation. Other experiments in the
 4092 area might prevent the source from staying open continuously. As an example, the time efficiency
 4093 of irradiation of CMS RPC detectors in GIF++ is presented in Figure 5.33.

4094 Several types of measurement are performed throughout the irradiation period. As long as the
 4095 detectors are being irradiated, a monitoring of the currents is performed to evaluate the corresponding
 4096 integrated charge over the total irradiation time. Moreover, in order to spot any signs of ageing, the

4097 gamma rates seen by the chambers at the chosen source absorber setting as well as the noise rates
 4098 and dark currents are periodically measured. During irradiation periods this is looked at every week
 4099 via HV scans performed at various source settings. The weekly scans involve both the irradiated but
 4100 also the reference chambers, providing with a weekly monitoring of the evolution of the irradiated
 4101 chambers noise, gamma rate and dark current. Measuring with all detectors at the same time also
 4102 allows getting rid of potential systematics that might make the rates (noise or gamma) vary from one
 4103 measurement to another. If such systematic effects occur, they will be observed in all detectors.

4104 Finally, the resistivity is measured periodically during the year, generally before or after test
 4105 beam periods, by the use of Argon breakdown technique. The method consists in filling the detector
 4106 volume with Argon instead of the CMS standard gas mixture and to increase the voltage while
 4107 monitoring the current. Beyond an electric field of about 1 kV mm^{-1} at the GIF++ environmental
 4108 conditions, Argon turns into a conductive plasma and does not offer electric resistance anymore. The
 4109 monitoring of the currents beyond the breakdown voltage can then be used to calculate the resistivity
 4110 of the electrode material.

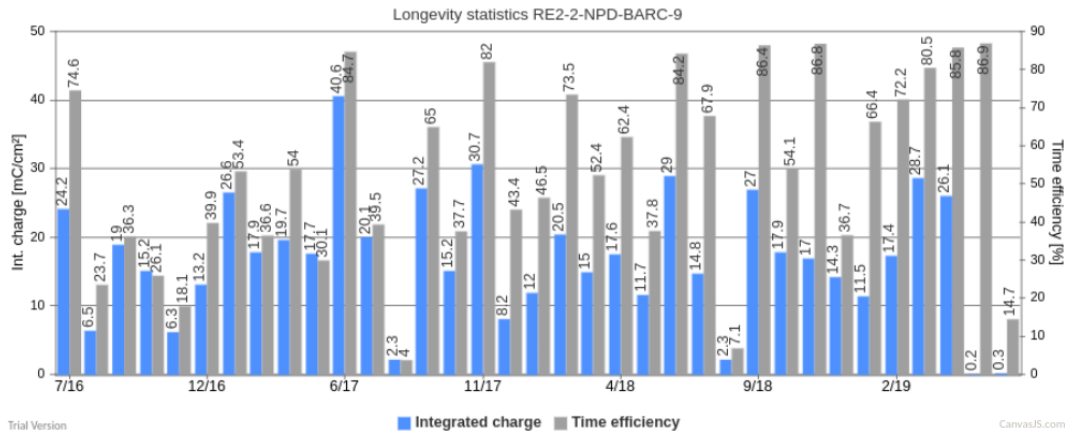


Figure 5.33: Longevity data for chamber RE2-2-NPD-BARC-9 in GIF++. For each month since July 2017, the integrated charge (in blue) as well as the time efficiency of irradiation (in gray) is reported.

4111 5.3.5.1 Longevity scans

4112 The main activity of irradiation periods consists of the *longevity scans* during which the currents of
 4113 the irradiated chambers are continuously monitored. The two irradiated chambers, RE2-2-NPD-BARC-09
 4114 and RE4-2-CERN-166, are both brought to a voltage of 9.8 kV while the source flux can vary de-
 4115 pending on the needs of the groups using the facility. The currents are monitored for each active
 4116 gas volume as can be seen in Figure 5.34. The integrated charge for each individual gas volume
 4117 is computed by integrating through time the current density, current normalised to the surface area,
 4118 flowing through each gap, as shown in Figure 5.35.

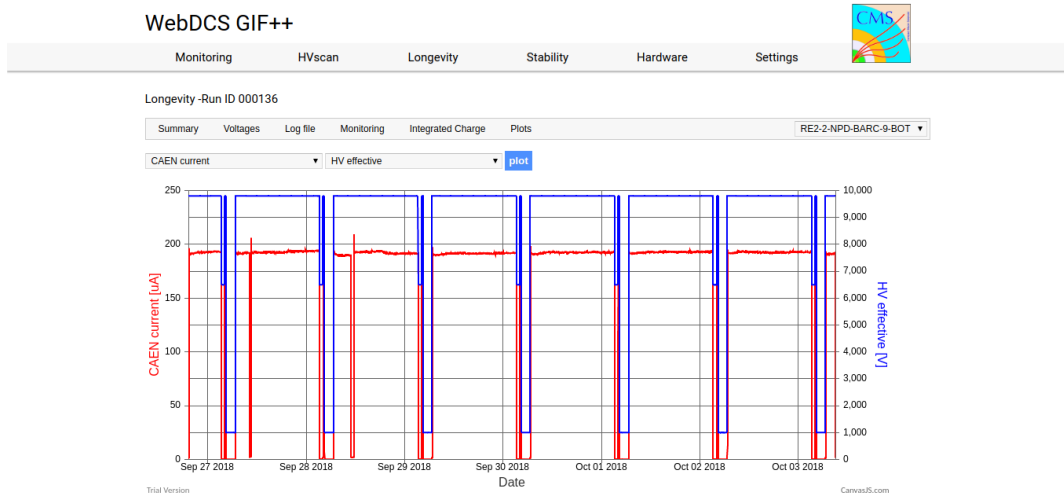


Figure 5.34: Example of a longevity scan monitoring page available on CMS RPC WebDCS at the GIF++: the current and effective voltage, as well as environmental parameters, are monitored for the bottom gap of chamber RE2–2–NPD–BARC–9. The decrease of current is related to a decrease of the voltage due to the daily rate scan procedure or to periods during which the source was turned OFF.

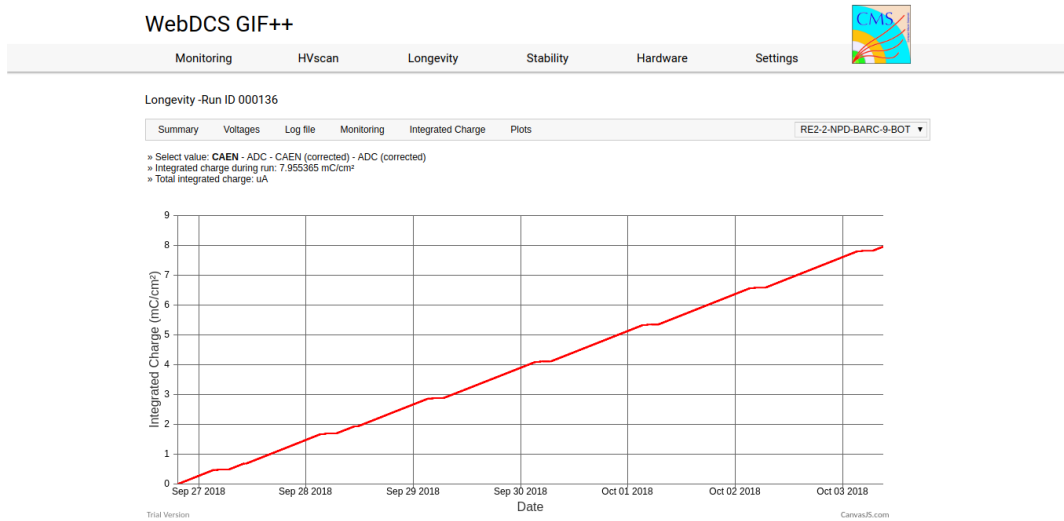


Figure 5.35: Example of a longevity scan summary page available on CMS RPC WebDCS at the GIF++: the integrated charge is computed for the bottom gap of chamber RE2–2–NPD–BARC–9.

Finally, at the end of each longevity scan each gap contribution is translated into the mean chamber integrated charge. The integrated charge accumulated in each chamber is used to update the

summary plots providing the collaboration with official results to be spread as can be seen from Figure 5.36. The translation from individual gap currents to total integrated charge in the chamber is done using Equation 5.5, where the equation to compute the monitored current density already mentioned in Section 5.2.4 is recalled.

$$(5.5) \quad J_{mon} = \frac{I_{mon}^{TW} + I_{mon}^{TN}}{A_{TW} + A_{TN}} + \frac{I_{mon}^B}{A_B}$$

$$Q_{int} = \int_{t_i}^{t_f} J_{mon} dt$$

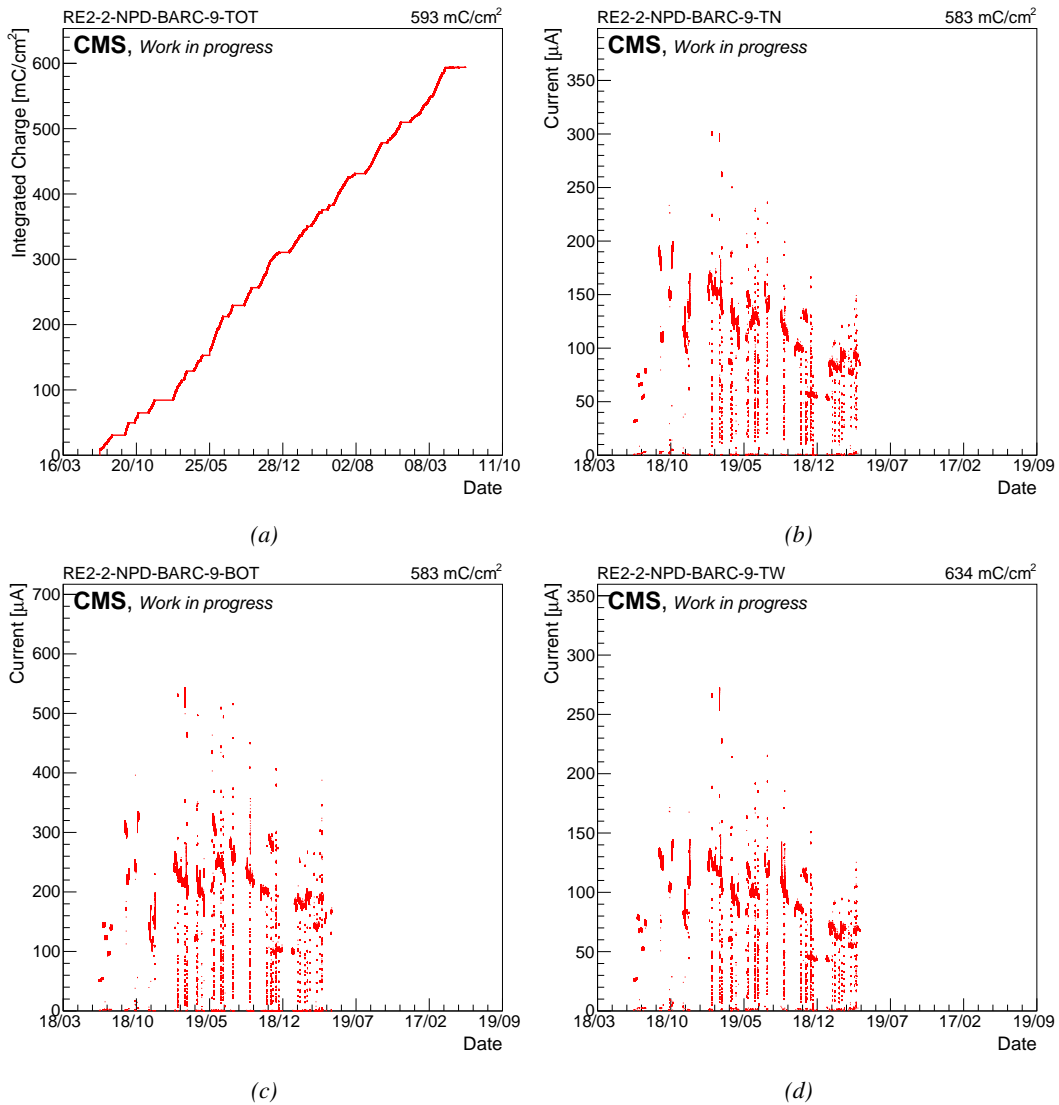


Figure 5.36: Example of current monitoring summary (top wide (a), top narrow (b) and bottom (c) gap currents) and of corresponding integrated charge (d) of chamber RE2-2-NPD-BARC-09.

4125 5.3.5.2 Daily rate monitoring scans

4126 Every night during longevity scans, the setup performs *daily rate scans*. These scans aim at keeping
4127 track of the gamma rate measured in the irradiated RPCs during longevity scans, but are also used
4128 to measure the noise rate at standby voltage for each gap. The procedure for these HV scans consist
4129 of nine runs for which 50,000 random triggers are accumulated, corresponding to 0.5 s of total
4130 integrated time.

- 4131 1- All gaps are first left at the irradiation voltage of 9.8 kV to measure the gamma rate.
- 4132 2- Then all gaps are brought to the standby voltage of 6.5 kV to measure the noise rate of the full
4133 detectors.
- 4134 3- Both top gaps (TW and TN) are brought to a voltage equivalent to an OFF status, i.e. 1 kV so
4135 that the noise contribution of only the bottom gap at standby voltage can be measured.
- 4136 4- The bottom gaps are ramped up toward the working voltage of 9.8 kV to measure their contri-
4137 bution to the gamma rate estimation.
- 4138 5-8 The steps 3 and 4 are repeated on TN and then on TW, keeping the bottom and the top gap
4139 which is not of interest at a voltage of 1 kV. This way, the individual contribution to the noise
4140 and gamma rates are known.
- 4141 9- Both TW and TN are brought to working voltage while the bottom gap is left at 1 kV to
4142 measure the gamma rate for the full top layer at once.

4143 Finally, the voltages of all gaps are brought back to working voltage for the longevity program to
4144 continue until the next daily scan. These scans are responsible for the drop of voltages and currents
4145 observed in Figure 5.34. The procedure previously described is highlighted in Figure 5.37.

4146 Similarly to the efficiency and rate scans taken during test beam periods, the data is here stored
4147 in two separate ROOT files for the TDC and CAEN data for each run. At the same time, the currents
4148 are still monitored by the longevity scan and saved into the GIF++ database for an easy evaluation
4149 of the currents to the integrated charge. The Offline Analysis tool then provides the DQM page with
4150 histograms, and daily values can be compiled into long term monitoring plots to study the variations
4151 of rate and current with increasing integrated charge, as presented in Figure 5.38. The variations
4152 of the rate and current are correlated and correspond mainly to change of source irradiation, gas
4153 flow, gas humidity, or environmental conditions. The rates on every single read-out channel are
4154 also tracked to control their activity with increasing integrated charge and, this way, understand
4155 the appearance of hot spots through noisy channels, as shown in Figure 5.39. The activity of a
4156 strip is defined as the rate of the individual channel normalized to the mean rate measured in the
4157 corresponding read-out partition.

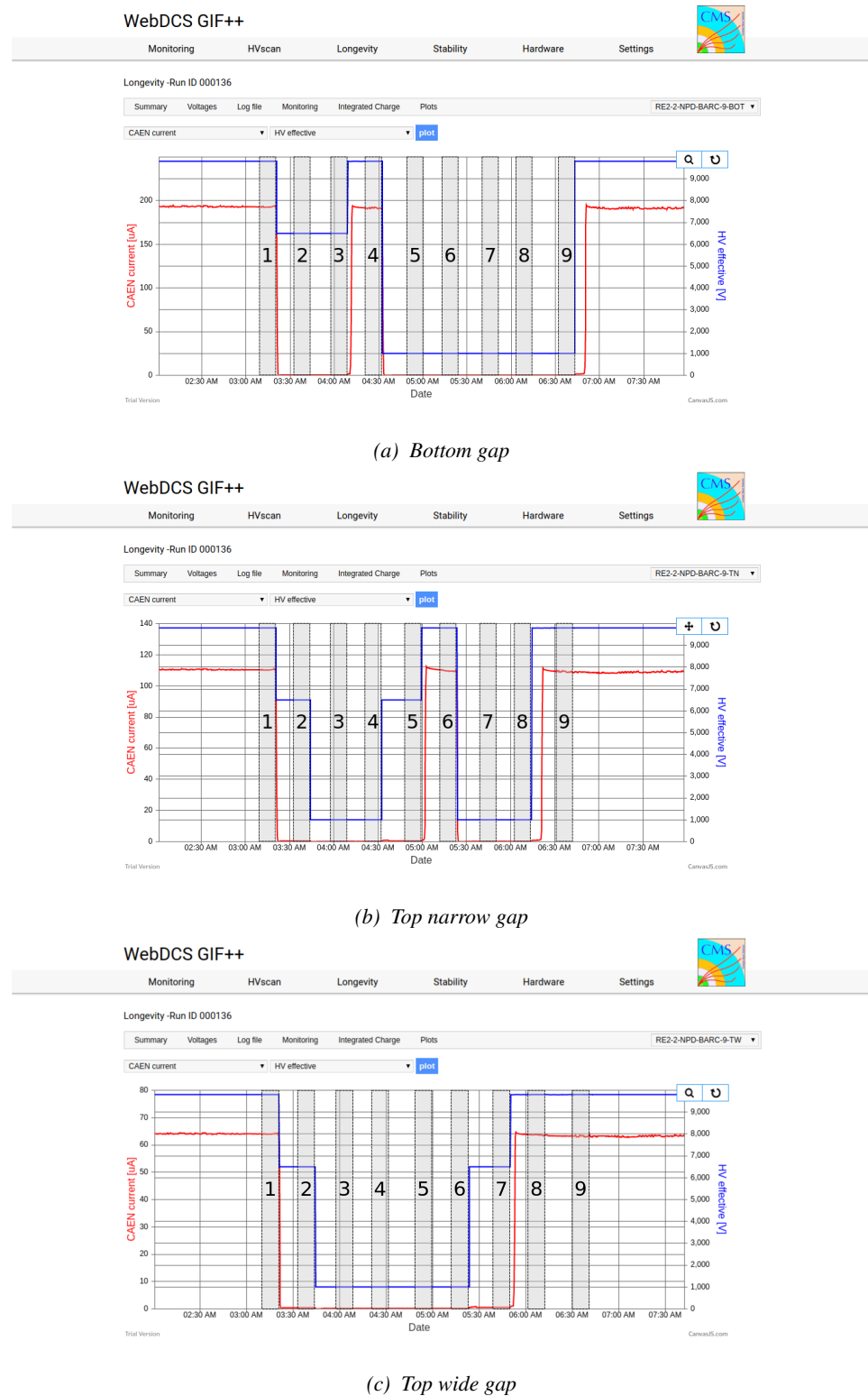


Figure 5.37: Example of daily scan procedure of chamber RE2-2-NPD-BARC-09 with highlighted runs on the CMS WebDCS at the GIF++.

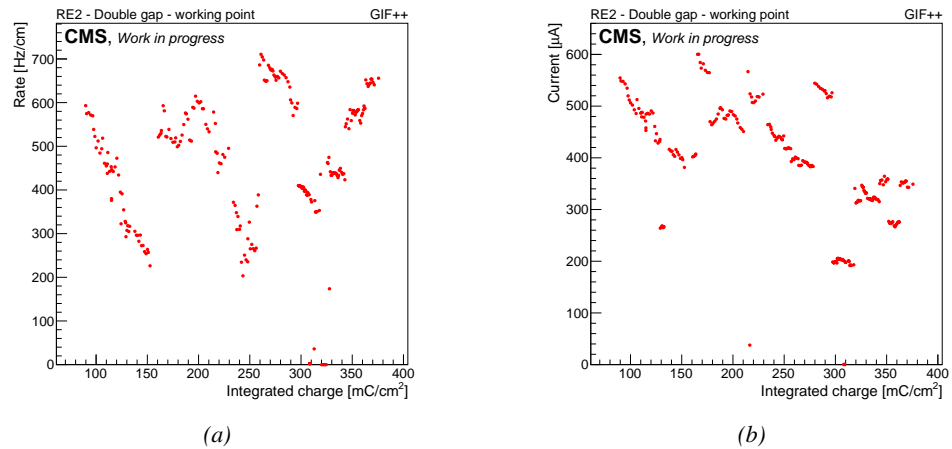


Figure 5.38: Example of rate (a) and current (b) monitoring of chamber RE2-2-NPD-BARC-09 at working voltage in double gap mode (step 1) with increasing integrated charge.

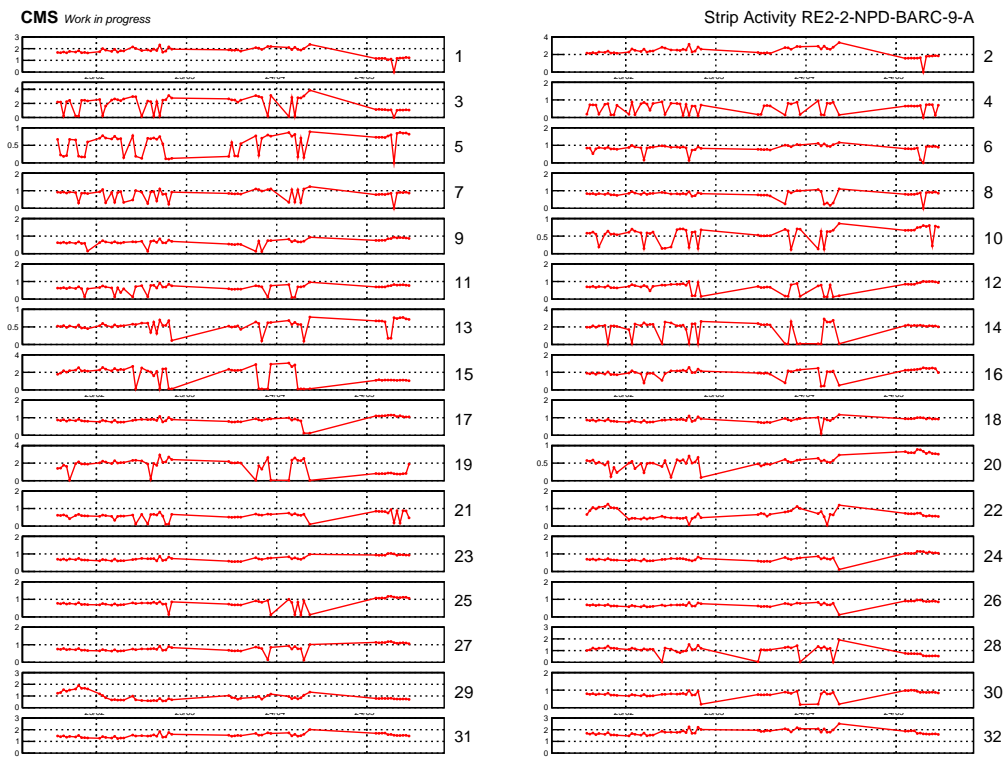


Figure 5.39: Example of strip activity of chamber RE2-2-NPD-BARC-09 monitored over time.

4158 5.3.5.3 Weekly noise monitoring scans

Once a week, the source is turned OFF to make a noise scan for the CMS RPC. This HV scan is composed of six runs for which 25,000 random triggers are accumulated. The first run is taken at

standby voltage and the second one at 8 kV. The next five runs are taken at voltages ranging from 9.4 to 9.8 kV in order to access for both type of chambers, RE2 and RE4, in the voltage region where the efficiency rises and reaches its plateau. The whole procedure is shown in Figure 5.40. On the occasion of this scan, the ongoing longevity scan is stopped. A new one will be started once the weekly scans are over.

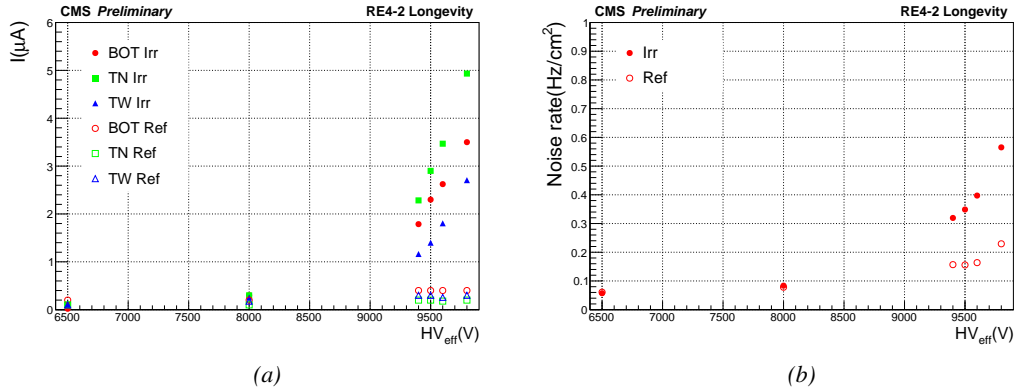


Figure 5.40: Example of rates (a) and currents (b) of irradiated chamber RE4-2-CERN-166 and reference chamber RE4-2-CERN-165 measured during a weekly noise scan.

5.3.5.4 Weekly source scans

Directly following the weekly noise scans, HV rate scans are organised at different source settings (usually ABS 6.8, 4.6 and 3.3). The procedure of these HV scans consists of nine runs for which 25,000 random triggers are accumulated. The first run is taken at standby voltage while the next eight runs are taken at voltages ranging from 9.4 to 10.1 kV. They aim at measuring the gamma rate to which the chambers are subjected and the related currents. The whole procedure is shown in Figure 5.41.

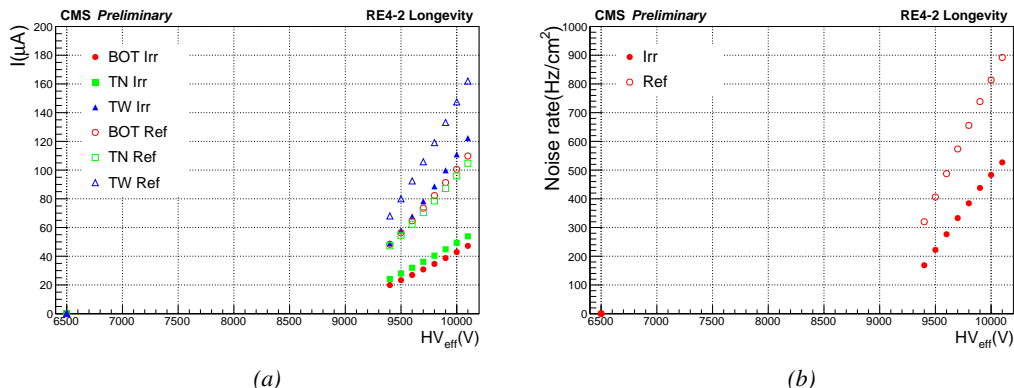


Figure 5.41: Example of rates (a) and currents (b) of irradiated chamber RE4-2-CERN-166 and reference chamber RE4-2-CERN-165 measured during a weekly source scan. The data were measured with ABS 123 (6.9).

5.3.5.5 Weekly current scans

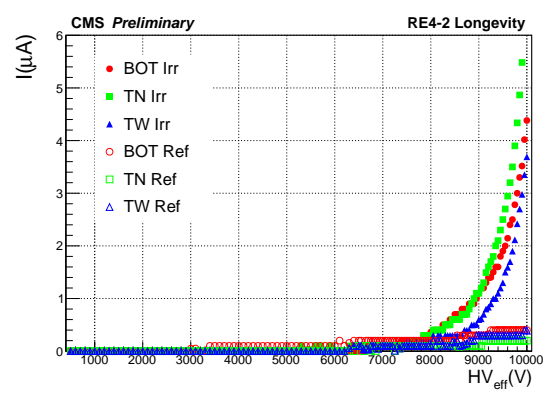


Figure 5.42: Example of currents of irradiated chamber RE4-2-CERN-166 and reference chamber RE4-2-CERN-165 measured during a weekly current scan.

procedure includes measurements at 131 high voltage points in between 500 V and 10 kV, in steps of 100 V until the standby voltage of 6.5 kV is reached and then in steps of 50 V. At low voltage, the current rise is slow and is only driven by the resistance of the detector electrode and thus increases linearly. It is referred to as the *ohmic current* as opposed to the *physics current* corresponding to the voltage region where charge multiplication starts to occur. A fit on the ohmic current range gives access to the resistance of the 'electrodes/gas' system. If any variation of the electrode resistance occurs, the global resistance will increase and so will the current. Technically, these scans will record a ROOT file per HV step that will have the same format as the CAEN ROOT file saved during other HV scans. The data is also analysed using the Offline Analysis tool to provide with DQM histograms as well as standardized I/V tables.

5.3.6 Extraction and monitoring of the resistivity

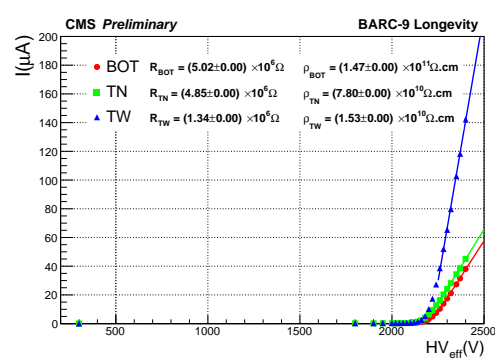


Figure 5.43: Example of currents of irradiated chamber RE2-2-NPD-BARC-09 measured during an argon scan. The resistance is extracted from the linear fit and the resistivity is computed using Equation 5.6.

the couple of electrodes R_{elec} is extracted as can be seen from Figure 5.43. The resistivity is then

The previously detailed daily rate scans, but also the weekly noise and source scans are interesting tools to look at an increase of noise rates and dark currents or at a loss of rate capability. They could point to an increase of surface resistivity of the electrodes through the absorption of hydrofluoric acid. Nevertheless, periodically measuring the currents on wider high voltage ranges allows to have access to the ohmic part of the current driven by the detectors related to the electrodes resistance. This is why precise current scans, consisting only in measuring the current driven through the four detectors, are performed each week. The scan pro-

A critical parameter to monitor is the resistivity of the electrodes. Its variation would impact the rate capability of the RPC. An increase of the resistivity with increased irradiation is expected. In the first place, the measurement of the resistivity of the electrodes is done using the so called *Argon scans*. Such tests are performed regularly before or after test beam periods through high voltage scans of the detectors operated with pure Argon. The electric field strength at which Argon breaks down being well known, the current beyond the breakdown voltage is monitored. Assuming a relation $I_{mon} = HV_{eff}/R_{elec}$ beyond the breakdown voltage, the resistance of

the resistivity is then

⁴²¹⁷ deduced by using Formula 5.6 where S is the surface area of the gap and l the thickness of a single
⁴²¹⁸ electrode.

$$(5.6) \quad \rho = R \times \frac{S}{2 \times l}$$

⁴²¹⁹ There exist other ways to access a quantity directly related to the resistivity. During the testbeam
⁴²²⁰ periods, the efficiency of the detectors is measured with both source OFF and source ON with high
⁴²²¹ irradiation. The shift of voltage introduced by an irradiation is directly linked to the rate capability
⁴²²² of the detector and hence to the resistivity of the electrodes. By comparing the efficiency curves
⁴²²³ observed with source ON and OFF during a single testbeam, it is possible to access the local mean
⁴²²⁴ resistance of the detector during a testbeam period. This value can be compared to the resistivity
⁴²²⁵ directly measured using the argon scans. It also provides a tool to compare different testbeam results
⁴²²⁶ by getting rid of the bias introduced by the fluctuation of the resistivity through time. The mean
⁴²²⁷ resistance is computed as in Formula 5.7.

$$(5.7) \quad R = \frac{\Delta HV}{\Delta I} = \frac{HV^{ON} - HV^{OFF}}{I^{ON} - I^{OFF}}$$

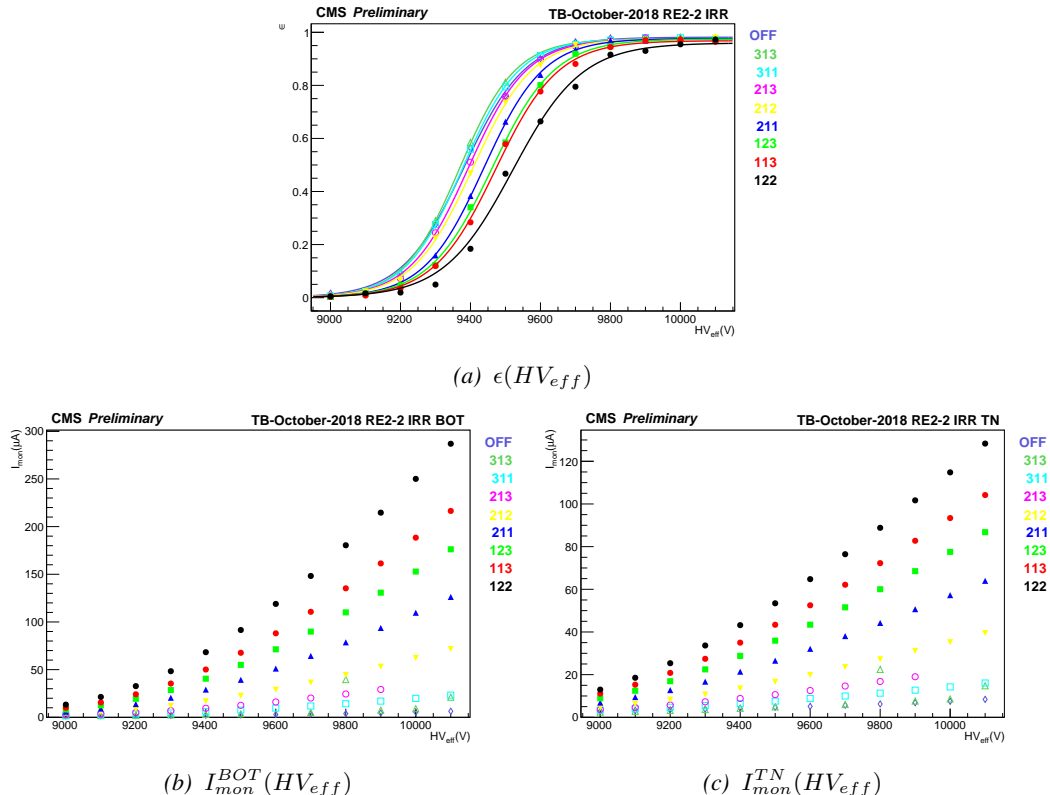


Figure 5.44: Efficiency (a) and monitored currents of the bottom (b) and top narrow (c) gaps as a function of the effective voltage of chamber RE2-2-NPD-BARC-09 during October 2018 testbeam period.

4228 It is important to note that the result provided by using this method will only concern the re-
 4229 sistance of the detector under the beam, including the little contribution of the resistance of the gas
 4230 volume itself. The translation to the resistivity of the electrodes is not straight forward even though
 4231 the result falls in the same order of magnitude. Also, the quality of the resistance extraction depends
 4232 on which level of irradiation is available in the data. During October 2018 testbeam period, HV
 4233 scans were done on partition C of the RPCs (bottom and top narrow gas gaps) with source OFF and
 4234 with eight diffent ABS values: ABS 313 (464), ABS 311 (100), ABS 213 (46.4), ABS 212 (21.5),
 4235 ABS 211 (10), ABS 123 (6.9), ABS 113 (4.6) and ABS 122 (3.2). T1 was placed close to the bunker
 4236 upstream wall at a distace of 5.6 m from the source. This position corresponds to a gamma current
 4237 of the order of $5 \times 10^5 \text{ cm}^{-2} \text{ s}^{-1}$ with source fully open.

4238 In a first step, the efficiency sigmoids as well as the bottom and top narrow gaps' monitored
 4239 current as a function of the effective voltage were retrieved as can be seen from Figure 5.44. The
 4240 goal is to compute the value of the effective voltage at the knee HV_{knee} of the sigmoids. The knee
 4241 where $\epsilon = 0.95 \times \epsilon_{max}$ would be the best location to extract the value of the resistivity. At this point,
 4242 the performance of the detectors is stable and a little variation of voltage does not have a large effect
 4243 on the efficiency. The effective voltage at the knee is given by Formula 5.8.

$$(5.8) \quad HV_{knee} = HV_{50} + \frac{\ln(19)}{\lambda}$$

4244 The monitored current at the knee I_{knee}^G for each gap G is then computed by extrapolating from
 4245 the monitored currents value located around HV_{knee} as in Formula 5.9 where I_{\downarrow}^G and HV_{\downarrow}^G are the
 4246 monitored current and the effective voltage at the voltage point bellow the knee and I_{\uparrow}^G and HV_{\uparrow}^G
 4247 are the monitored current and the effective voltage above the knee.

$$(5.9) \quad I_{knee}^G = I_{\downarrow}^G + (I_{\uparrow}^G + I_{\downarrow}^G) \times \frac{HV_{knee} - HV_{\downarrow}^G}{HV_{\uparrow}^G - HV_{\downarrow}^G}$$

4248 Once the values of the monitored currents are known at the knee, the mean current flowing
 4249 through the gaps at the level of the studied partition P can be computed. First of all, the currents at
 4250 knee of the gaps in the beam line is normalised to the area of the gap active area seen by the local
 4251 read-out partition $S^{G,P}$. Then the mean current at knee \bar{I}_{knee}^P is computed by ponderating the local
 4252 currents $I_{knee}^{G,P}$ of each gap by their respective active area in the partition.

$$(5.10) \quad \begin{aligned} I_{knee}^{G,P} &= \frac{I_{knee}^G \times S^{G,P}}{S^G} \\ \bar{I}_{knee}^P &= \frac{I_{knee}^{1,P} \times S^{1,P} + I_{knee}^{2,P} \times S^{2,P}}{S^{1,P} + S^{2,P}} \end{aligned}$$

4253 The variation of effective voltage and mean monitored current at the knee in between the Source
 4254 OFF and ON scans can then be obtained. The local resistivity of the detector can finally be calculated
 4255 combining Formula 5.6 and Formula 5.7. This process is performed for every scan of each approved
 4256 test beam period as can be seen in Figure 5.45. Finally, the most probable resistivity during the test
 4257 beam period is obtained thanks to a constant fit. The value of the mean partition resistivity displayed
 4258 in Figure 5.45 is of the same order than what would be expected for CMS RPCs.

Later, the value extracted from this method will be used to compare the efficiency sigmoids of the different testbeam periods. During the operation of the detector without irradiation, the voltage drop across the detector almost only consists in a voltage drop across the gas volume. As the electrodes behave approximately as charged capacitors, there is only a negligible voltage drop across their volume. The charge of the electrodes is only affected locally by the charge carriers freed by avalanches in the gas volume. Nevertheless, under irradiation, the conversion of photons is uniform throughout the electrodes' volume and charge recombination happens everywhere at the same time making it impossible for the electrodes to stay charged. Hence, a significant part of the voltage drop appears across the electrodes, explaining the usual voltage shift observed in the performance of irradiated RPCs. The data comparison will then be done using the gas voltage drop HV_{gas} obtained by correcting the effective voltage HV_{eff} thanks to Formula 5.11 in which R is the resistance computed at the knee using Formula 5.7 in the RPC partition of interest and \bar{I} is the mean current in this partition at each voltage step.

$$(5.11) \quad HV_{gas} = HV_{eff} - R \times \bar{I}$$

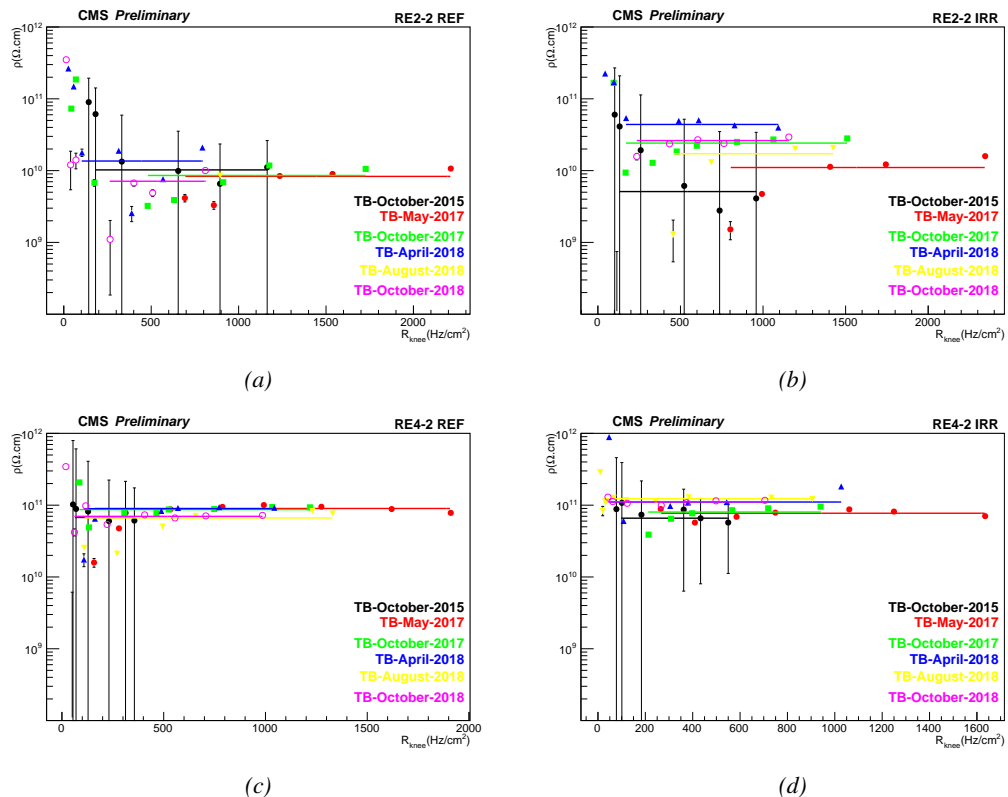
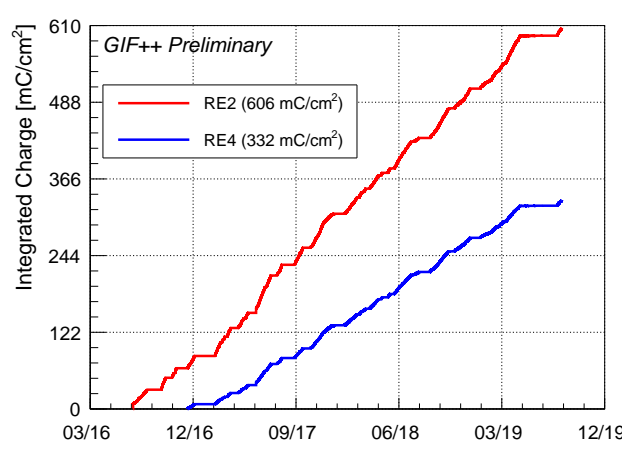


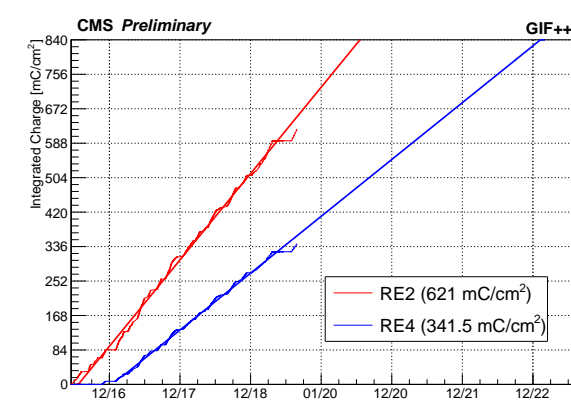
Figure 5.45: Resistivity extraction for all approved test beam periods for the reference RE2/2 (a) and RE4/2 (c) chambers and the irradiated RE2/2 (b) and RE4/2 (d) chambers.

4272 5.3.7 Results and discussions



4287 *Figure 5.46: Total integrated charge in the irradiated RPCs,*
 4288 *RE2-2-NPD-BARC-9 and RE4-2-CERN-165, in July 2019.*
 4289 *The irradiation of the RE2 chamber started early July 2016 while*
 4290 *the RE4 chamber couldn't be irradiated before end of November*
 4291 *2016.*

4292 charge accumulation of the RE2 detector is faster than which of the RE4 and is expected to end
 4293 within a year. In the case of the RE4 RPC, the irradiation would go on for more than two years at
 4294 the current charge accumulation rate. This time would be reduced after the end of the longevity study
 4295 of the RE2 by placing the trolley hosting the detectors closer to the source.



4309 *Figure 5.47: Linear projection of the time necessary to finish the*
 4310 *longevity program on the RE2 and RE4 detectors at the GIF++.*

4311 on all four RPCs, the dark currents are monitored. Two voltage of interest are being compared
 4312 through time. The first value of interest was chosen at a STANDBY voltage of 6500 V where no
 4313 multiplication process happens. This is done to follow the variations of the ohmic component of the
 4314 current. The monitored dark current in STANDBY are shown in Figure 5.48. At the time of writing,
 4315 the ohmic currents for all detectors are stable. Both RE4 detectors appear to follow the same trend

4273 Since 2015, CMS RPCs have been
 4274 irradiated at the GIF++ with the
 4275 goal to reach a total integrated
 4276 charge per irradiated detector of
 4277 $0.84 \text{ C}/\text{cm}^2$ while certifying the
 4278 detectors to a single hit rate capa-
 4279 bility of $600 \text{ Hz}/\text{cm}^2$. At the
 4280 time of writing, the RE2 and RE4
 4281 chambers were exposed to 74 and
 4282 40% of their total irradiation pro-
 4283 gram respectively, as shown in Fig-
 4284 ure 5.46. According to Figure 5.47,
 4285 a few years of irradiation are ex-
 4286 pected before reaching the end of
 4287 the longevity study for both types of
 4288 detectors and before reaching a fi-
 4289 nal answer on whether the present
 4290 CMS RPC system will be able to
 4291 live through HL-LHC or not. The

4292 Throughout the longevity pro-
 4293 gram, great care was put into mon-
 4294 itoring the detector characteristics.
 4295 While presenting the results, current
 4296 densities expressed in $\mu\text{A}/\text{cm}^2$ will
 4297 be showed in the place of currents.
 4298 In the first part of the discussion the
 4299 current densities will be referred to
 4300 as "dark current". Also, the data
 4301 of the reference detectors will be
 4302 displayed with increasing integrated
 4303 charge. This integrated charge will
 4304 always refer to the integrated charge
 4305 of the irradiated detectors.

4306 Using the data collected during
 4307 the weekly noise scans performed

4317 while the ohmic current of the irradiated RE2 detector has increased a little. Nevertheless, this in-
 4318 crease is only of 10 to 20 pA/cm² and a similar behaviour can be observed for both RE4 detectors.
 4319 There is no reason to associate the increase in ohmic current with the irradiation.

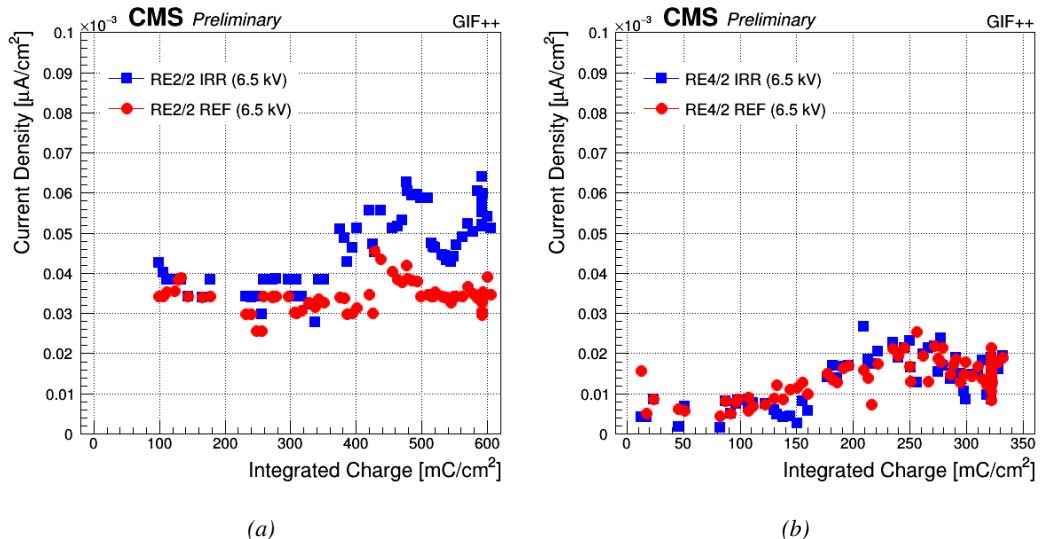


Figure 5.48: Monitoring of the ohmic component of the dark current with increasing integrated charge at a voltage of 6500 V of the RE2-2 (a) and RE4-2 (b) detectors installed at the GIF++.

4320 The second value of interest is located in the gain region near the working point at a voltage
 4321 of 9600 V for the RE2 detectors and of 9500 V for the RE4 ones. Monitoring the multiplication
 4322 region allows to spot the appearance of hot spots across the detectors' areas. A local damage to the
 4323 electrode could result in an increase of local discharges and an overall increase of the current drawn
 4324 by the detector which would show in the monitored values. Near the working voltage, in addition to
 4325 the current densities, the noise rate per unit area are monitored as can be seen in Figure 5.49. In the case
 4326 of the RE2 detectors, the dark currents and noise rate stay stable since the beginning of the irradiation
 4327 program. The variability of the dark current of the irradiated chamber is higher than the one of the
 4328 reference chamber but seem to always come back between 0.1 and 0.15 nA/cm². Concerning the
 4329 RE4 detectors, both chambers are very stable up to an irradiation of 150 mC/cm². Even though
 4330 the noise rate of the reference chamber seem to fluctuate a lot between 0.5 and 3.5 Hz/cm² before
 4331 this value, the monitoring of the noise rate per unit area following this early range as well as the
 4332 very stable dark current would suggest that the chamber was in fact suffering from a bad grounding.
 4333 Indeed, beyond 150 mC/cm², the noise rate suddenly stabilizes between 0.1 and 0.2 Hz/cm² while
 4334 the dark current increases very slightly to 50 pA/cm². On the contrary, the irradiated chamber
 4335 which was very stable under 150 mC/cm², sees its dark current and its noise rate increase and
 4336 fluctuate with a similar shape. The noise rate is still within the requirements of CMS. Indeed, an
 4337 upper threshold of 1 Hz/cm² was considered to be good enough to prevent fake events due to noise.
 4338 Regarding the dark current, so far the highest peak, reached a little higher than 0.4 nA/cm² and
 4339 have since dropped to 0.2 nA/cm². During *source scans* at gamma rates per unit area usually above
 4340 400 Hz/cm², the current densities are of the order of 10 nA/cm², almost two orders of magnitude
 4341 larger than the dark current. Nevertheless, both the noise rate and dark current have almost gained
 4342 an order of magnitude at their highest monitored values and will need to be carefully followed at

⁴³⁴³ higher values of integrated charge.

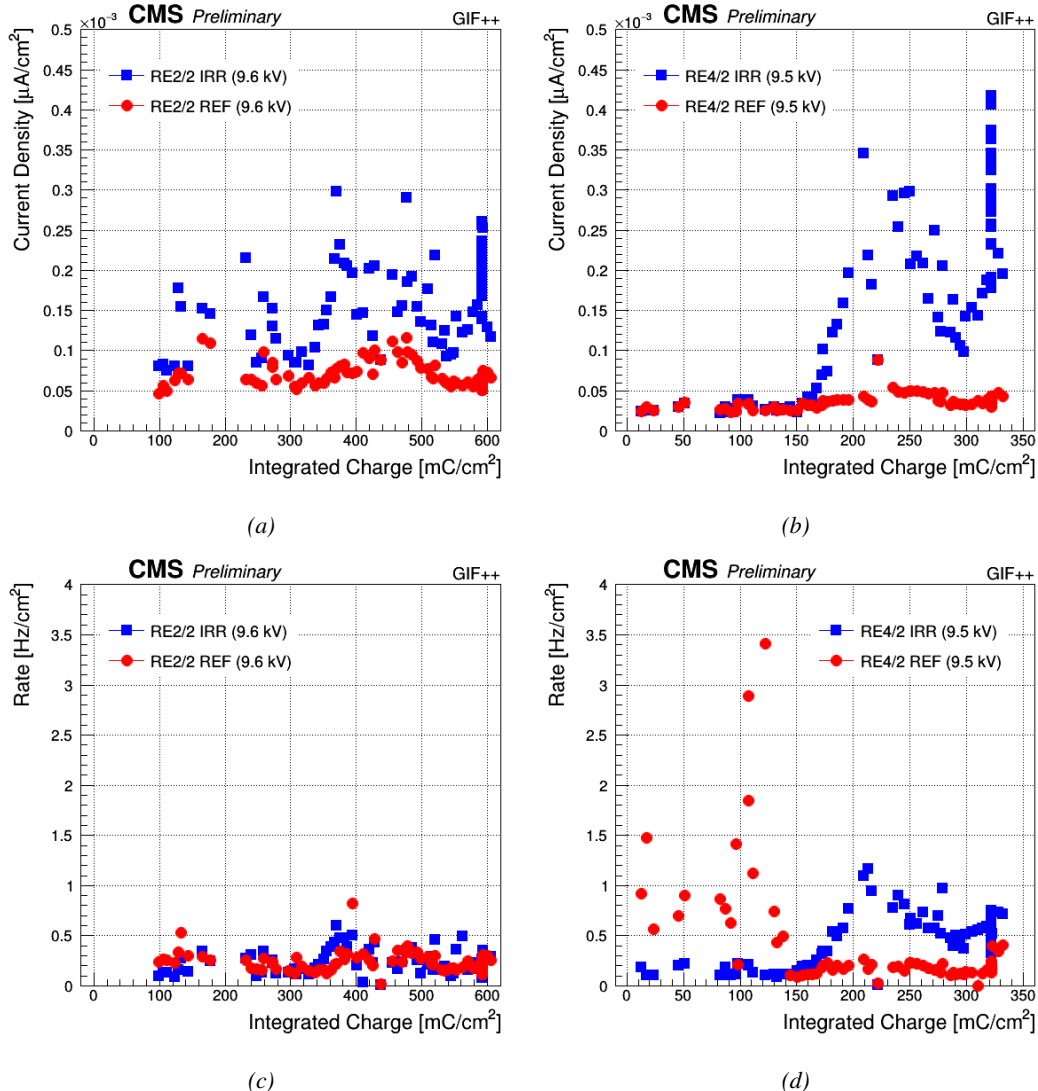


Figure 5.49: Monitoring of the physics component of the dark current and of the noise rate per unit area with increasing integrated charge at a voltage of 9600 V for the RE2-2 detectors (a) and (c) and at a voltage of 9500 V for the RE4-2 detectors (b) and (d) installed at the Gif++.

⁴³⁴⁴ The same exercise is done using the data collected during the weekly source scans. The moni
⁴³⁴⁵ toring of the current densities and of the gamma rate per unit area is showed in Figure 5.50. The
⁴³⁴⁶ reported measurements are always performed with the same source conditions corresponding to an
⁴³⁴⁷ irradiation attenuated by a factor 6.9. The increase in dark current of the irradiated RE4 chamber
⁴³⁴⁸ don't have any visible effect when the source irradiates the detectors. No signs of ageing due to
⁴³⁴⁹ irradiation is yet to be seen for both the RE2 and RE4 detectors. The current densities and gamma
⁴³⁵⁰ rates of all four detectors evolve following the same phases of increase and decrease, as confirmed
⁴³⁵¹ by Figure 5.51.

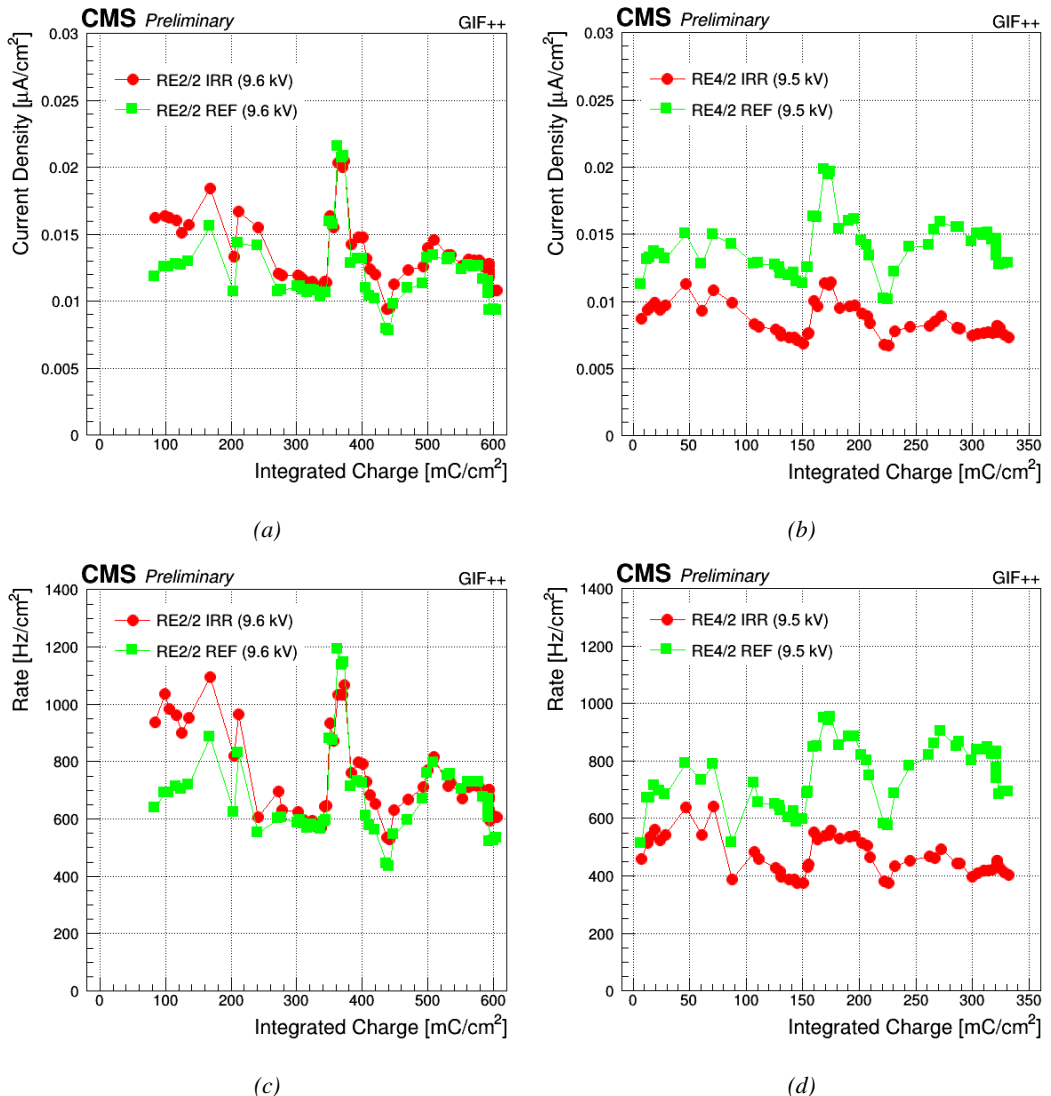


Figure 5.50: Monitoring of the current density and of the gamma rate per unit area under irradiation with increasing integrated charge at a voltage of 9600 V for the RE2-2 detectors (a) and (c) and at a voltage of 9500 V for the RE4-2 detectors (b) and (d) installed at the GIF++. The source irradiation is attenuated by a factor 6.9.

The use of Principal Component Analysis (PCA) [279] reveals that the study of the correlations between the current densities and the gamma rates can be reduced to a single dimension. To perform the PCA, the algorithm used normalises each variable to get a mean value of 0 and a variance of 1 resulting in the study of the variance. The associated *Scree* plot [280] showed in Figure 5.51b indicates for each of the components of the PCA, the eigen values of the covariance matrix. In this case, the eigen values have been normalised to express the percentage of variance explained by each component. More than 93% of the data variation can be explained using a simple linear composition of the current density and of the gamma rate. It is expected as the current density and gamma rate

4360 are two side of the same physical process. Any deviation would mean that other processes than the
 4361 conversion of photons in the electrode material take place.

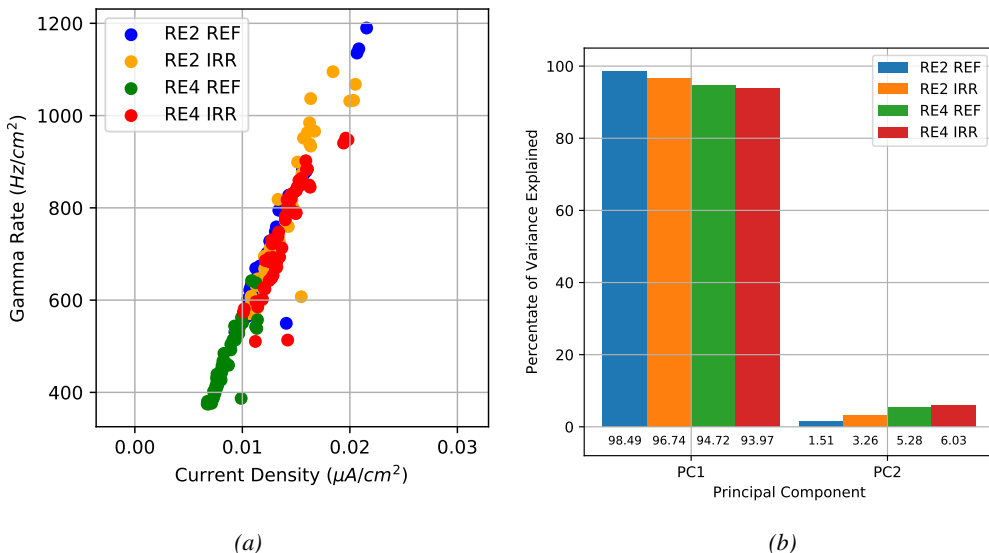


Figure 5.51: (a) Gamma rates as a function of the corresponding current densities. (b) Scree plot obtained at the output of PCAs performed on each set of current densities and corresponding gamma rates.

4362 The fluctuations observed on Figure 5.50 may arise due to different factors such as the environmental
 4363 conditions (gas temperature, gas relative humidity, environmental pressure) or the presence
 4364 of other experiments between the source. The distance from the source and the trolley, and the
 4365 gamma current at which the detectors are irradiated during the ageing procedure are kept as consist-
 4366 ent as possible and should not contribute to the fluctuations in current density and gamma rate. In
 4367 order to have a better understanding, the monitoring of the environmental parameters, i.e. the gas
 4368 relative humidity and temperature both at the supply and at the exhaust of the trolley together with the
 4369 humidity and temperature inside of the bunker and the environmental pressure, is showed in Fig-
 4370 ures 5.52, 5.53 and 5.54. In these Figures, the data are displayed with increasing integrated charge
 4371 in the case of the RE2 and of the RE4 detectors for comparison purposes. Each value of integrated
 4372 charge corresponds to a unique date.

4373 Comparing the trends visible in Figure 5.50 to the monitoring of the different environmental
 4374 parameters, it would seem that the temperature variations may be able to explain most of the fluctua-
 4375 tions. This assumption is confirmed by a PCA performed on data sets composed for each detector
 4376 of the monitored environmental parameters, except the temperature and the relative humidity of the
 4377 air in the bunker, and of its current density and gamma rate data. The corresponding Scree plot is
 4378 showed in Figure 5.55. The dimension reduction for this data set is less trivial. Nevertheless, most of
 4379 the variation in current densities and gamma rates is held by the first principal component of the PCA
 4380 basis for all four detectors, as can be understood from the *Score* plots presented in Figure 5.56. The
 4381 Score plots show for each principal component the decomposition of its correponding eigen vector
 4382 in terms of the variables of the original data set normalised to the eigen value associated to the eigen
 4383 vector. The eigen vectors represent the directions of maximum variance. Hence, the *strength* of each
 4384 original variable leads to its variability along this direction. The first principal component can be

4385 interpreted as the variations directly linked to the fluctuations in current density and gamma rate.
 4386 The linearity between these two variables is again visible as both variables carry the same amount
 4387 of variability. Looking at the other variables along the first principal component, the temperature
 4388 seems to always be a positive source of variation for the current density and the gamma rate. The
 4389 contribution of the atmospherical pressure is always small. The relative humidity of the gas doesn't
 4390 provide a consistent feedback.

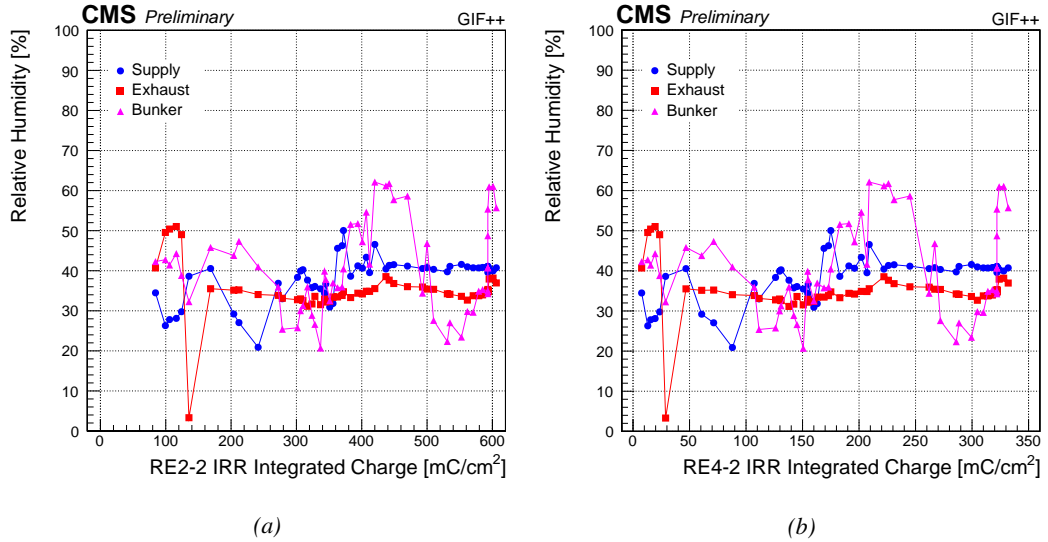


Figure 5.52: Monitoring of the gas relative humidity at the level of the supply and of the exhaust of T1 and ambient relative humidity at the GIF++ during the source scans.

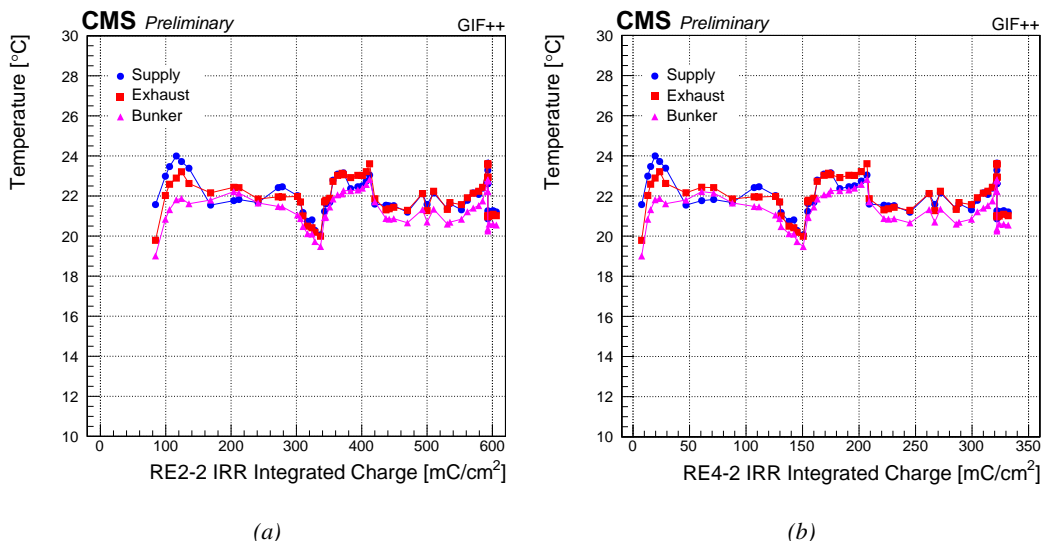


Figure 5.53: Monitoring of the gas temperature at the level of the supply and of the exhaust of T1 and ambient temperature at the GIF++ during the source scans.

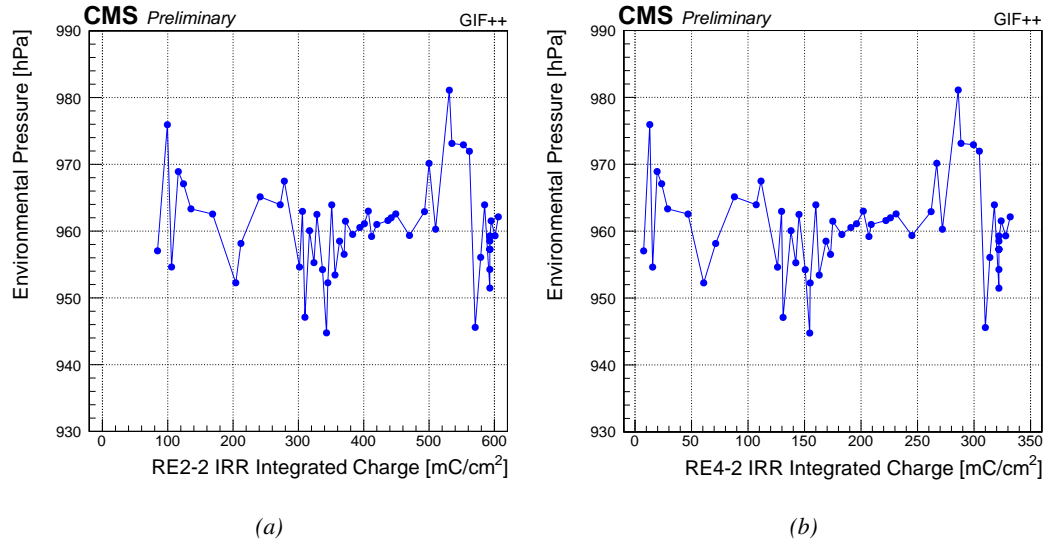


Figure 5.54: Monitoring of the environmental pressure at the GIF++ during the source scans.

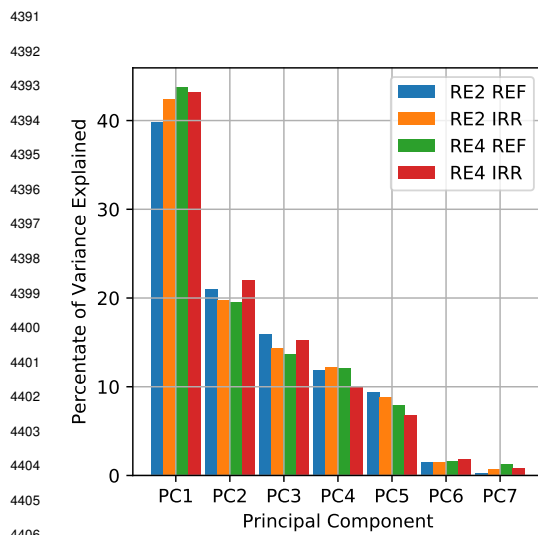


Figure 5.55: Scree plot corresponding to the PCAs performed on the seven dimensions of each RPC data set to study the influence of the environmental parameters in the fluctuation of the current densities and gamma rates.

much more stable in terms of temperature providing an explanation for the less refined temperature correction on the applied voltage.

Aside of the fluctuations due to the insufficient temperature correction, it seems that both the current densities and gamma rate tend to decrease with time. This decrease affects both the RE2 detectors and the irradiated RE4 detector. The current densities went from 12, 16 and 9 nA/cm² to 9, 10 and 7 nA/cm² respectively for the reference RE2, the irradiated RE2 and the irradiated RE4. The monitored gamma rates decreased from 650, 900 and 500 Hz/cm² to 500, 600 and 400 Hz/cm².

The other principal components are more difficult to interpret. The second component seems to always link the variabilities of the relative humidities. The relative humidity of the exhaust could be interpreted as a negative contribution of the relative humidity of the input gas. The third principal component likely represents the fluctuations of atmospheric pressure. The next principal components are not consistent from one detector to the other.

It is safe to conclude that the voltage correction performed at the GIF++ is not able to account for the high variability of the temperature in the bunker and, hence, of the gas mixture the detectors are operated with. The pressure on the other hand does not play a great role in affecting the RPC operation as the voltage correction was improved to efficiently take into account this parameter [234]. The environmental conditions in the CMS cavern are

4418 The rate of decrease is nevertheless faster for the irradiated detectors. The reference RE4 detector
 4419 features a more stable operation through time if not a light increase of the two variables. Its current
 4420 density varies from 11 to 13 nA/cm² and its gamma rate from 500 to 700 Hz/cm².

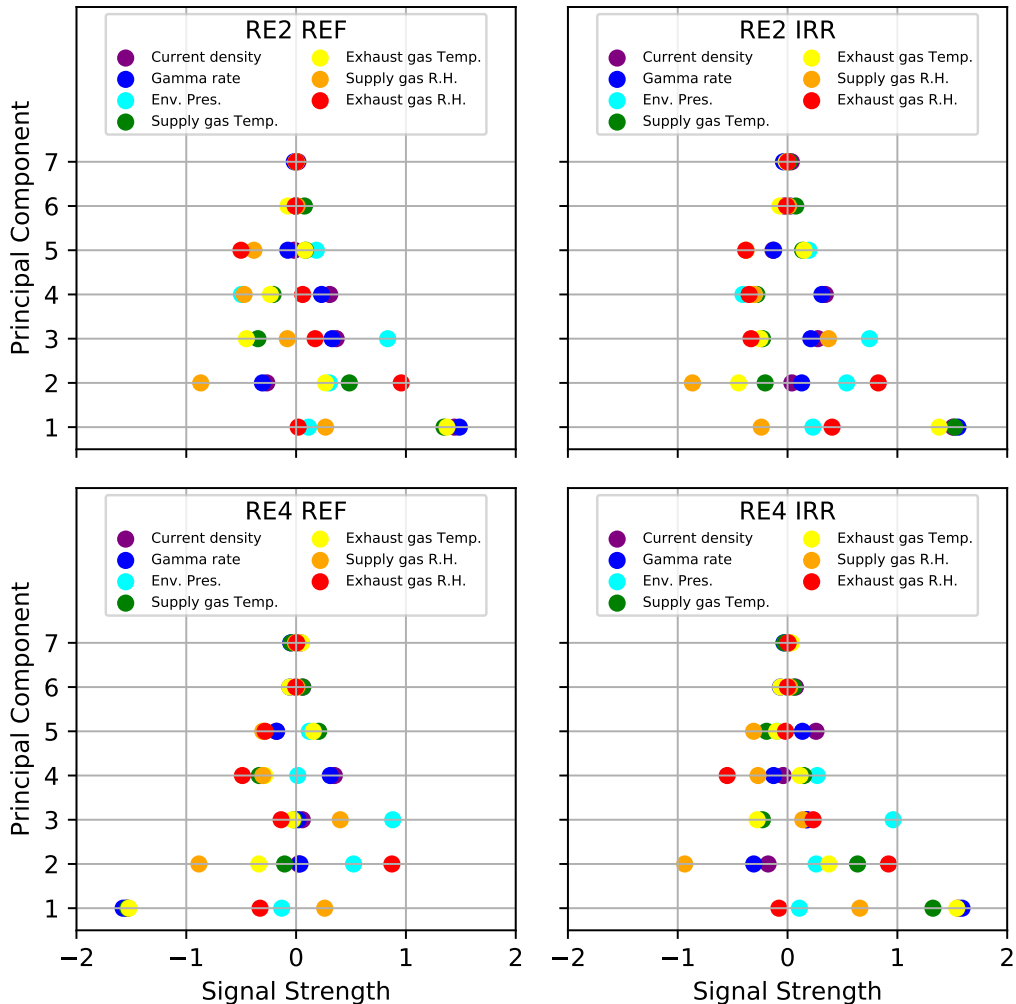


Figure 5.56: Score plots corresponding to the PCAs performed on the seven dimensions of each RPC data set to study the variations in current density and gamma rate.

4421 Comparing the evolution of the current densities and of the gamma rates to the monitored resistivity showed in Figure 5.57 may explain the decrease observed for three of the four chambers and
 4422 the more stable behaviour of the reference RE4. Indeed, both the RE2 detectors and the irradiated
 4423 RE4 show an increase in resistivity. The strongest increase of resistivity is observed for both the irra-
 4424 diated detectors whose average resistivity went from 2.27 to $4.83 \times 10^{10} \Omega \text{ cm}$ for the RE2 and from
 4425 7.17×10^{10} to $1.96 \times 10^{11} \Omega \text{ cm}$ for the RE4. The increase of average resistivity of the reference
 4426 RE2 chamber from 1.88 to $2.40 \times 10^{10} \Omega \text{ cm}$ is much smaller. On the contrary, the average resistivity
 4427 of the reference RE4 is more or less at the same level at the time of writing ($9.22 \times 10^{10} \Omega \text{ cm}$) than
 4428

it was at the start of the longevity program ($8.36 \times 10^{10} \Omega \text{cm}$). The differences in increase rate of the irradiated chambers with respect to the reference ones can be seen in Figure 5.58. It is clear that both the current density and the gamma rate of the irradiated detectors decreases relatively to the reference ones. This is consistent with the relative increase in average resistivity of the irradiated chambers with respect to the reference ones.

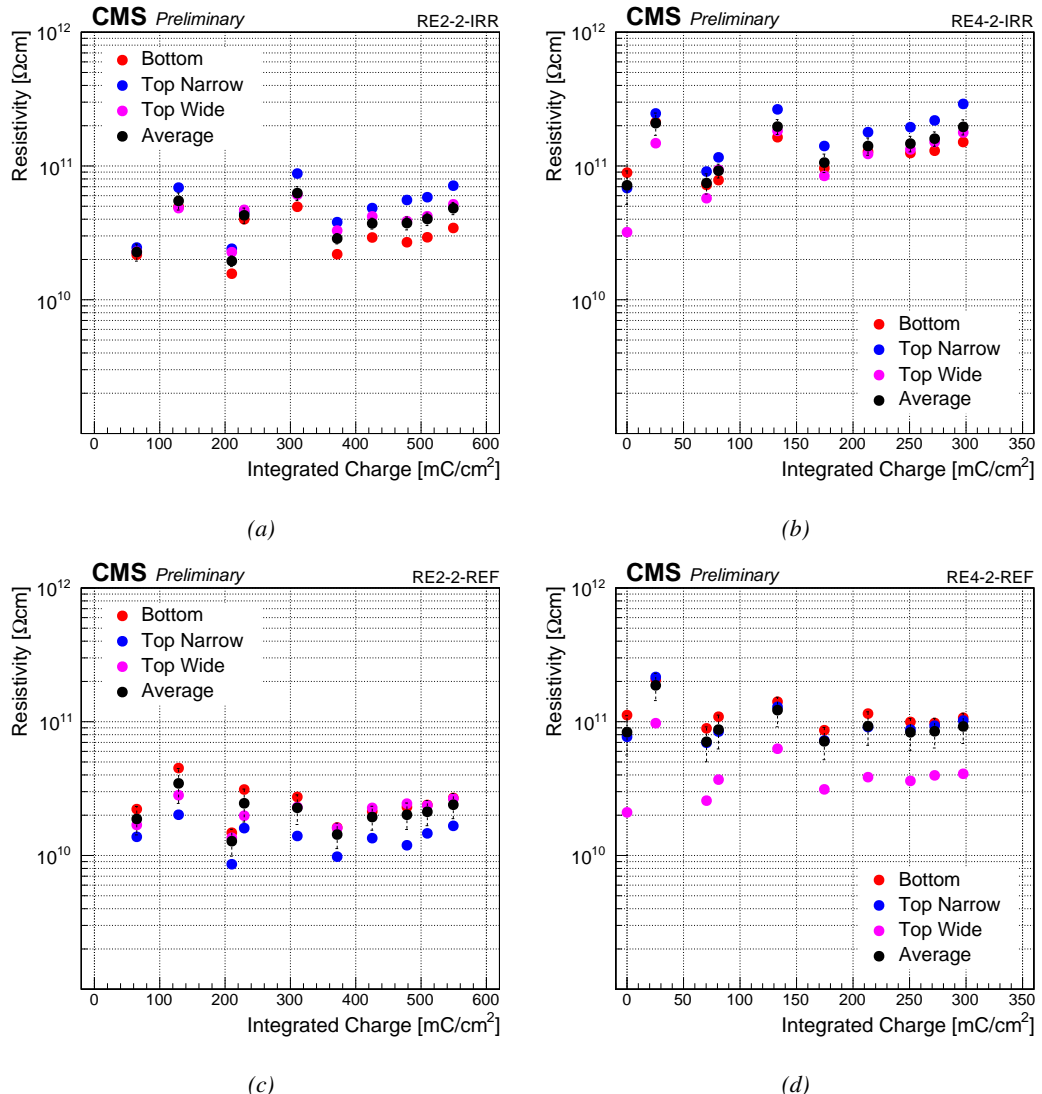


Figure 5.57: Monitoring through argon scans of the resistivity with increasing integrated charge for the RE2-2 detectors (a) and (c) and the RE4-2 detectors (b) and (d) installed at the GIF++.

In addition to the decrease of the irradiated detectors current densities and gamma rates with respect to the reference RPCs, the fluctuation that can be observed in the ratios could be related to the fluctuations of gas humidity observed in Figure 5.52. The results of the PCA performed on the same data set than previously but focussing on the ratios reveal that the humidity of the gas could

indeed play a role in the evolution of the ratios and by extension of the resistivity of the detectors. The Scree plot in Figure ?? shows that approximately 75% of the variability in the data set is explained by the first three principal components.

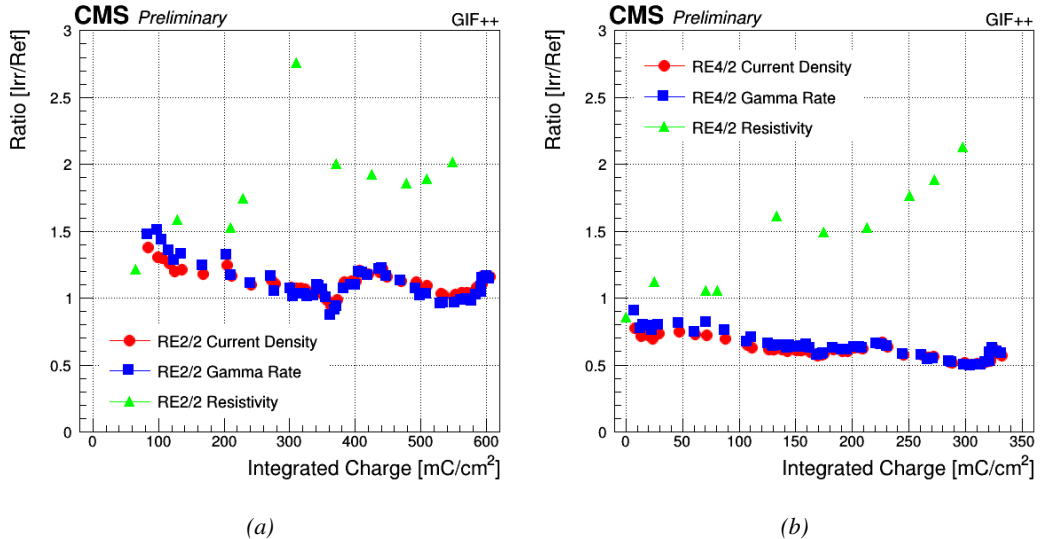


Figure 5.58: "Irradiated over Reference" parameter ratios (current densities, gamma rates and resistivities) as a function of the integrated charge for the RE2 5.58a and the RE4 5.58b detectors installed at the Gif++.

The Score plots in Figure ?? give us more information about the variability along these three directions. It would seem that the first principal component mainly holds the variations of the current density and gamma rate ratios. Their fluctuation is negatively linked to the relative humidity of the gas in the supply and positively to the relative humidity of the gas in the exhaust. The contributions of the temperature are not consistent and the pressure seems not to affect the data. The variability of the temperature is completely described by the second principal component alone and the variability of the atmospheric pressure is explained by the third principal component. The fourth one, which explains less variability, could be, as before, a link between the atmospheric pressure and the gas relative humidity but this is not clear.

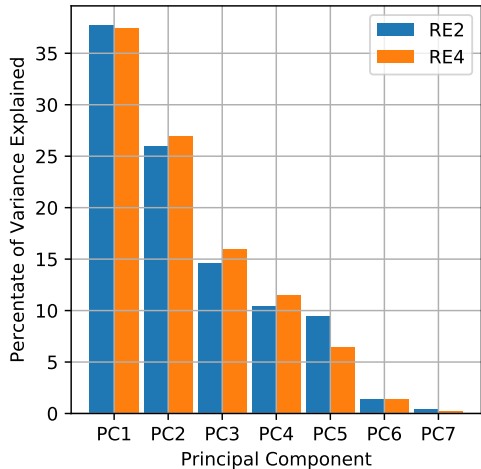


Figure 5.59: Scree plot corresponding to the PCAs performed on the seven dimensions of each RPC data set to study the influence of the environmental parameters in the fluctuation of the current densities and gamma rates.

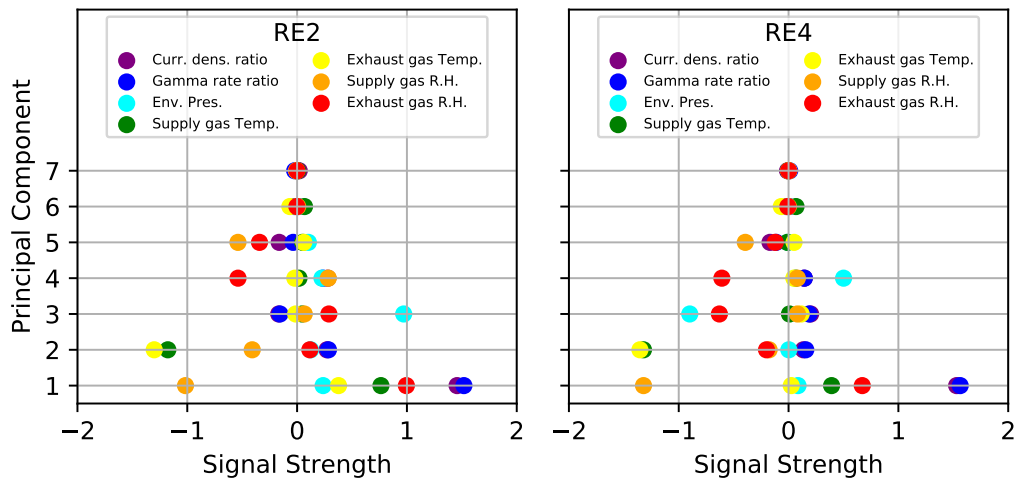


Figure 5.60: Score plots corresponding to the PCAs performed on the seven dimensions of each RPC data set to study the variations in current density and gamma rate ratios of the irradiated chambers with respect to the reference ones.

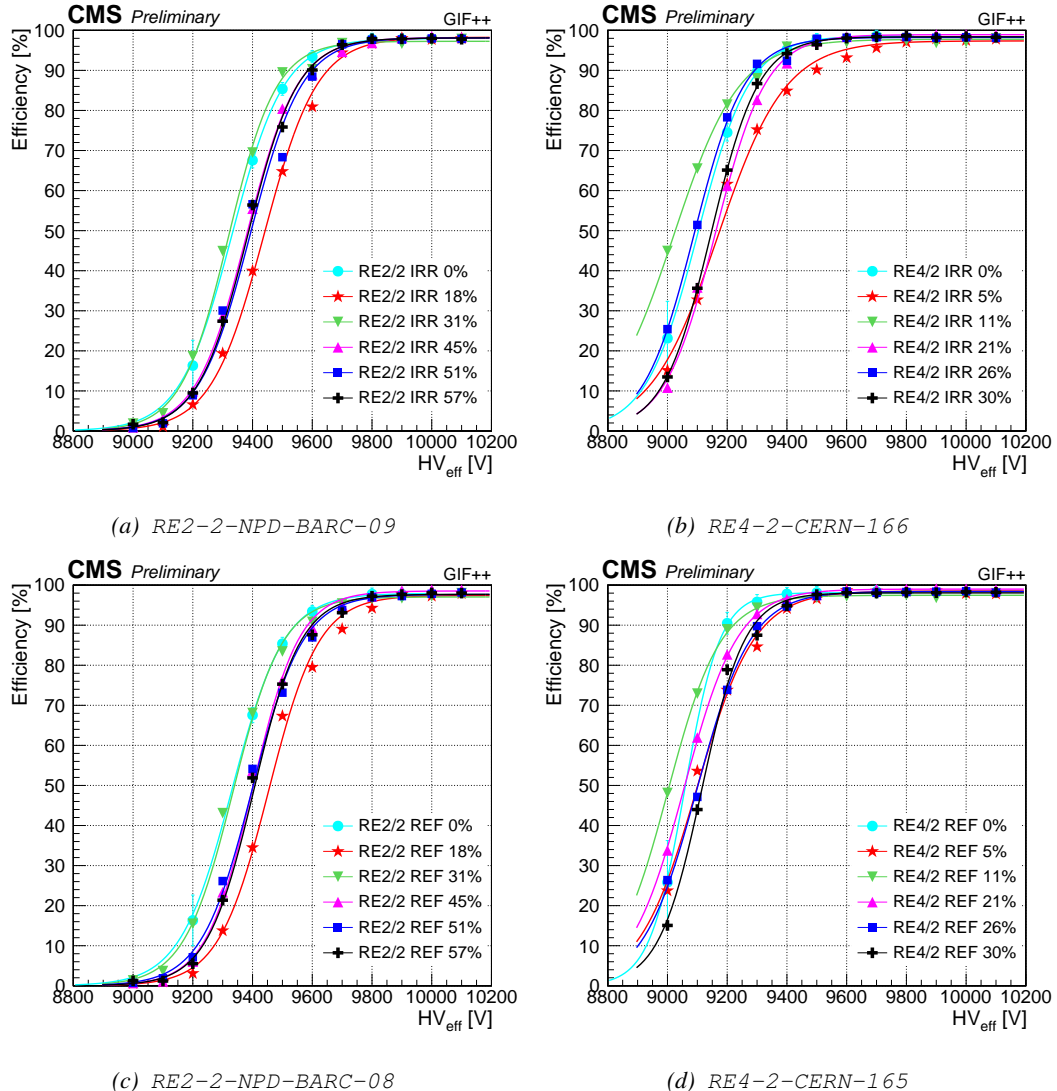


Figure 5.61

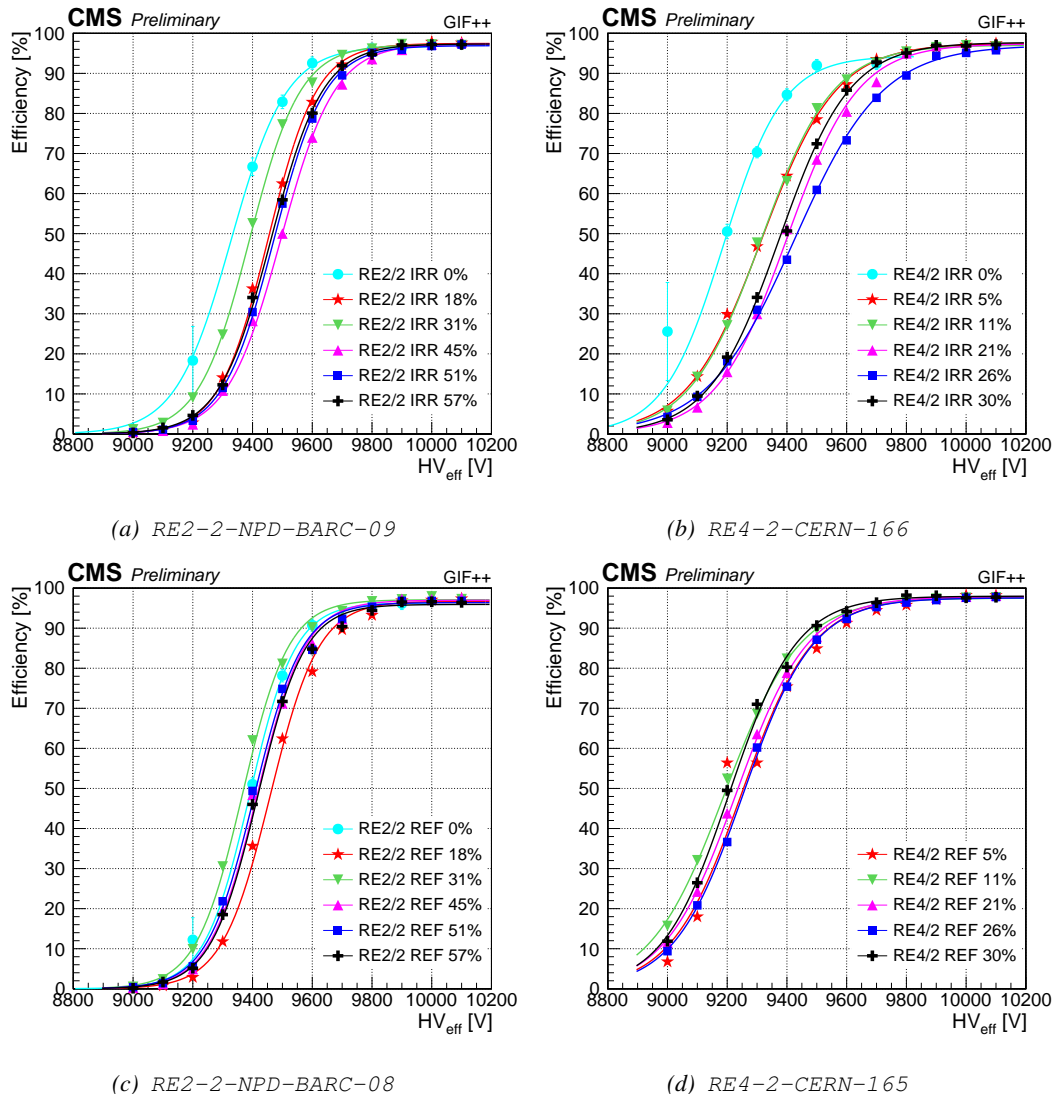


Figure 5.62

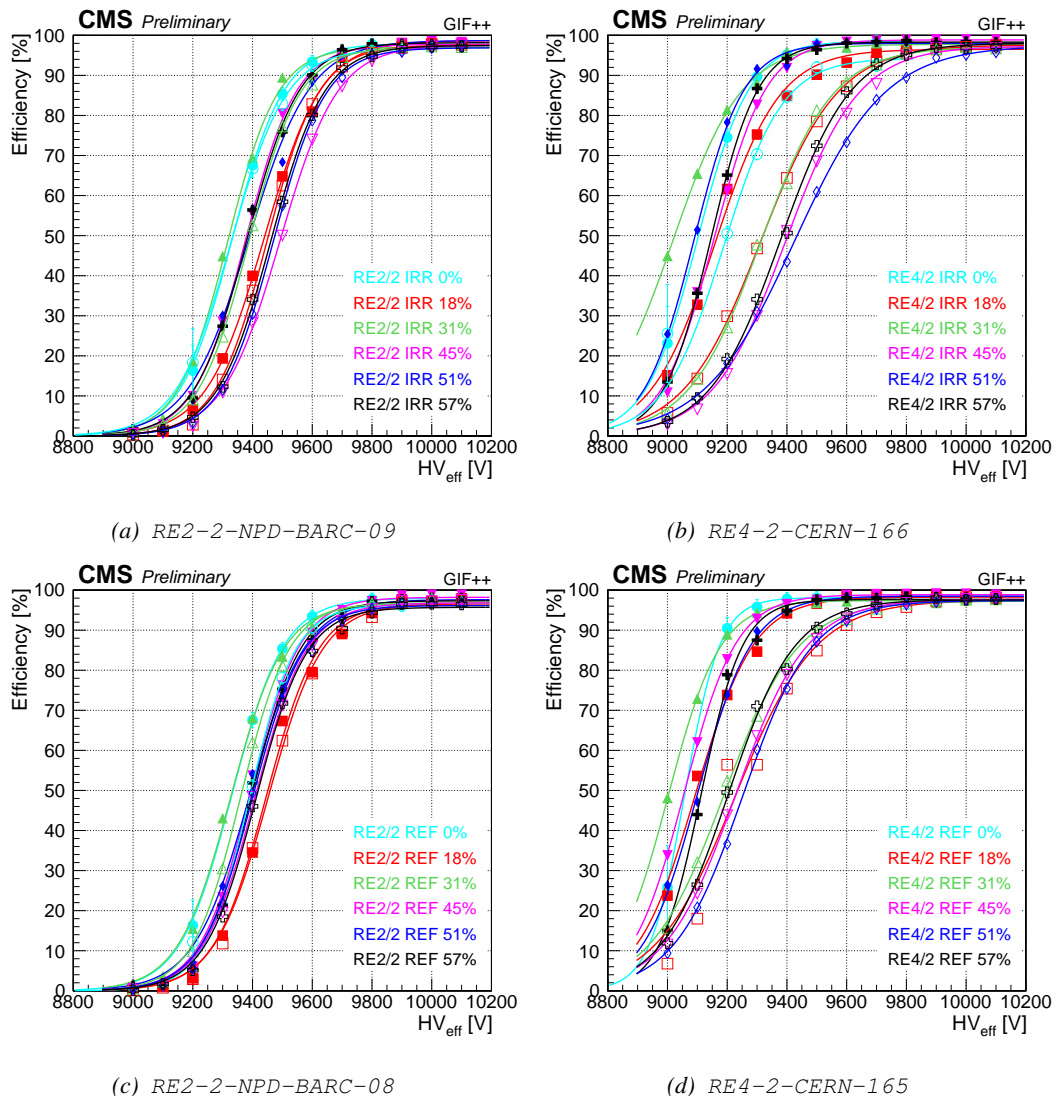


Figure 5.63

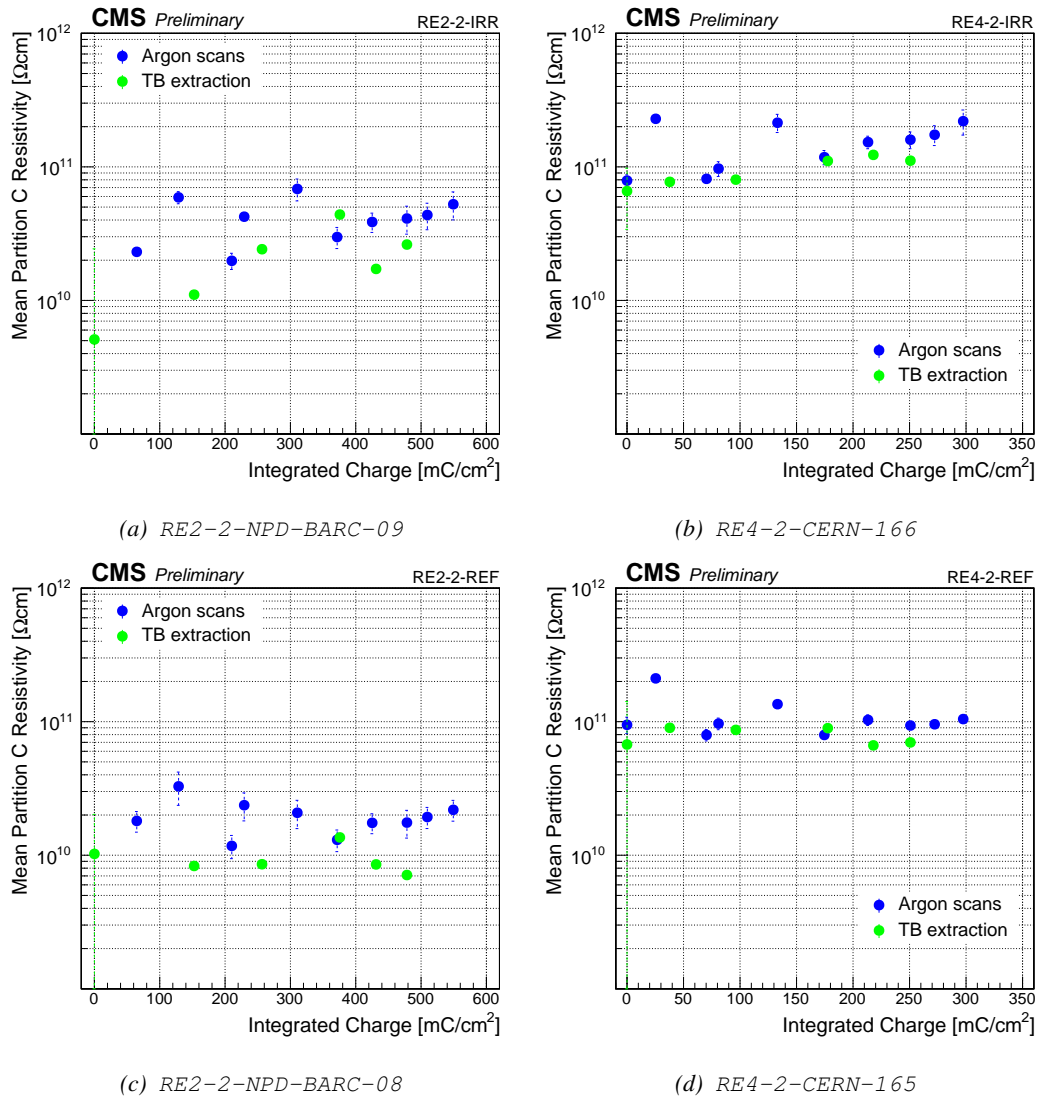


Figure 5.64

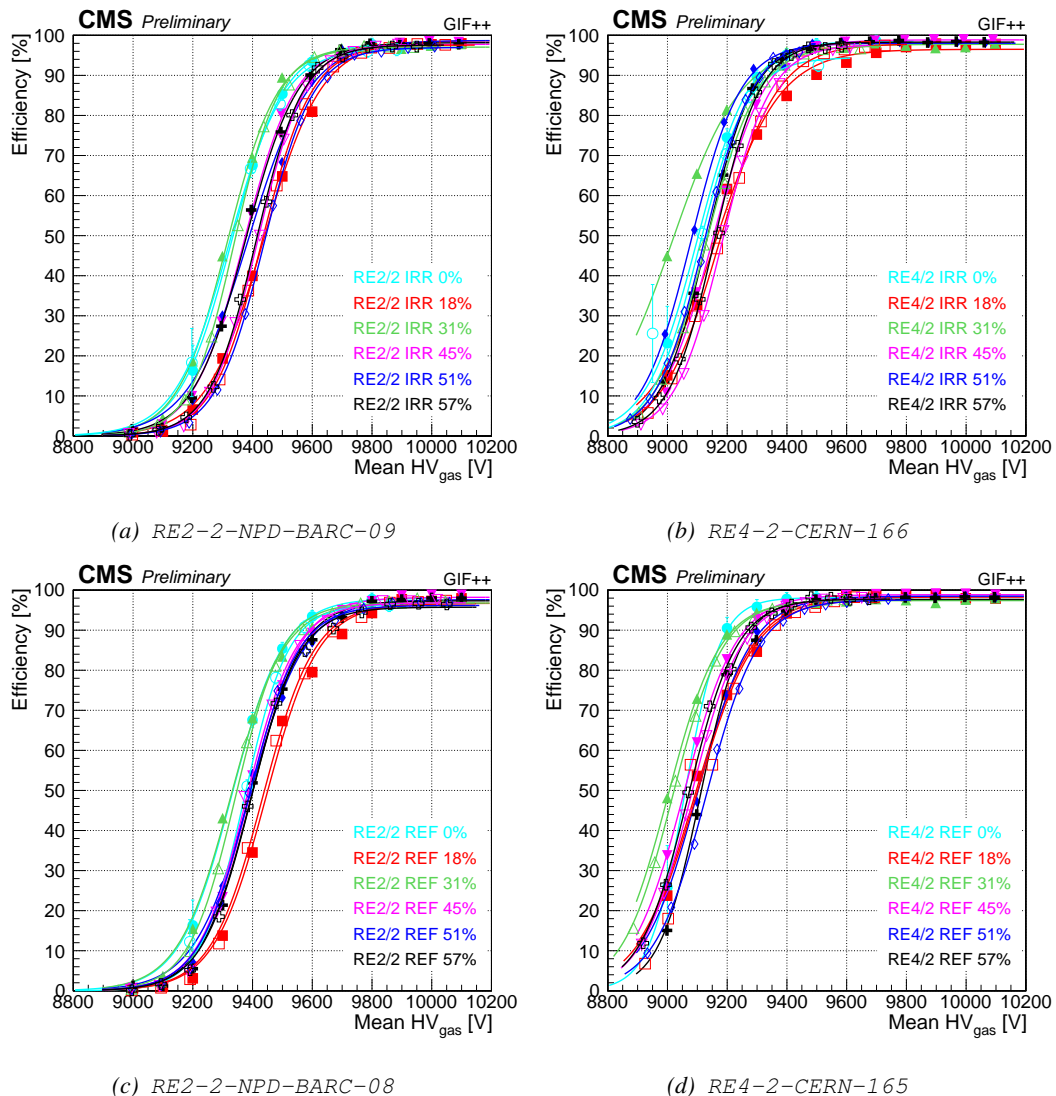


Figure 5.65

